Reactive and Functional Polymers 162 (2021) 104875

Contents lists available at ScienceDirect

Reactive and Functional Polymers

journal homepage: www.elsevier.com/locate/react

Perspective Article

Microwave-assisted RAFT polymerization of *N*-(2-hydroxypropyl) methacrylamide and its relevant copolymers

Vladimir Sincari, Svetlana Lukáš Petrova, Rafał Konefał, Martin Hruby, Eliézer Jäger *

Institute of Macromolecular Chemistry, Czech Academy of Sciences, Heyrovský Sq. 2, 16206 Prague, Czech Republic

ARTICLE INFO

Keywords:
RAFT
Microwave irradiation
HPMA
Kinetic study
Homopolymers
Copolymers
Block copolymers

ABSTRACT

A rapid and eco-friendly reversible addition-fragmentation chain transfer (RAFT) polymerization reaction of the *N*-(2-hydroxypropyl) methacrylamide (HPMA) monomer under microwave irradiation (MWI) was demonstrated. A systematic investigation to determine the optimal conditions for the polymerization, such as the reaction time, solvents, monomer stoichiometry and RAFT agents, was implemented. The polymerization kinetics were obtained using two different chain transfer agents (CTAs), namely, commercial 4-cyano-4-(phenylcarbonothioylthio)pentanoic acid and synthesized 4-cyano-4-(((ethylthio)carbonothioyl)thio)pentanoic acid, in the presence of 4,4′-azobis(4-cyanovaleric acid) as the initiator in various solvents. The controlled living character of the RAFT polymerization under MWI conditions was demonstrated by the linear increase in the number-average molecular weight (M_n) with monomer conversion. Moreover, good agreement between the theoretical and experimental M_n values was verified with pseudo-first-order kinetic plots, with low dispersities ($Đ \leq 1.04$) if a favorable solvent and/or CTA was chosen. In addition, the ability of MWI to facilitate copolymer formation was demonstrated by the preparation of relevant copolymers, such as poly(HPMA-*b*-bocAPMA), poly(HPMA-*b*-MABH) and poly(HPMA-*b*-PDPA). Altogether, these facile synthetic approaches can find applications for the synthesis of PHPMA-based homo- and copolymers that have already been clinically tested and serve as hydrophilic high-potential alternatives to polyethylene oxide.

1. Introduction

For several decades, the field of radical polymerization has experienced a renaissance due to the advent of controlled/living radical polymerization (CLRP) [1–3]. The development of CLRP techniques has been accompanied by the ability to produce well-defined polymers with controlled molecular weights and a wide range of polymer architectures and functionalities [4]. One of the most widely studied CLRP methods is reversible addition-fragmentation chain transfer (RAFT) polymerization [5,6], and there are two other types of CLRP, namely, nitroxide mediated polymerization (NMP) [7–9] and atom transfer radical polymerization (ATRP) [8–12]. Among these methods, RAFT polymerization has attracted great interest due to its applicability to a wide range of monomers and its tolerance to most functional groups and reaction solvents [13,14], as well as its low cost, narrow molecular weight distribution (low $Đ$), high end-group fidelity, and capacity for continued chain growth. However, from a practical point of view, RAFT processes are often plagued by a relatively low polymerization rate (Rp) and demonstrate some degree of rate retardation [4,15]. Accordingly, it is crucial to find a way to accelerate the Rp and simultaneously ensure that the living character of the RAFT technique is preserved [16,17].

Microwave irradiation (MWI) has currently been successfully employed for organic synthesis, inorganic synthesis, material science, polymer chemistry, and other disciplines. Over the past decade, the microwave (MW) heating technique has been successfully used for CRLP as an alternative to thermal heating. It has been demonstrated that with this approach, the conversion of monomer to polymer was much higher and the Rp was much faster [18–22]. Considering that the RAFT process normally requires reaction times ranging from several hours to several days under conventional heating conditions, MWI was successfully extended to RAFT polymerizations, overcoming this drawback. The results so far have shown that the polymerization time can be reduced to minutes or hours depending on the target weight-average molecular weight (M_w) because of the tremendous increase in the Rp. Few examples have considered the favorable effect of MWI on RAFT polymerization, which included the use of styrene [22–25], methyl methacrylate [24,26], methyl acrylate [23,24], *N*-isopropylacrylamide [27,28], *N*,*N*-dimethylacrylamide [28] diallyldimethylammonium chloride

* Corresponding author.
E-mail address: jager@imc.cas.cz (E. Jäger).

https://doi.org/10.1016/j.reactfunctpolym.2021.104875
Received 30 November 2020; Received in revised form 16 February 2021; Accepted 8 March 2021
Available online 10 March 2021
1381-5148/© 2021 Elsevier B.V. All rights reserved.

(DADMAC) [29], vinylcyclicsilazane [30] and vinyl pyridines [31] monomers. In all cases, the molecular weight distributions ($Đ$) of the polymers formed under MW conditions were narrow, opening an avenue for developing other polymers by the MWI method.

In particular, methacrylamides such as poly(*N*-(2-hydroxypropyl) methacrylamide) (PHPMA) are of great importance because they are water-soluble (highly hydrophilic), nonimmunogenic and nontoxic polymers and reside in the blood circulation for a relatively long period of time [32,33]. Furthermore, copolymers of PHPMA were the first polymer drug conjugates to enter clinical trials [33]. PHPMA is currently frequently used as a macromolecular carrier for low molecular weight drugs, especially anticancer chemotherapeutic agents, to enhance the therapeutic efficacy and limit the side effects [32,34–36]. Intense research using PHPMA drug conjugates has gained momentum and has found uses in many different applications [37,38], with PHPMA copolymers considered a good alternative hydrophilic polymer to polyethylene oxide (PEO) because of the immunogenic reactions reported for the former [39,40].

The synthesis of the PHPMA copolymer is mainly carried out by CLRP. The ATRP of HPMA was implemented for the first time by Matyjaszewki et al. [41]. However, the polymerization proceeded in an uncontrolled manner, resulting in PHPMA copolymers with broad molecular weight distributions and low conversions. The controlled polymerization of HPMA by ATRP has been recently revised towards high monomer conversions and narrow dispersities [42]. In 2005, McCormick et al. [43] synthesized a PHPMA copolymer with a defined molecular weight and low $Đ$ using the RAFT method under aqueous conditions. Later in 2013, Özdemir et al. [31] reported on the RAFT-mediated synthesis of PHPMA macroCTA in MeOH and PHPMA-*b*-4-vinylpyridine block copolymer in DMF or MeOH by conventional and MWI heating methods at 70 °C using 4-cyano-4-(((ethylthio)carbonothioyl)thio)pentanoic acid as chain transfer agent and AIBN as an initiator. Despite, good control over polymers molecular weight and composition the polymerizations were investigated only in MeOH for homopolymers resulting in low conversions ~40%.

Although to date, the RAFT method has been largely employed for the synthesis of PHPMA homo- and copolymers [44–46], the polymerization times are still relatively long, from several hours to almost a day.

Accounting for the aforementioned benefits of the MWI technique and the potential applications of PHPMA copolymers in the biomedical field, we herein investigate the preparation of PHPMA homo- and copolymers by MWI. We overview the MWI-assisted RAFT polymerization of HPMA in various solvents and use different chain transfer agents (CTAs), such as the commercial and widely used 4-cyano-4-(phenylcarbonothioylthio)pentanoic acid (named CTA1) and the synthesized 4-cyano-4-(((ethylthio)carbonothioyl)thio)pentanoic acid (named CTA2) in the presence of 4,4′-azobis(4-cyanovaleric acid) (V-501) as an initiator. Several different stoichiometric ratios between the monomer, CTA and initiator were tested. In addition, it has been demonstrated that copolymers can be produced, thus illustrating the "livingness" of the system. Also, the best conditions established for the RAFT-mediated homo- and copolymer formation by MWI were compared with the conventional heating method. Altogether, we provide a guideline for selecting the optimal conditions for the RAFT polymerization of HPMA to produce PHPMA homopolymers (named PHPMA macroCTAs – PHPMA-mCTA) and PHPMA-based copolymers using MWI-assisted polymerization.

2. Experimental section

2.1. Materials

Reagents included amino-2-propanol (93%), methacryloyl chloride (≥ 97.0%, distilled under an argon atmosphere), sodium hydride (NaH, 60% dispersion in mineral oil), ethanethiol (EtSH, 97%), carbon disulfide (CS_2, anhydrous, ≥ 99%), *tert*-butyl carbazate (Boc-hydrazide, 98%), triethylamine (Et_3N, ≥99.5%), 4,4′-azobis(4-cyanovaleric acid) (V-501, ≥ 98%), 4-cyano-4-(phenylcarbonothioylthio)pentomic acid (CTA1) and 2-(diisopropylamino)ethyl methacrylate (97%, distilled under an argon atmosphere). Dichloromethane (CH_2Cl_2, anhydrous ≥99.8%) was dried by refluxing over a benzophenone-sodium complex and distilled under an argon atmosphere. Other solvents included diethyl ether (Et_2O, ≥ 99.7%), dimethyl sulfoxide (DMSO, ≥ 99.5%), and *tert*-butanol (*tert*-BuOH, ≥ 99.5%). All reagents and solvents were purchased from Sigma-Aldrich.

The monomer *N*-(2-hydroxypropyl)methacrylamide (HPMA) (Scheme S1, Fig. S1) was synthesized according to reference [47]. *N*-(3-Boc-aminopropyl)methacrylamide (boc-APMA) was purchased from PubChem. Methacrylamide butyl carbazate with a hydrazine bond (MABH) (Scheme S2, Fig. S2) was synthetized according to reference [48]. The RAFT agent 4-cyano-4-(((ethylthio)carbonothioyl)thio)pentanoic acid (CTA2) (Fig. S3) was synthesized according to reference [49]. The detailed procedure of all the syntheses is provided in the ESI file.

2.2. Instruments and analyses

Microwave-assisted RAFT polymerizations were conducted on a Biotage Initiator Sixty microwave system. The monomers, CTA, PHPMA homopolymers and their copolymers were characterized by proton nuclear magnetic resonance (^{1}H NMR) spectroscopy. ^{1}H NMR spectra were recorded on a Bruker Avance (600 MHz) spectrometer with $CDCl_3$, methanol-d_4 or D_2O (acidified with DCl; pH ~ 3.0) as the solvent at 295 K.

The apparent average molecular weights ((i.e., number-average molecular weight (M_n) and weight-average molecular weight (M_w)) and the molecular weight distribution or dispersity ($Đ$) of the homo- and copolymers were determined by size exclusion chromatography (SEC) using an HPLC Ultimate 3000 system (Dionex, USA) equipped with an SEC column (TSKgel SuperAW3000 150 × 6 mm, 4 μm) and three detectors: ultraviolet/visible (UV/VIS), refractive index (RI, Optilab®-rEX) and multiangle light scattering (MALS, DAWN EOS) (Wyatt Technology Co., USA). A mixture (80/20 vol%) of methanol and sodium acetate buffer (0.3 M, pH = 6.5) was used as the mobile phase.

2.3. Kinetic study of the RAFT polymerization of HPMA using MWI (Scheme 1)

RAFT experiments were performed in Biotage high-precision MW glass vials (2 mL) and conducted in a laboratory MW reactor (Biotage Initiator Robot Sixty). The MW instrument was set to normal voltage with a prestirring step of 60 s. A typical procedure for kinetic studies was as follows: A stock solution was prepared of HPMA (1.2 g, 3.99×10^{-5} mol at DP 175), CTA and initiator V-501 ([CTA]/[I] 1/0.5 and 1/0.2) in certain amounts of DMSO, *tert*-BuOH and/or deionized water. Two different CTA agents (CTA1 and CTA2) were investigated in HPMA mCTA synthesis, where the experimental conditions were kept the same for both cases. An aliquot (1 mL) from a stock solution was obtained and transferred to five or six glass vials equipped with a magnetic stir bar, which were sealed and deoxygenated for 30 min using argon purging. Afterwards, the vials were placed in the cavity of the MW instrument, and the temperature was set to 70 °C, with a reaction time of 60 min to 12 h (when necessary) for a total of five to six experiments. At different time points, the polymerization was stopped by ceasing MWI, removing the vial from the instrument and rapidly quenching in liquid nitrogen. The sample solution (20 μL) was immediately analyzed by ^{1}H NMR spectroscopy. The monomer conversion was calculated by comparing the remaining monomer concentration with the initial monomer feed. The remaining fraction of the sample solution was precipitated into cold acetone or an acetone/ether mixture 3/1 (*v*/v) for molecular weight analysis. The RAFT polymerization of HPMA under various reaction conditions and solvents is presented in Tables 1 and 2 and Tables S1 to S3 (ESI). In addition, the best conditions established for the RAFT-

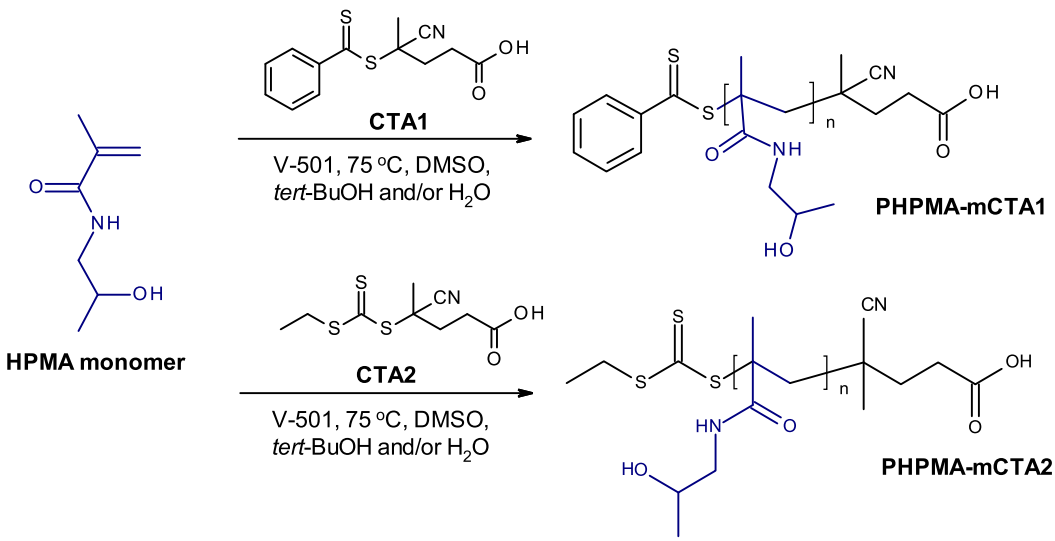

Scheme 1. General synthetic procedure for MWI-assisted RAFT polymerization of the monomer HPMA to produce PHPMA-mCTAs using 4-cyano-4-(phenylcarbonothioylthio)pentanoic acid (CTA1) and 4-cyano-4-(((ethylthio)carbonothioyl)thio)pentanoic acid (CTA2) as RAFT agents.

Table 1
Microwave-assisted RAFT polymerization of HPMA in water. Conversion data, number-average molecular weight (M_n) and dispersity ($Đ$) for MWI-assisted RAFT polymerization of HPMA. V-501 as the initiator in a molar ratio of [M]/[CTA]/[I] = 175/1/0.2 for the target $M_n \sim 25000$ g·mol^{-1}.

	Time (h)	Conv.[a] (%)	$M_{n,th}$[b] ^{1}H NMR (g·mol^{-1})	M_n, SEC (g·mol^{-1})	$Đ$
CTA1	0.5	20	5 340	2530	1.95
	1	28	7 295	10420	1.08
	1.5	36	7 796	14950	1.05
	2.0	47	12060	17950	1.04
	3.0	58	14810	22040	1.04
	4.0	56	12810	22750	1.05
CTA2	0.5	12	3 150	4300	1.19
	1	40	9 875	9000	1.16
	1.5	50	12280	12400	1.13
	2	61	14920	15600	1.09
	3.0	71	18970	19200	1.08
	4.0	80	21080	24200	1.09

[a] Conversion data determined by ^{1}H NMR analysis. [b] Theoretical $M_n = [M]_0/[CTA]_0 \times$ conv. $\times M_{WHPMA} + M_{WCTA}$.

mediated homopolymer formation by MWI were compared with the polymerization by the conventional heating method (Table S4).

2.4. Synthesis of PHPMA-b-bocAPMA, PHPMA-b-PMABH and PHPMA-b-PDPA copolymers via MWI (Scheme 2)

MWI-assisted RAFT copolymerization was carried out as follows: PHPMA-mCTA2, 0.1 g (2.43×10^{-5} mol) ($M_{n(NMR)} \sim 4130$ g·mol^{-1}) was dissolved in *tert*-BuOH (2 mL), different amounts of the Boc-protected monomers *N*-(3-Boc-aminopropyl)methacrylamide (bocAPMA) (B1, Scheme 2), methacrylamide butyl carbazate (MABH) (B2, Scheme 2) or 2-(diisopropylamino)ethyl methacrylate (DPA) (B3, Scheme 2) and the initiator V-501 (0.5 mol·L^{-1}, related to PHPMA-mCTA) were dissolved in *tert*-butanol (4 mL), and these solutions were added to a 10–20 mL MW glass vial with a magnetic stir bar, which was sealed and then purged with argon for 30 min. Next, the reaction vial was placed in the cavity of the MW instrument, and the temperature was programmed to 70 °C. After 6 h, the polymerization was stopped with a quenching step using liquid nitrogen. The yellowish reaction product was precipitated into cooled diethyl ether, filtered, washed three times with diethyl ether, and then dried overnight at room temperature under vacuum. After purification, the structure of the copolymers was confirmed by ^{1}H NMR spectroscopy, and the M_n was determined by ^{1}H NMR spectroscopy and SEC. The macromolecular characteristics of the PHPMA-*b*-bocAPMA (BC1, Scheme 2), PHPMA-*b*-PMABH (BC2, Scheme 2) and PHPMA-*b*-PDPA (BC3, Scheme 2) copolymers are depicted in Table 2. The conventional heating method for the copolymer synthesis was carried out at the same conditions as mention above for comparison. The macromolecular characteristics of the block copolymers are listed in Table S5 (ESI).

3. Results and discussion

3.1. Kinetic study of microwave-assisted RAFT polymerization of HPMA

To identify and optimize the conditions for the preparation of well-defined PHPMA homo- and copolymers via MWI using RAFT polymerization, several parameters were evaluated. Careful selection of the CTA was necessary for successful RAFT polymerization. Two different CTA

Table 2
Experimental conditions and macromolecular characteristics of the block copolymers prepared via microwave-assisted RAFT polymerization.

Sample	$[M]_0/[CTA]_0/[I]_0$	Time (h)	Conv. (%)	$M_{n,NMR}$[c] (g·mol^{-1})	$M_{n,SEC}$ (g·mol^{-1})[d]	$Đ$
PHPMA$_{29}$-mCTA2	100/1/0.2	3	93[a]	4130	4410	1.04
PHPMA$_{29}$-*b*-bocAPMA$_{47}$ (BC1)	75/1/0.5	6	96[a]	15500	25000	1.06
PHPMA$_{29}$-*b*-PMABH$_{44}$ (BC2)	75/1/0.5	6	30[a]	12208	22200	1.38
PHPMA$_{29}$-*b*-PDPA$_{34}$ (BC3)	75/1/0.5	6	45[b]	11851	13720	1.14

[a] Determined by ^{1}H NMR spectroscopy in methanol-d_4 or using end-group analysis.
[b] Determined by 1H NMR in acidic D2O using end-group analysis.
[c] M_n was calculated via ^{1}H NMR spectroscopy according to $M_n = (n\text{MU} \times M_{W\ HPMA}) + (n\text{MU} \times M_{W\ monomer}) + M_{WCTA}$ Eq. 1.
[d] Determined by SEC in MeOH/acetate buffer, pH 6.5, 80/20 vol%.

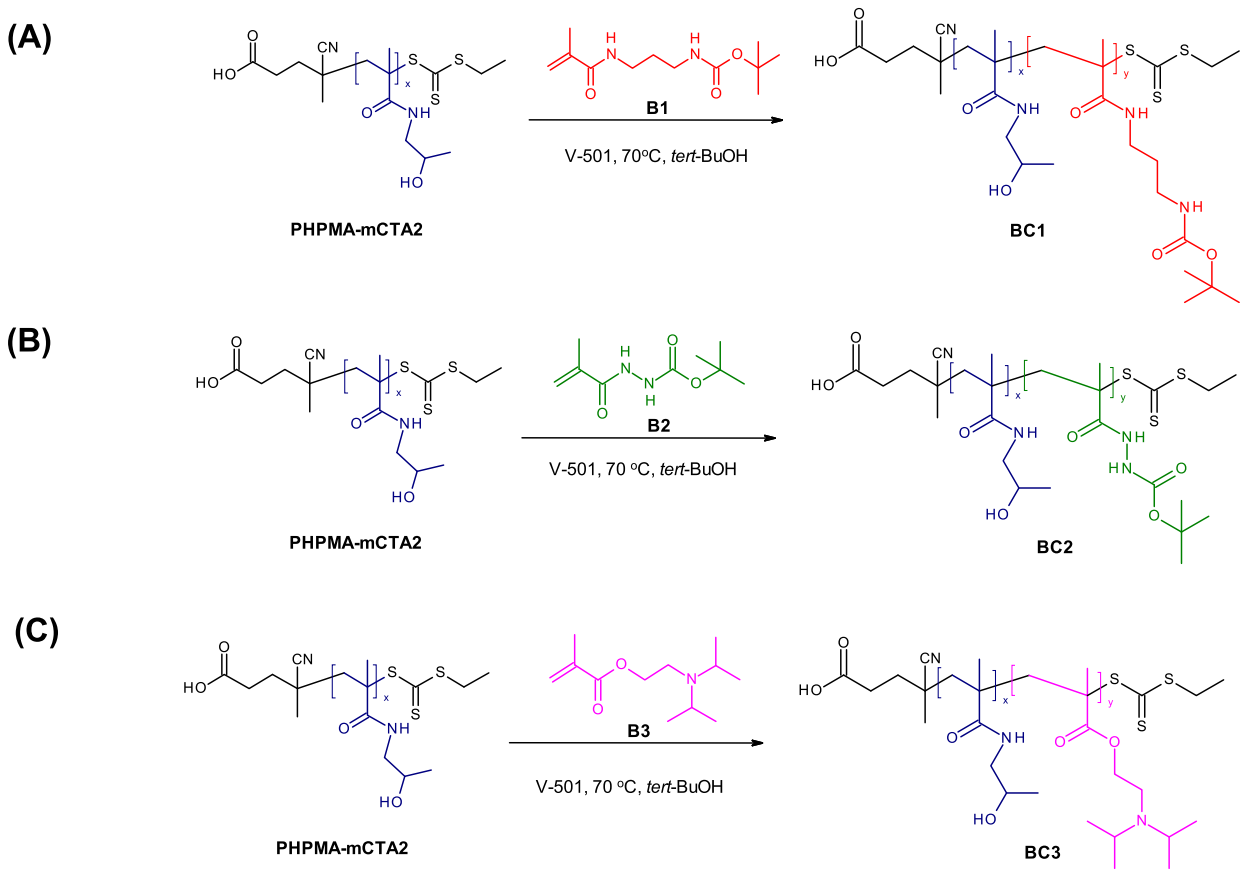

Scheme 2. RAFT-mediated synthesis of diblock copolymers via MWI. (A) PHPMA-*b*-bocAPMA (BC1), (B) PHPMA-*b*-PMABH (BC2) and (C) PHPMA-*b*-PDPA (BC3).

agents, namely, commercial 4-cyano-4-(phenylcarbonothioylthio)pentanoic acid (CTA1) and synthesized 4-cyano-4-(((ethylthio)carbonothioyl)thio)pentanoic acid (CTA2), were investigated in the synthesis of HPMA mCTAs (Scheme 1). These CTAs are known to generally perform well in the polymerization of methacrylates and methacrylamides [46,49]. We targeted a molecular weight of 25,000 g·mol^{-1} for PHPMA because it is below the threshold allowing renal clearance and avoiding polymer accumulation, envisaging further biological applications [50]. All polymerizations were carried out in a MW reactor at 70 °C with 4,4′-azobis(4-cyanovaleric acid) (V-501) as the initiator. The reactions were monitored to determine the conditions of the initial reaction kinetics. The impact of the selected CTA and the variation in the initiator concentration and solvent on the Rp, the control of the polymerization, and the quality of the final polymer (low $Đ$ and higher M_n) obtained were assessed.

The study began with preliminary screening experiments aiming to provide a rapid polymerization of HPMA with the commercial and widely used CTA1 in the presence of V-501 in molar ratio [M]/[CTA]/[I] = 175/1/0.5 (relatively high initiator concentration and aprotic organic solvent – DMSO). DMSO was chosen for the RAFT polymerization of HPMA because all chemical reagents are very well dissolved in this solvent. The given conversion data obtained by ^{1}H NMR and the M_n and dispersity ($Đ$) obtained by SEC for microwave-assisted RAFT polymerization of HPMA at a molar ratio of [M]/[CTA]/[I] = 175/1/0.5 are summarized in Table S1 (ESI). The obtained results clearly indicated no linear increase in molecular weight with the polymerization time, high dispersity and very poor conversions, reaching a maximum of ~25% conversion for CTA1. The M_n values were closer to each other, showing that longer polymerization times are not necessary for these selected reaction conditions (Table S1, ESI). For CTA2, the monomer conversions were reasonably good, reaching ~75%, with almost the desired targeted M_n (~ 25,000 g·mol^{-1}); however, minimal control over the molecular weight and reasonably low dispersity ($Đ \leq 1.2$) were achieved (Table S1, CTA2, ESI). As observed for CTA1, the similar molecular weights obtained within 4 h and 5 h for CTA2 demonstrate that longer polymerization times are not necessary for these selected reaction conditions. A possible explanation for the obtained results could be the solvent chosen for polymerization, which could negatively influence the polymerization process.

Recently, Thang et al. conducted a deep and detailed study on the effect of solvents on the conventional thermal RAFT polymerization of HPMA [51]. The authors determined that the hydrogen bonding between polymer chains in aprotic solvents has a negative influence on the RAFT polymerization process. In aprotic solvents such as DMSO, the deviation from linearity can be attributed to radical loss, most likely due to radical-radical termination resulting in dead chains and thus low conversions [51]. Moreover, it should be noted that MWI absorbed by the solvents could affect the polymerization. The ability of DMSO to convert MW energy into heat is determined by the so-called loss tangent (tan δ), where for DMSO, tan $\delta = 0.825$, which means that it has ultra-high MW absorption [52]. High MW absorption solvents used for RAFT polymerization have been reported to lead to significant chain-end loss, potentially resulting from unintentionally high initial temperatures in the reaction medium, which lead to chain transfer or other side reactions during polymerization [15]. Indeed, under the above reaction conditions, it was generally not possible to achieve good control (in particular, low $Đ$) for both CTAs. In response to this challenge, appropriate reaction conditions were investigated to enable good control (i.e., low $Đ$, predictable molar mass, shorter polymerization times) over the polymerization of HPMA.

Compared to DMSO, *tert*-BuOH is a moderately polar solvent with a slightly lower ability to convert MW energy into heat (tan $\delta = 0.80$),

which makes it very attractive for use in MWI synthesis and might contribute to a faster reaction rate. Indeed, Cunningham et al. pioneered the conventional polymerization of amino-containing monomers such as dialkylamino ethyl methacrylates in *tert*-BuOH, with good control and livingness [53]. Moreover, although *tert*-BuOH is a nontoxic, relatively inexpensive solvent, to the best of our knowledge, it has never been used for MWI-assisted RAFT polymerization of HPMA. Accordingly, we evaluated the efficiency of *tert*-BuOH as a solvent for RAFT polymerization by MWI for polymer synthesis at the same molar ratios as those used for DMSO - [M]/[CTA]/[I] = 175/1/0.5.

The results are depicted in Table S2 (ESI). The polymer conversion increased to ~52% for CTA1 and to 80% for CTA2, whereas the molecular weight was not controlled during the first 5 h of polymerization in both cases (Table S2, ESI). Similarly, the agreement between theoretical and experimental molecular weights was not consistently good, but the $Đ$ values of the polymers obtained during the homopolymerizations were consistently low (see Table S2). Until now, in all experiments, the Rp by MWI was significantly slow. Therefore, under the abovementioned reaction conditions, we had never reached the target M_n (~ 25,000 g·mol^{-1}) within a relatively short time – a few hours. These issues could most likely be because of an inappropriate selection of molar ratios between CTA and initiator, [CTA]/[I] = 1/0.5. Indeed, it is known in RAFT polymerization that the total active species concentration influences the Rp, where a decrease in the total active species concentration generally positively affects the Rp [53,54].

To obtain the target M_n, the amount of initiator, V-501, with respect to CTAs was reduced by 2.5 times, with all the other parameters kept constant. At a molar ratio of [M]/[CTA]/[I] = 175/1/0.2, the polymerization rate was still quite slow (at maximum time = 12 h); however, the obtained molecular weights, dispersities and conversion data showed that the polymerization of HPMA by both CTAs proceeded in a controlled fashion, producing polymers with low $Đ$, as seen in Table S3 (ESI). The controlled living character of the MWI-assisted RAFT of HPMA was demonstrated by the linear curve obtained by plotting the natural logarithm of the total monomer concentration versus time for the molar ratio [M]/[CTA]/[I] = 175/1/0.2 in *tert*-BuOH (Fig. S4A, ESI). The RAFT polymerization proceeded to high conversions with increasing reaction time. The pseudo-first-order kinetic plot showed a linear increase in the molecular weight with conversion and low dispersity ($Đ$ ~ 1.03 to 1.04 at the 12th h). According to the time-dependent conversion data, PHPMA-mCTA1 was formed in a controlled manner (blue lines, Fig. S4B, ESI). Similarly, for CTA2 at the same molar ratio ([M]/[CTA]/[I] = 175/1/0.2), the polymerization followed a pseudo-first-order kinetic plot, showing a linear increase in molecular weight with the polymerization time; however, a more controlled fashion was exhibited (red lines, Fig. S4B and Table S3, ESI) than that observed for the polymerization using CTA1 (blue lines, Fig. S4 and Table S3, ESI). In addition, good agreement between theoretical and experimental molecular weights was achieved, and the dispersity of the homopolymers was always low ($Đ$ ~ 1.04 at the 12th h, Fig. S4, ESI).

The SEC chromatograms of PHPMA-mCTA1 (Fig. S5A) and PHPMA-mCTA2 (Fig. S5B) at the corresponding molar ratios show a monomodal distribution, as indicated by the overlap of the SEC traces. Nevertheless, the SEC traces revealed a shift to lower elution volumes as a function of polymerization time, indicating an increase in molecular weight (Table S3). Altogether, these results suggested that MWI-assisted RAFT polymerization of HPMA implemented in *tert*-BuOH and at these selected stoichiometries using both CTAs proceeds in a controlled manner, with outstanding results obtained for CTA2.

We next explored the opportunities for clean processing and pollution prevention by choosing another solvent such as water. We searched numerous publications reporting the combination of water as an environmentally benign solvent for chemical transformations with the application of MWI as an efficient heating method [55–58]. Water is inexpensive, readily available, nontoxic, and nonflammable presenting clear advantages as a solvent for use in organic synthesis. Furthermore, as a MW-absorbing solvent, water has a medium loss tan δ of 0.123 [52], making it very suitable for MW-assisted synthesis. Moreover, it is worth mentioning that the HPMA monomer is highly soluble in aqueous medium, which makes water an excellent solvent for RAFT polymerization of HPMA by MWI. Accordingly, we performed the same set of experiments but used water as a solvent.

As a typical polymerization procedure, the molar ratio between the monomer, free RAFT agent and initiator was kept as [M]/[CTA]/[I] = 175/1/0.2 for both CTAs, as previously used for *tert*-BuOH (Table S3). The polymerization was carried out at 70 °C for different times (0.5–4 h). Examining the kinetic plots of $\ln([M]_o/[M]_t)$ for both CTAs versus polymerization time, the plots were linear for CTA2 (Fig. 1A). The conversion of the HPMA monomer versus molecular weight and dispersity was also linear, indicating that RAFT polymerization proceeded in a well-controlled fashion (Fig. 1B).

The results clearly indicated that PHPMA-mCTA was obtained with a higher conversion in water, and the polymerization time was four times faster (Table 1) than that with DMSO (Table S1) or *tert*-BuOH (Table S2 and S3). Therefore, under the reaction conditions, we obtained the desired target M_n (~ 25,000 g·mol^{-1}) within a relatively short period of time (4.0 h, CTA2). As comparison, the experimental set ([M]/[CTA]/[I] = 175/1/0.2) was performed by the conventional heating method using both CTAs, as previously reported for water (Table 1). The obtained results show a slightly slow reaction rate, broader dispersity's and homopolymer conversion (~48% for CTA1; 65% for CTA2, Table S4) if compared with the MWI (Table 1) pointing out the better choice towards obtention of HPMA homopolymers by MWI via RAFT in water.

SEC measurements were conducted for all samples from the kinetic study by MWI in water. The elution profile changes for PHPMA-mCTA1 and PHPMA-mCTA2 are shown in Fig. 2 (A) and (B), respectively, and the maxima of the various peaks (M_n) are reported in Table 1. The unimodal SEC traces indicate that homopolymerization in corresponding ratios occurs in a controlled manner; similar results were obtained in the synthesis of HPMA by RAFT in *tert*-BuOH for both CTAs and in water for CTA2, as judged by SEC traces exhibiting shifts towards higher molecular weights, which indicated good livingness and control during the synthesis of the macroRAFT agents (Fig. 2B).

Although the SEC data for CTA1 show reasonable M_n values, pseudo-first-order kinetic plots were not achieved, and the M_n values obtained by NMR were far from those obtained by SEC. This discrepancy is likely because CTA1 could be degraded in water at 70 °C [59], and the chain-end functionality of the growing chain might have been compromised. If (nearly) all of the polymer chains contained a dithiobenzoate group, then the UV and RI traces would be almost identical. An increasing fraction of dead chains (i.e., those not containing a dithiobenzoate moiety at their end) results in greater deviation between the UV and RI traces. This deviation could be evaluated by observing possible discrepancies among the SEC-UV, SEC-RI and SEC-LS data [53]; indeed, from the SEC analyses, discrepancies specially among the SEC-UV and SEC-RI results were observed for the CTA1 suggesting that the growing chain from CTA1 could be compromised (Fig. S6A, ESI file).

3.2. Microwave-assisted block copolymerization (Scheme 2)

Ultimately, the livingness and end-group functionality of the previously synthesized PHPMA-mCTA2 was verified by growing a second block via MWI-assisted RAFT polymerization. We selected monomers that are relevant in the biological field, such as *N*-(3-Boc-aminopropyl) methacrylamide (bocAPMA) (B1, Scheme 2), methacrylamide butyl carbazate (MABH) (B2, Scheme 2) and 2-(diisopropylamino)ethyl methacrylate (DPA) (B3, Scheme 2), that have already been tested in several biological experiments in in vitro and in vivo models. For instance, B1 can be further deprotected and used for small interfering RNA (siRNA) delivery [60] or functionalized for imaging and diagnostics [61]; B2 is an example of a successful pH-labile hydrazone linkage-based copolymer of HPMA and can be functionalized with

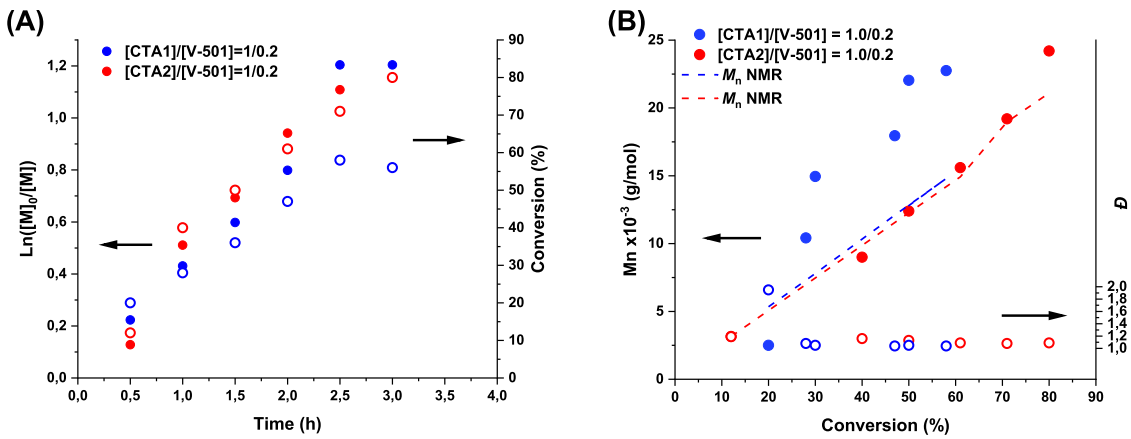

Fig. 1. (A) Semilogarithmic plots and (B) molecular weight and dispersity versus conversion of microwave-assisted RAFT polymerization of HPMA in water.

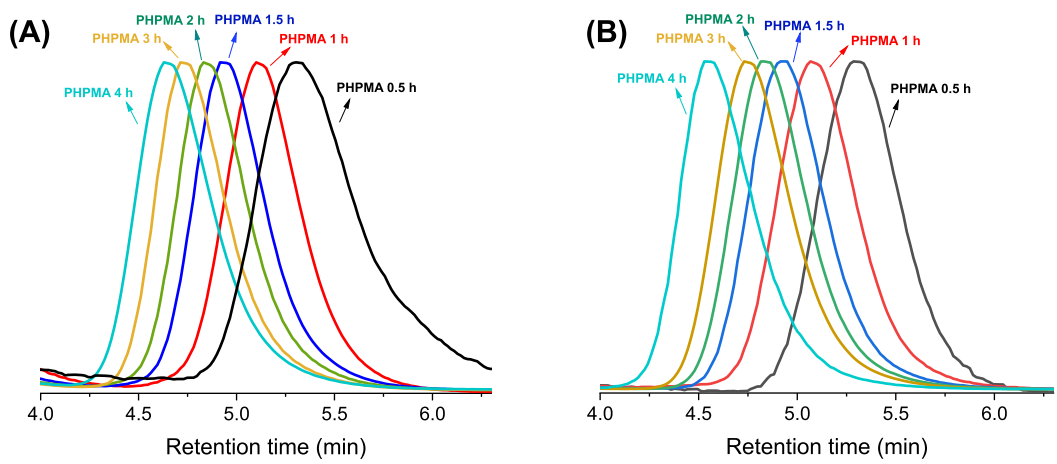

Fig. 2. SEC traces in MeOH/acetate buffer of PHPMA-mCTA1 (a) (CTA1, Table 1) and PHPMA-mCTA2 (b) (CTA2, Table 1) at varying polymerization times.

several drugs [47,48,61,62] for pH-controlled activation; and B3 is an ultra-pH-sensitive monomer that undergoes a hydrophobic/hydrophilic switch within a small pH window of 6.30 < pH < 6.95, which is remarkably close to the pH in the microenvironment of tumor cells, making the block copolymer useful for supramolecular self-assembly towards several structures with a myriad of applications [63–69].

The selection of mCTA2 was based on the most favorable results obtained during the kinetic studies. PHPMA-*b*-bocAPMA (BC1, Scheme 2), PHPMA-*b*-PMABH (BC2, Scheme 2) and PHPMA-*b*-PDPA (BC3, Scheme 2) copolymers were successfully synthesized via MWI-assisted RAFT polymerization. Mediated polymerization of copolymers BC1-BC3 was carried out in the presence of V-501 as an initiator at 70 °C, with a monomer/PHPMA-mCTA2/initiator molar ratio of 75/1/0.5 ($[M]_o/[CTA]_o/[I]_o$) (copolymers BC1 - BC3, Scheme 2, Table 2) in *tert*-BuOH (selected because has lower ability to convert MW energy to heat and due to the reagents and monomers shown reasonable solubility in the solvent). The BCs were successfully obtained (Table 2) with desirable M_n values, as judged by the SEC traces towards lower elution volumes, indicating an increase in molecular weights (Fig. 3). The composition of each BC copolymer was characterized by ^{1}H NMR spectroscopy. The ^{1}H NMR spectra of the diblock copolymers (BC1 – Fig. S7; BC2 – Fig. S8; BC3 – Fig. S9) showed the characteristic signals for the protons belonging to the HPMA, bocAPMA, MABH and DPA repeated units (Supplementary information). As comparison, the block copolymers were also prepared via the conventional heating method using the same aforementioned conditions (75/1/0.5 - $[M]_o/[PHPMAmCTA1]_o/[I]_o$). The obtained results demonstrated the

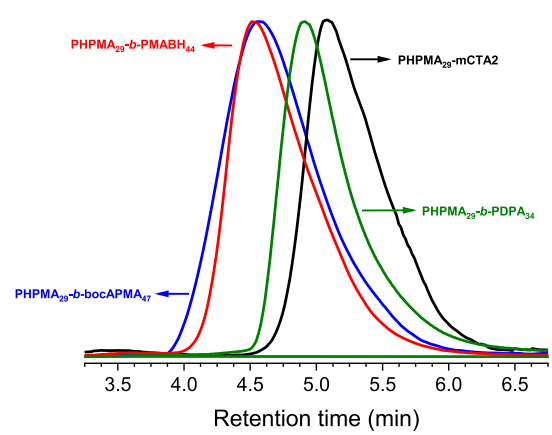

Fig. 3. SEC chromatograms in MeOH/acetate buffer of the $PHPMA_{29}$-mCTA2 (black lines) $PHPMA_{29}$-*b*-$bocAPMA_{47}$ (blue lines), $PHPMA_{29}$-*b*-$PMABH_{44}$ (red lines) and $PHPMA_{29}$-*b*-$PDPA_{34}$ (green lines) diblock copolymers (Table 2). (For interpretation of the references to colour in this figure legend, the reader is referred to the web version of this article.)

obtention of the BCs with generally broader dispersities and lower or similar conversions (~30% for BC1; 20% for BC2; 50% for BC3, Table S5) if compared with via MWI (Table 2). Differences between theoretical molecular weight (NMR) and experimental (SEC) observed can be because SEC has a strong dependence of its data on the calibrant,

solvent, column and it is a relative method therefore requiring a molecular weight detector, oppositely to the NMR that is absolute primary method requiring no calibration [70].

The monomers used are of great interest not only because they can readily polymerize with other vinylic monomers but also because they contain *tert*-Boc-protected multifunctional groups in their composition (for B1 and B2). Deprotection to a free amine can be easily carried out with a variety of reagents including HCl/MeOH, Me3Sil, or heat (185 °C) for subsequent future "universal" postreaction modifications for a myriad of applications, more than even the aforementioned biomedical applications. Notably, for BC2 and BC3, a lower conversion was observed for the growth of the second block. Since the same PHPMA-mCTA was used for the growth of BC1 (~ 96% conversion), we hypothesized that this result could not have been caused either by a low reinitiation efficiency of the macroRAFT agent or as a function of the decreased reinitiation efficiency because of the molecular weight of the macroRAFT agent (hindrance effect). The cause of these observed low conversions remains unclear and will be the subject of further investigations.

4. Conclusions

In this work, aspects of the kinetic study of MWI-assisted RAFT polymerization are discussed with a focus on certain advantages and limitations of various reaction conditions, providing some guidance for the selection of the right conditions for the polymerization of HPMA. Different CTAs, solvents, and molar ratios $[M]_o/[CTA]_o/[I]_o$ were investigated, aiming towards controlled molecular weights, conversions and dispersities. The kinetic experiments demonstrated that the aprotic polar solvent (DMSO) resulted in low conversions and poor controllability of the polymerization. A significantly well-controlled reaction was obtained at a molar ratio of $[M]_o/[CTA]_o/[I]_o = 100/1/0.2$ in *tert*-BuOH as the solvent, but with a relatively long reaction time ($t > 12$ h). Based on the results of this work, the MWI-assisted RAFT polymerization proceeds with good control over the molecular weight and composition if a monomer/CTA2/initiator feed ratio of 100/1/0.2 and water as the solvent are chosen. Furthermore, the RAFT polymerization of PHPMA-mCTA can be extended in a controlled fashion, resulting in nearly monodisperse copolymers, as demonstrated through the synthesis of the relevant PHPMA-*b*-bocAPMA, PHPMA-*b*-PMABH and PHPMA-*b*-PDPA diblock copolymers.

Author contributions

S.L.P and E.J. Conceptualization; S.L.P., V.S. and R.K. Data curation; V.S., S.L.P., R.K., M.H., and E.J. Methodology, Validation;; S.L.P., M.H., and E.J. Writing - review & editing; M.H. Resources, Funding acquisition; E.J. Supervision, Project administration, Funding acquisition. All authors have given approval to the final version of the manuscript.

Declaration of Competing Interest

The authors declare no conflict of interest.

Acknowledgments

This work was supported by Czech Science Foundation (Grant # 20-15077Y). M.H thanks the Ministry of Education, Youth and Sports of the Czech Republic (grant INTER-COST # LTC19032).

Appendix A. Supplementary data

Supplementary data to this article can be found online at https://doi.org/10.1016/j.reactfunctpolym.2021.104875.

References

[1] W.A. Braunecker, K. Matyjaszewski, Controlled/living radical polymerization: features, developments, and perspectives, Prog. Polym. Sci. 32 (2007) 93–146, https://doi.org/10.1016/j.progpolymsci.2006.11.002.
[2] P.B. Zetterlund, Y. Kagawa, M. Okubo, Controlled/living radical polymerization in dispersed systems, Chem. Rev. 108 (2008) 3747–3794, https://doi.org/10.1021/cr800242x.
[3] M.F. Cunningham, Controlled/living radical polymerization in aqueous dispersed systems, Prog. Polym. Sci. 33 (2008) 365–398, https://doi.org/10.1016/j.progpolymsci.2007.11.002.
[4] P.B. Zetterlund, S. Perrier, RAFT polymerization under microwave irradiation: toward mechanistic understanding, Macromolecules. 44 (2011) 1340–1346, https://doi.org/10.1021/ma102689d.
[5] J. Chiefari, Y.K. Chong, F. Ercole, J. Krstina, J. Jeffery, T.P.T. Le, R.T. A. Mayadunne, G.F. Meijs, C.L. Moad, G. Moad, E. Rizzardo, S.H. Thang, Living free-radical polymerization by reversible addition - fragmentation chain transfer: the RAFT process, Macromolecules. 31 (1998) 5559–5562, https://doi.org/10.1021/ma9804951.
[6] M. Destarac, On the critical role of RAFT agent design in reversible addition-fragmentation chain transfer (RAFT) polymerization, Polym. Rev. 51 (2011) 163–187, https://doi.org/10.1080/15583724.2011.568130.
[7] M.K. Georges, R.P.N. Veregin, P.M. Kazmaier, G.K. Hamer, Narrow molecular weight resins by a free-radical polymerization process, Macromolecules. 26 (1993) 2987–2988, https://doi.org/10.1021/ma00063a054.
[8] J.S. Wang, K. Matyjaszewski, Controlled/"Living" radical polymerization. atom transfer radical polymerization in the presence of transition-metal complexes, J. Am. Chem. Soc. 117 (1995) 5614–5615, https://doi.org/10.1021/ja00125a035.
[9] K. Matyjaszewski, J. Xia, Atom transfer radical polymerization, Chem. Rev. 101 (2001) 2921–2990, https://doi.org/10.1021/cr940534g.
[10] M. Ouchi, T. Terashima, M. Sawamoto, Transition metal-catalyzed living radical polymerization: toward perfection in catalysis and precision polymer synthesis, Chem. Rev. 109 (2009) 4963–5050, https://doi.org/10.1021/cr900234b.
[11] N. Ayres, Atom transfer radical polymerization: a robust and versatile route for polymer synthesis, Polym. Rev. 51 (2011) 138–162, https://doi.org/10.1080/15583724.2011.566402.
[12] W. Tang, K. Matyjaszewski, Effects of initiator structure on activation rate constants in ATRP, Macromolecules. 40 (2007) 1858–1863, https://doi.org/10.1021/ma062897b.
[13] C. Boyer, M.H. Stenzel, T.P. Davis, Building nanostructures using RAFT polymerization, J. Polym. Sci. Part A Polym. Chem. 49 (2011) 551–595, https://doi.org/10.1002/pola.24482.
[14] M.H. Stenzel, in: C. Barner-Kowollik (Ed.), Handbook of RAFT Polymerization, Wiley, 2008, pp. 315–372, https://doi.org/10.1002/9783527622757.
[15] W.L.A. Brooks, B.S. Sumerlin, Microwave-assisted RAFT polymerization, Isr. J. Chem. 52 (2012) 256–263, https://doi.org/10.1002/ijch.201100140.
[16] J.B. McLeary, F.M. Calitz, J.M. McKenzie, M.P. Tonge, R.D. Sanderson, B. Klumperman, Beyond inhibition: a ^{1}H NMR investigation of the early kinetics of RAFT-mediated polymerization with the same initiating and leaving groups, Macromolecules. 37 (2004) 2383–2394, https://doi.org/10.1021/ma035478c.
[17] J.B. McLeary, J.M. McKenzie, M.P. Tonge, R.D. Sanderson, B. Klumperman, Initialisation in RAFT-mediated polymerisation of methyl acrylateElectronic Supplementary Information (ESI) available: chemical structures of all species, Chem. Commun. (2004) 1950, https://doi.org/10.1039/b404857a. http://www.rsc.org/suppdata/cc/b4/b404857a/.
[18] D. Bogdal, P. Penczek, J. Pielichowski, A. Prociak, Microwave Assisted Synthesis, Crosslinking, and Processing of Polymeric Materials, 2003, pp. 194–263, https://doi.org/10.1007/b11051.
[19] R. Hoogenboom, U.S. Schubert, Microwave-assisted polymer synthesis: recent developments in a rapidly expanding field of research, Macromol. Rapid Commun. 28 (2007) 368–386, https://doi.org/10.1002/marc.200600749.
[20] S. Sinnwell, H. Ritter, Recent advances in microwave-assisted polymer synthesis, Aust. J. Chem. 60 (2007) 729, https://doi.org/10.1071/CH07219.
[21] M. Bardts, N. Gonsior, H. Ritter, Polymer synthesis and modification by use of microwaves, Macromol. Chem. Phys. 209 (2008) 25–31, https://doi.org/10.1002/macp.200700443.
[22] C. Marestin, R. Mercier, in: V. Polshettiwar, R.S. Varma (Eds.), Aqueous Microwave Assisted Chemistry, Royal Society of Chemistry, Cambridge, 2010, pp. 145–175, https://doi.org/10.1039/9781849730990.
[23] S.L. Brown, C.M. Rayner, S. Graham, A. Cooper, S. Rannard, S. Perrier, Ultra-fast microwave enhanced reversible addition-fragmentation chain transfer (RAFT) polymerization: monomers to polymers in minutes, Chem. Commun. 2145 (2007), https://doi.org/10.1039/b703386a.
[24] S.L. Brown, C.M. Rayner, S. Perrier, Microwave-accelerated RAFT polymerization of polar monomers, Macromol. Rapid Commun. 28 (2007) 478–483, https://doi.org/10.1002/marc.200600755.
[25] J.C. Hernández-Ortiz, G. Jaramillo-Soto, J. Palacios-Alquisira, E. Vivaldo-Lima, Modeling of polymerization kinetics and molecular weight development in the microwave-activated RAFT polymerization of styrene, Macromol. React. Eng. 4 (2010) 210–221, https://doi.org/10.1002/mren.200900047.
[26] R.M. Paulus, C.R. Becer, R. Hoogenboom, U.S. Schubert, High temperature initiator-free RAFT polymerization of methyl methacrylate in a microwave reactor, Aust. J. Chem. 62 (2009) 254, https://doi.org/10.1071/CH09064.
[27] Z. An, Q. Shi, W. Tang, C.-K. Tsung, C.J. Hawker, G.D. Stucky, Facile RAFT precipitation polymerization for the microwave-assisted synthesis of well-defined,

double hydrophilic block copolymers and nanostructured hydrogels, J. Am. Chem. Soc. 129 (2007) 14493–14499, https://doi.org/10.1021/ja0756974.
[28] D. Roy, A. Ullah, B.S. Sumerlin, Rapid block copolymer synthesis by microwave-assisted RAFT polymerization, Macromolecules. 42 (2009) 7701–7708, https://doi.org/10.1021/ma901471k.
[29] Y. Assem, A. Greiner, S. Agarwal, Microwave-assisted controlled ring-closing Cyclopolymerization of Diallyldimethylammonium chloride via the RAFT process, Macromol. Rapid Commun. 28 (2007) 1923–1928, https://doi.org/10.1002/marc.200700377.
[30] C.T. Nguyen, Q.D. Nghiem, D.-P. Kim, J. San Chang, Y.K. Hwang, Microwave assisted synthesis of high molecular weight polyvinylsilazane via RAFT process, Polymer (Guildf). 50 (2009) 5037–5041, https://doi.org/10.1016/j.polymer.2009.08.035.
[31] Z. Özdemir, M. Topuzoğulları, İ.A. İşoğlu, S. Dinçer, RAFT-mediated synthesis of poly(N-(2-hydroxypropyl)methacrylamide-b-4-vinylpyridine) by conventional and microwave heating, Polym. Bull. 70 (2013) 2857–2872, https://doi.org/10.1007/s00289-013-0993-1.
[32] B. Říhová, J. Kopeček, K. Ulbrich, V. Chytrý, Immunogenicity of N-(2-hydroxypropyl) methacrylamide copolymers, Die Makromol. Chemie. 9 (1985) 13–24, https://doi.org/10.1002/macp.1985.020091985103.
[33] J. Kopeček, P. Kopečková, HPMA copolymers: origins, early developments, present, and future, Adv. Drug Deliv. Rev. 62 (2010) 122–149, https://doi.org/10.1016/j.addr.2009.10.004.
[34] J. Khandare, T. Minko, Polymer–drug conjugates: progress in polymeric prodrugs, Prog. Polym. Sci. 31 (2006) 359–397, https://doi.org/10.1016/j.progpolymsci.2005.09.004.
[35] G. Pasut, F.M. Veronese, Polymer–drug conjugation, recent achievements and general strategies, Prog. Polym. Sci. 32 (2007) 933–961, https://doi.org/10.1016/j.progpolymsci.2007.05.008.
[36] B.S. Tucker, B.S. Sumerlin, Poly(N-(2-hydroxypropyl) methacrylamide)-based nanotherapeutics, Polym. Chem. 5 (2014) 1566–1572, https://doi.org/10.1039/C3PY01279D.
[37] X.-M. Liu, S.C. Miller, D. Wang, Beyond oncology — Application of HPMA copolymers in non-cancerous diseases, Adv. Drug Deliv. Rev. 62 (2010) 258–271, https://doi.org/10.1016/j.addr.2009.10.006.
[38] M. Vorobii, A. de los Santos Pereira, O. Pop-Georgievski, N.Y. Kostina, C. Rodriguez-Emmenegger, V. Percec, Synthesis of non-fouling poly[N-(2-hydroxypropyl)methacrylamide] brushes by photoinduced SET-LRP, Polym. Chem. 6 (2015) 4210–4220, https://doi.org/10.1039/C5PY00506J.
[39] P. Zhang, F. Sun, S. Liu, S. Jiang, Anti-PEG antibodies in the clinic: current issues and beyond PEGylation, J. Control. Release 244 (2016) 184–193, https://doi.org/10.1016/j.jconrel.2016.06.040.
[40] T.T. Hoang Thi, E.H. Pilkington, D.H. Nguyen, J.S. Lee, K.D. Park, N.P. Truong, The importance of poly(ethylene glycol) alternatives for overcoming peg immunogenicity in drug delivery and bioconjugation, Polymers (Basel) 12 (2020) 298, https://doi.org/10.3390/polym12020298.
[41] M. Teodorescu, K. Matyjaszewski, Atom transfer radical polymerization of (meth) acrylamides, Macromolecules. 32 (1999) 4826–4831, https://doi.org/10.1021/ma990175x.
[42] V. Raus, L. Kostka, Optimizing the cu-RDRP of N -(2-hydroxypropyl) methacrylamide toward biomedical applications, Polym. Chem. 10 (2019) 564–568, https://doi.org/10.1039/C8PY01569D.
[43] C.W. Scales, Y.A. Vasilieva, A.J. Convertine, A.B. Lowe, C.L. McCormick, Direct, controlled synthesis of the nonimmunogenic, hydrophilic polymer, poly(N -(2-hydroxypropyl)methacrylamide) via RAFT in aqueous media †, Biomacromolecules. 6 (2005) 1846–1850, https://doi.org/10.1021/bm0503017.
[44] V. Šubr, L. Kostka, J. Strohalm, T. Etrych, K. Ulbrich, Synthesis of well-defined Semitelechelic poly[N -(2-hydroxypropyl)methacrylamide] polymers with functional group at the α-end of the polymer chain by RAFT polymerization, Macromolecules. 46 (2013) 2100–2108, https://doi.org/10.1021/ma400042u.
[45] J.A. Alfurhood, H. Sun, C.P. Kabb, B.S. Tucker, J.H. Matthews, H. Luesch, B. S. Sumerlin, Poly(N-(2-hydroxypropyl)methacrylamide)–valproic acid conjugates as block copolymer nanocarriers, Polym. Chem. 8 (2017) 4983–4987, https://doi.org/10.1039/C7PY00196G.
[46] M. Barz, M. Tarantola, K. Fischer, M. Schmidt, R. Luxenhofer, A. Janshoff, P. Theato, R. Zentel, From defined reactive Diblock copolymers to functional HPMA-based self-assembled nanoaggregates, Biomacromolecules. 9 (2008) 3114–3118, https://doi.org/10.1021/bm800684b.
[47] K. Ulbrich, V. Šubr, J. Strohalm, D. Plocová, M. Jelínková, B. Říhová, Polymeric drugs based on conjugates of synthetic and natural macromolecules, J. Control. Release 64 (2000) 63–79, https://doi.org/10.1016/S0168-3659(99)00141-8.
[48] Z. Xu, K. Zhang, C. Hou, D. Wang, X. Liu, X. Guan, X. Zhang, H. Zhang, A novel nanoassembled doxorubicin prodrug with a high drug loading for anticancer drug delivery, J. Mater. Chem. B 2 (2014) 3433–3437, https://doi.org/10.1039/C4TB00128A.
[49] M. Danial, S. Telwatte, D. Tyssen, S. Cosson, G. Tachedjian, G. Moad, A. Postma, Combination anti-HIV therapy via tandem release of prodrugs from macromolecular carriers, Polym. Chem. 7 (2016) 7477–7487, https://doi.org/10.1039/C6PY01882C.
[50] M.E. Fox, F.C. Szoka, J.M.J. Fréchet, Soluble polymer carriers for the treatment of Cancer: the importance of molecular architecture, Acc. Chem. Res. 42 (2009) 1141–1151, https://doi.org/10.1021/ar900035f.
[51] X. Pan, F. Zhang, B. Choi, Y. Luo, X. Guo, A. Feng, S.H. Thang, Effect of solvents on the RAFT polymerization of N-(2-hydroxypropyl) methacrylamide, Eur. Polym. J. 115 (2019) 166–172, https://doi.org/10.1016/j.eurpolymj.2019.03.016.
[52] D. Dallinger, C.O. Kappe, Microwave-assisted synthesis in water as solvent, Chem. Rev. 107 (2007) 2563–2591, https://doi.org/10.1021/cr0509410.
[53] J. Arredondo, P. Champagne, M.F. Cunningham, RAFT-mediated polymerisation of dialkylaminoethyl methacrylates in tert -butanol, Polym. Chem. 10 (2019) 1938–1946, https://doi.org/10.1039/C8PY01803K.
[54] S. Perrier, 50th anniversary perspective: RAFT polymerization—A user guide, Macromolecules. 50 (2017) 7433–7447, https://doi.org/10.1021/acs.macromol.7b00767.
[55] J. Rigolini, B. Grassl, S. Reynaud, L. Billon, Microwave-assisted nitroxide-mediated polymerization for water-soluble homopolymers and block copolymers synthesis in homogeneous aqueous solution, J. Polym. Sci. Part A Polym. Chem. 48 (2010) 5775–5782, https://doi.org/10.1002/pola.24385.
[56] S. Schmitz, H. Ritter, Access to poly{N -[3-(dimethylamino)propyl](meth) acrylamide} via microwave-assisted synthesis and control of LCST-behavior in water, Macromol. Rapid Commun. 28 (2007) 2080–2083, https://doi.org/10.1002/marc.200700378.
[57] M. Lobert, R. Hoogenboom, C.-A. Fustin, J.-F. Gohy, U.S. Schubert, Amphiphilic gradient copolymers containing fluorinated 2-phenyl-2-oxazolines: microwave-assisted one-pot synthesis and self-assembly in water, J. Polym. Sci. Part A Polym. Chem. 46 (2008) 5859–5868, https://doi.org/10.1002/pola.22901.
[58] C. Guerrero-Sanchez, M. Lobert, R. Hoogenboom, U.S. Schubert, Microwave-assisted homogeneous polymerizations in water-soluble ionic liquids: an alternative and green approach for polymer synthesis, Macromol. Rapid Commun. 28 (2007) 456–464, https://doi.org/10.1002/marc.200600728.
[59] D.B. Thomas, A.J. Convertine, R.D. Hester, A.B. Lowe, C.L. McCormick, Hydrolytic susceptibility of dithioester chain transfer agents and implications in aqueous RAFT polymerizations †, Macromolecules. 37 (2004) 1735–1741, https://doi.org/10.1021/ma035572t.
[60] A.W. York, Y. Zhang, A.C. Holley, Y. Guo, F. Huang, C.L. McCormick, Facile synthesis of multivalent folate-block copolymer conjugates via aqueous RAFT polymerization: targeted delivery of siRNA and subsequent gene suppression, Biomacromolecules. 10 (2009) 936–943, https://doi.org/10.1021/bm8014768.
[61] L. Kostka, L. Kotrchová, V. Šubr, A. Libánská, C.A. Ferreira, I. Malátová, H.J. Lee, T. E. Barnhart, J.W. Engle, W. Cai, M. Šírová, T. Etrych, HPMA-based star polymer biomaterials with tuneable structure and biodegradability tailored for advanced drug delivery to solid tumours, Biomaterials. 235 (2020) 119728, https://doi.org/10.1016/j.biomaterials.2019.119728.
[62] T. Etrych, M. Šírová, L. Starovoytova, B. Říhová, K. Ulbrich, HPMA copolymer conjugates of paclitaxel and docetaxel with pH-controlled drug release, Mol. Pharm. 7 (2010) 1015–1026, https://doi.org/10.1021/mp100119f.
[63] L.J.C. Albuquerque, V. Sincari, A. Jäger, R. Konefał, J. Pánek, P. Černoch, E. Pavlova, P. Štěpánek, F.C. Giacomelli, E. Jäger, Microfluidic-assisted engineering of quasi-monodisperse pH-responsive polymersomes toward advanced platforms for the intracellular delivery of hydrophilic therapeutics, Langmuir (2019), https://doi.org/10.1021/acs.langmuir.9b01009 acs.langmuir.9b01009.
[64] Y. Wang, K. Zhou, G. Huang, C. Hensley, X. Huang, X. Ma, T. Zhao, B.D. Sumer, R. J. DeBerardinis, J. Gao, A nanoparticle-based strategy for the imaging of a broad range of tumours by nonlinear amplification of microenvironment signals, Nat. Mater. 13 (2014) 204–212, https://doi.org/10.1038/nmat3819.
[65] Y. Li, T. Zhao, C. Wang, Z. Lin, G. Huang, B.D. Sumer, J. Gao, Molecular basis of cooperativity in pH-triggered supramolecular self-assembly, Nat. Commun. 7 (2016) 13214, https://doi.org/10.1038/ncomms13214.
[66] A. Joseph, C. Contini, D. Cecchin, S. Nyberg, L. Ruiz-Perez, J. Gaitzsch, G. Fullstone, X. Tian, J. Azizi, J. Preston, G. Volpe, G. Battaglia, Chemotactic synthetic vesicles: design and applications in blood-brain barrier crossing, Sci. Adv. 3 (2017), e1700362, https://doi.org/10.1126/sciadv.1700362.
[67] C. Giacomelli, L. Le Men, R. Borsali, J. Lai-Kee-Him, A. Brisson, S.P. Armes, A. L. Lewis, Phosphorylcholine-based pH-responsive diblock copolymer micelles as drug delivery vehicles: light scattering, electron microscopy, and fluorescence experiments, Biomacromolecules. 7 (2006) 817–828, https://doi.org/10.1021/bm0508921.
[68] F.C. Giacomelli, P. Stepánek, C. Giacomelli, V. Schmidt, E. Jäger, A. Jäger, K. Ulbrich, pH-triggered block copolymer micelles based on a pH-responsive PDPA (poly[2-(diisopropylamino)ethyl methacrylate]) inner core and a PEO (poly (ethylene oxide)) outer shell as a potential tool for the cancer therapy, Soft Matter 7 (2011) 9316, https://doi.org/10.1039/c1sm05992k.
[69] B. Říhová, M. Kovář, Immunogenicity and immunomodulatory properties of HPMA-based polymers, Adv. Drug Deliv. Rev. 62 (2010) 184–191, https://doi.org/10.1016/j.addr.2009.10.005.
[70] J.U. Izunobi, C.L. Higginbotham, Polymer molecular weight analysis by ^{1}H NMR spectroscopy, J. Chem. Educ. 88 (2011) 1098–1104, https://doi.org/10.1021/ed100461v.

LANGMUIR Article
Cite This: Langmuir 2019, 35, 8363−8372
pubs.acs.org/Langmuir

Microfluidic-Assisted Engineering of Quasi-Monodisperse pH-Responsive Polymersomes toward Advanced Platforms for the Intracellular Delivery of Hydrophilic Therapeutics

Lindomar J. C. Albuquerque,*[†,‡] Vladimir Sincari,[†] Alessandro Jäger,[†] Rafal Konefał,[†] Jiří Pánek,[†] Peter Černoch,[†] Ewa Pavlova,[†] Petr Štěpánek,[†] Fernando C. Giacomelli,[‡] and Eliézer Jäger*[†]

[†]Institute of Macromolecular Chemistry, Heyrovského nám. 2, Prague 6 162 06, Czech Republic

[‡]Centro de Ciências Naturais e Humanas, Universidade Federal do ABC, Avenida dos Estados 5001, Santo André 09210-580, Brazil

Supporting Information

ABSTRACT: The extracellular and subcellular compartments are characterized by specific pH levels that can be modified by pathophysiological states. This scenario encourages the use of environmentally responsive nanomedicines for the treatment of damaged cells. We have engineered doxorubicin (DOX)-loaded pH-responsive polymersomes using poly([*N*-(2-hydroxypropyl)]-methacrylamide)-*b*-poly[2-(diisopropylamino)ethyl methacrylate] block copolymers ($PHPMA_m$-*b*-$PDPA_n$). We demonstrate that, by taking advantage of the microfluidic technology, quasi-monodisperse assemblies can be created. This feature is of due relevance because highly uniform nanoparticles commonly exhibit more consistent biodistribution and cellular uptake. We also report that the size of the polymer vesicles can be tuned by playing with the inherent mechanical parameters of the microfluidic protocol. This new knowledge can be used to engineer size-specific nanomedicines for enhanced tumor accumulation if the manufacturing is performed with previous knowledge of tumor characteristics (particularly the degree of vascularity and porosity). The pH-dependent DOX release was further investigated evidencing the ability of polymersome to sustain encapsulated hydrophilic molecules when circulating in physiological environment (pH 7.4). This suggests nonrelevant drug leakage during systemic circulation. On the other hand, polymersome disassembly in slightly acid environments takes place enabling fast DOX release, thereby making the colloidal carriers highly cytotoxic. These features encourage the use of such advanced pH-responsive platforms to target damaged cells while preserving healthy environments during systemic circulation.

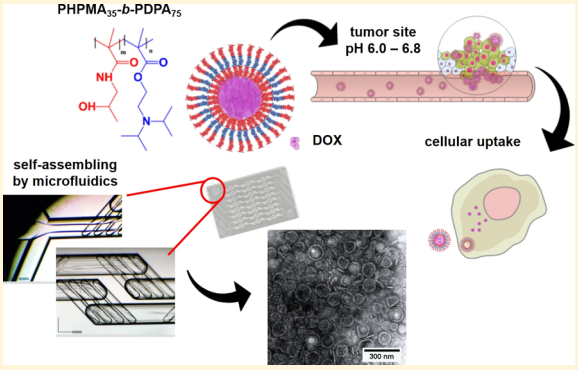

INTRODUCTION

Nowadays, it is widely accepted that the currently available cancer therapies have several drawbacks, and most of them are linked to the short blood circulation time of the antitumor agents and their low specificity. This can be circumvented, for instance, by loading the small molecules into supramolecular assemblies. The strategy presumably protects the active agent against degradation and clearance during the systemic circulation ideally driving it selectively to the sites of action where the damaged cells are present. The approach may enhance the therapeutic efficacy limiting the exposure of healthy tissues.[1,2] The selective drug targeting to solid tumors using nanoparticle-based technologies is centered on the known pathophysiology of such unhealthy sites. The combination of leaky microvasculature and missing or tight lymphatic capillary systems enables higher accumulation and retention of nano-sized supramolecular assemblies [enhanced permeability and retention (EPR) effect].[3−5] Moving beyond the EPR effect, the extracellular and subcellular compartments in tumor sites are characterized by a pH window that can also be modified by the pathophysiological state. The high metabolic rate of cancer cells leads to an accumulation of H^+ ions in the tumor microenvironment[6] and therefore, in contrast to healthy tissues, the extracellular pH of tumors is generally acidic (ranging from 6.2 to 6.8 depending on tumor aggressiveness). Furthermore, in the intracellular environment where the active agents are ideally delivered, the pH drops to ∼6.0 in early endosomes, to ∼5.5 in late endosomes, and to values smaller than ∼5.0 in lysosomes.[7,8] Accordingly, the usefulness of pH-responsive delivery systems responding in such pH range is clear. Particularly, polymer vesicles can be used for the loading of hydrophilic molecules within their aqueous compartment. They can be produced by the self-assembly of amphiphilic diblock copolymers when the polymer chains contain a high fraction of the hydrophobic component. Indeed, the polymer vesicles (known as polymersomes) have

Received: April 5, 2019
Revised: May 31, 2019
Published: June 2, 2019

Downloaded via ACADEMY OF SCIENCES CZECH REPUBLIC on September 16, 2022 at 16:24:10 (UTC).
See https://pubs.acs.org/sharingguidelines for options on how to legitimately share published articles.

ACS Publications © 2019 American Chemical Society

DOI: 10.1021/acs.langmuir.9b01009
Langmuir 2019, 35, 8363−8372

received great attention as delivery systems thanks to their ability to transport and protect small molecules during systemic circulation, their compartmentalization properties, and their higher stability when compared to liposomes. These advantages resulted in several examples of translation efforts into oncology, neurology, and immunology.[9−11] Nevertheless, one of the main drawbacks to be still circumvented is the typical manufacturing of highly polydisperse samples when using standard protocols of preparation (thin-film rehydration,[12−15] electroformation,[16] solvent-switch,[17] nanoprecipitation,[18] and pH-switch[19]) besides the presence of multiple morphologies, poor control over size, low drug loading content (LC), and low encapsulation efficiency.[20]

Taking into account the abovementioned considerations, we were motivated to explore the production of monodisperse pH-responsive polymersomes. The straightforward methodologies were already significantly investigated with notable achievements. Particularly, the control over particle size and enhanced encapsulation efficiency can be accomplished by varying the nanoprecipitation conditions.[21−23] Nevertheless, methodologies to reduce the polydispersity of soft-matter self-assembled nanostructures still deserve further investigations, and the use of microfluidic devices for such purpose[24] is an important strategy. The microfluidic technique was already successfully employed to control the size, shape and polydispersity of particles and capsules;[20,25] however, it has been seldom explored in the engineering of sub-200 nm polymersomes, particularly when simultaneously associated with the encapsulation of hydrophilic molecules. This has been herein explored with further evaluation of intracellular delivery and antitumor efficacy of doxorubicin (DOX)-loaded pH-responsive polymersomes. We have selected poly(2-(diisopropylamino)ethyl methacrylate) (PDPA) as the hydrophilic−hydrophobic pH-responsive block because of its $pK_a \approx 6.8$ and its ability to dissociate rapidly at pH < 6.8.[13,26] This is particularly important because the endocytosis is a reasonably fast process starting from plasma membrane wrapping up to the lysosomal stage in roughly 30 min.[27] Consequently, polymersomes must release their cargo within the cell cytosol in the time scale of a few minutes. The polymer poly(*N*-(2-hydroxypropyl)methacrylamide) (PHPMA) was chosen as the hydrophilic segment because of its protein-repelling characteristics and long blood circulation lifetime.[28,29]

■ METHODOLOGY

Materials and Chemicals. The monomer 2-(diisopropylamino)ethyl methacrylate (DPA, 97%, Sigma-Aldrich, Czech Republic) and methacryloylchloride (Sigma-Aldrich, Czech Republic) were purified by vacuum distillation prior to use. The initiator 4,4-azobis(4-cyanopentanoic acid) (V501, Sigma-Aldrich, Czech Republic) was recrystallized from methanol prior to use. The initiator 2,2′-azobis(2-methylpropionitrile) (AIBN, Sigma-Aldrich, Czech Republic), the chain-transfer agent 4-cyano-4-(phenylcarbonothioylthio)-pentanoic acid (CTA-COOH, Sigma-Aldrich, Czech Republic), and *N*-(3-dimethylaminopropyl)-*N*′-ethylcarbodiimide hydrochloride (EDC, Sigma-Aldrich, Czech Republic) were used as received. The solvents methanol (MeOH), dimethyl sulfoxide (DMSO), hydrochloric acid (HCl), *tert*-butanol, and 1,4-dioxane with the highest purity commercially available and the chemicals sodium sulfate (Na_2SO_4), magnesium sulfate ($MgSO_4$), sodium azide (NaN_3), 3-chloro-1-propanol, and DOX were purchased from Sigma-Aldrich (Czech Republic). The chemicals amino-2-propanol and 4-(dimethylamino)-pyridine (DMAP, 98%) were purchased from Fluka (Czech Republic). The fluorescent dyes dibenzylcyclooctyne-cyanine 3 (Cy3) and dibenzylcyclooctyne-cyanine 5 (Cy5) were purchased from Jena Bioscience (Germany). Dichloromethane (DCM) and acetone were purchased from Lachner (Czech Republic). All the solvents were dried over molecular sieves prior to use.

Synthesis of the Block Copolymers. *Synthesis of the Azide Chain-Transfer Agent (CTA-Azide).* CTA-azide was synthetized following the procedure described by Mendonça et al. with adaptions.[30] 3-Chloro-1-propanol (3 g, 31.7 mmol) and NaN_3 (3.5 g, 54.0 mmol) were dissolved in a mixture of acetone (50 mL) and water (5 mL) in a round-bottom flask and refluxed overnight. Acetone was removed under reduced pressure, and 35 mL of water was added to the remaining solution. The product was extracted with diethyl ether (3 × 70 mL) and the organic layer was dried over anhydrous Na_2SO_4. 3-Azido-1-propanol was obtained as a colorless oil (1.6 g, 53%) after solvent was removed under reduced pressure. The pure product was analyzed by Fourier transform infrared spectroscopy (FTIR). In the next step, a mixture of CTA-COOH (700 mg, 2.51 mmol), 3-azido-1-propanol (380 mg, 3.76 mmol), and dry DCM (40 mL) were added to a round flask equipped with a magnetic bar and a rubber stopper. The solution was cooled to 0 °C and filled with argon. Afterward, a solution of EDC (720 mg, 3.76 mmol) and DMAP (50 mg, 0.38 mmol) in DCM (10 mL) was added to the flask and allowed to react under argon atmosphere at 0 °C for 2 h and then at room temperature overnight. Then, the reaction mixture was stopped, washed with water (100 mL, 5 times), and dried over anhydrous Na_2SO_4. DCM was removed under reduced pressure and the crude product was purified by column chromatography [SiO_2 and hexane/ethyl acetate = 4/1 (v/v)]. The pure product (0.38 g, 42%) was analyzed by ^{1}H NMR and FTIR. All the methods are described in detail in the Supporting Information.

Synthesis of the Azide-Terminated PHPMA macroCTA. *N*-(2-Hydroxypropyl)methacrylamide (HPMA) monomer was prepared as previously described.[31] The synthesis of PHPMA macroCTA was conducted by RAFT polymerization. In a Schlenk tube equipped with a magnetic stirrer, HPMA monomer (1 g, 7 mmol) was dissolved in 6.62 mL of *tert*-butanol. The solution was filled with argon for 15 min and deoxygenated by three freeze−pump−thaw cycles. CTA-azide (118.4 mg, 0.326 mmol) and the initiator AIBN (33.2 mg, 0.204 mmol) were dissolved in 0.736 mL of DMSO. This solution was added to the Schlenk tube and another freeze−pump−thaw cycle was completed. The tube containing the pink solution was filled again with argon and placed into an oil bath at 70 °C to start the polymerization reaction that took place during 18 h and then quenched by exposing the reaction mixture to air and liquid nitrogen. The polymerization solution was precipitated in a cold mixture of acetone/diethyl ether (3/1) followed by a centrifugation step to isolate the product. The product was dissolved in a small amount of methanol and the azide-terminated PHPMA macroCTA was purified by Sephadex LH-20 using methanol as mobile phase. The product was precipitated in cold diethyl ether and vacuum-dried to yield a pink solid. The obtained polymer was characterized by size exclusion chromatography (SEC) and ^{1}H NMR.

Synthesis of Several Azide-Terminated Poly(N-(2-hydroxypropyl)methacrylamide)-b-(2-(diisopropylamino)-

DOI: 10.1021/acs.langmuir.9b01009
Langmuir 2019, 35, 8363−8372

ethyl methacrylate) ($PHPMA_m$-b-$PDPA_n$) Block Copolymers. In a Schlenk flask equipped with a magnetic stirrer, PHPMA macroCTA azide (500 mg) was dissolved in MeOH (10 mL) and different amounts of the monomer DPA dissolved in dioxane (15 mL) and the initiator AIBN dissolved in DMSO (100 μL) were mixed under stirring. The mixture was filled with argon for 15 min. Three freeze−pump−thaw cycles were performed, and the solution was filled again with argon for 15 min and placed into an oil bath at 70 °C to start the polymerization that took place during 18 h and then quenched by exposing the reaction mixture to air and liquid nitrogen. The block copolymers were obtained after dialysis against deionized water (pH ≈ 3) during 48 h. The used membrane had a molecular weight cut-off (MWCO) of 3.5−5.0 kDa and the water was changed every 12 h. The block copolymers were recovered by lyophilization and characterized by ^{1}H NMR and SEC.

Coupling of Azide-Terminated Poly(N-(2-hydroxypropyl)-methacrylamide)-b-(2-(diisopropylamino)ethyl methacrylate) ($PHPMA_{35}$-b-$PDPA_{75}$) to Cyanine 3-DBCO and Cyanine 5-DBCO. In an amber glass vial, 5.0 mg of the diblock copolymer was dissolved in 1 mL of dimethylformamide under stirring. The fluorescent dye (cyanine 3-DBCO or cyanine 5-DBCO) was added at molar ratio 3:1 (fluorescent dye/azide terminated group) and the reaction was carried out overnight in the dark. The solution was then dialyzed in a Float-A-Lyzer MWCO 3.5−5.0 kDa against water for 24 h to remove free dye and organic solvent. The Cy3-$PHPMA_{35}$-*b*-$PDPA_{75}$ and Cy5-$PHPMA_{35}$-*b*-$PDPA_{75}$ conjugates were recovered by lyophilization (yields of 58 and 32%, respectively).

Preparation and Characterization of Polymersomes. The $PHPMA_m$-*b*-$PDPA_n$ block copolymers were dissolved in tetrahydrofuran (THF)/MeOH (80/20) (v/v) to reach final concentrations of 5.0 mg mL^{-1}. Polymersomes were produced using the microfluidic device setup from Dolomite (Royston, United Kingdom) equipped with a glass micromixer chip with 12 mixing stage micro-channels of 50 μm × 125 μm (depth × width). The polymer solutions were pumped through the middle channel and phosphate-buffered saline (PBS) (pH 7.4) through the side channels using two independent Dolomite Mitos P-Pumps (Royston, United Kingdom) controlled via a computer software. The flow rates were adjustable parameters and the polymer colloids were collected in vials and dialyzed (MWCO 3.5−5 kDa) against PBS for 12 h to remove the organic solvent. The $PHPMA_{35}$-*b*-$PDPA_{75}$ polymersomes containing Cy3−Cy5 Förster resonance energy-transfer (FRET) pair dyes were also produced by microfluidics. The supramolecular polymer assemblies were characterized by dynamic light scattering (DLS), static light scattering (SLS), electrophoretic light scattering (ELS), transmission electron microscopy (TEM), and FRET measurements as described in detail in the Supporting Information.

DOX Encapsulation and Release. The anticancer drug DOX was encapsulated in the polymersomes by microfluidics. The drug was dissolved in 5 μL of DMSO and further mixed with the pre-prepared polymer solutions at 5.0 mg mL^{-1}. The DOX feeding was 1.0 mg (representing 20% w/w). The flow rates were preselected as 200 and 100 μL min^{-1} for water and organic phase, respectively. The polymer colloids were collected in vials and dialyzed against PBS for 24 h to remove the organic solvent and unloaded DOX. The loading content (LC) and loading efficiency (LE) of DOX were determined by high-performance liquid chromatography (HPLC) (Ultimate 3000 HPLC, Thermo Fisher Scientific) using a reverse-phase column Chromolith performance RP-18e (100−4.6 mm, eluent water−acetonitrile with acetonitrile gradient 0−100 vol %, flow rate = 1.0 mL min^{-1}). The analytical curve with linear response in the range 0.001−0.5 mg mL^{-1} was recorded and used to determine DOX contents. The values were calculated using the standard equations

$$\text{LC (\%)} = \frac{\text{DOX amount in polymersomes}}{\text{mass of polymersomes}} \times 100 \quad (1)$$

$$\text{LE (\%)} = \frac{\text{DOX amount in polymersomes}}{\text{DOX feeding}} \times 100 \quad (2)$$

The measurements were performed in triplicate and the mean values are reported.

The DOX cumulative release was evaluated in aqueous media with adjusted pH (7.4 and 5.5) at 37 °C by the dialysis method. A pre-swollen cellulose dialysis membrane tube with MWCO of 3.5−5.0 kDa (Spectra/Por Float-A-Lyzer G2) was filled with 2.0 mL of DOX-loaded polymersomes at a concentration of 0.5 mg mL^{-1}. The membrane tube was then immersed into 3 L of Milli-Q water at 37 °C and 350 rpm. Then, at predetermined times, 10 μL of the DOX-loaded polymersomes was removed and diluted into 190 μL of DMSO for determination of the remaining DOX measured by HPLC.

Biological Assays. *Cell Culture.* Mice breast 4T1 tumor cells and B16F10 melanoma cells were cultured in Dulbecco's modified Eagle's medium (DMEM) supplemented with 10% fetal bovine serum and antibiotic solutions (penicillin 10 000 U mL^{-1} and streptomycin 10 000 μg mL^{-1}) at 37 °C in 5% CO_2 atmosphere.

Cellular Uptake. Flow cytometry data were acquired to quantify the cellular uptake of DOX-loaded polymersomes as compared to the uptake of free DOX. The cells were cultured into 96-well plates at a density of 10 000 cells/well (B16F10) or 5000 cells/well (4T1) in the cell culture medium and incubated at 37 °C in CO_2 atmosphere for 24 h. The next day, the cell culture medium was replaced by solutions containing DOX-loaded polymersomes at a DOX concentration equal to 10 μg mL^{-1}. After incubation time (12 or 24 h), the cells were washed three times with PBS buffer followed by trypsinization, centrifugation, and resuspended in 200 μL of PBS medium for flow cytometry analysis. The acquisitions (10 000 events per sample) and data analysis were performed using a BD FACSVerse flow cytometer and the FlowJo software, respectively.

Cytotoxicity. B16F10 and 4T1 cells were plated into 96-well plates and allowed to adhere for 24 h. Subsequently, the cells were exposed to DOX-loaded polymersomes at different concentrations (the highest concentration was 1 μg mL^{-1}) diluted in culture medium for 24 h. The negative and positive controls refer to untreated cells and cells treated with concentrated H_2O_2 solution (1% H_2O_2 in DMEM). Cell viability was evaluated according to the Invitrogen alamarBlue protocol where 10 μL of the alamarBlue cell viability reagent (Life Technologies, Czech Republic) was added to each well and incubated for 3 h at 37 °C. The fluorescence of the reduced fluorescent dye was then measured with a Synergy H1 plate reader (BioTek Instruments, USA) at excitation λ = 570 nm and emission λ = 600 nm.[32] Complementarily, the cell viability of DOX-free (unloaded) polymersomes was probed by using the same protocol. The data are given as mean ±

DOI: 10.1021/acs.langmuir.9b01009
Langmuir 2019, 35, 8363−8372

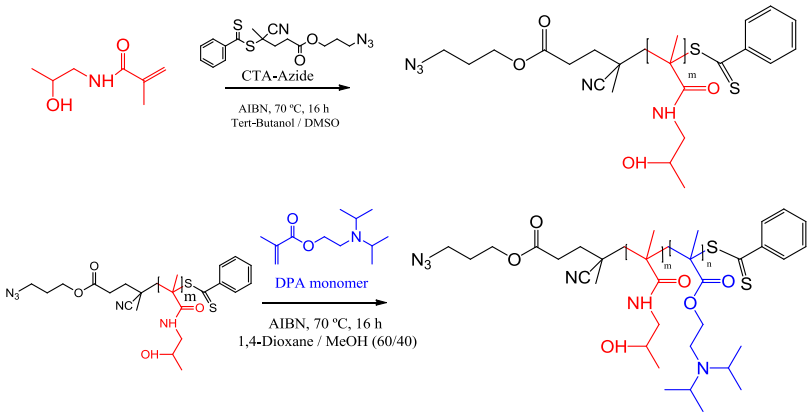

Figure 1. Synthetic route and molecular structure of the azide-terminated PHPMA macroCTA (top) and the diblock copolymers PHPMA$_m$-*b*-PDPA$_n$ (bottom).

Table 1. Synthesis Parameters and Molecular Characteristics of the Produced PHPMA$_m$-*b*-PDPA$_n$ Block Copolymers

block copolymer	$[M]_0/[CTA]_0/[I]$	M_n SEC (g·mol^{-1})	M_w/M_n	conversion (%)	yield (%)	wt (%) PHPMA
PHPMA$_{35}$-*b*-PDPA$_{26}$	50/2/1	10 600	1.25	69	53	53
PHPMA$_{35}$-*b*-PDPA$_{43}$	100/2/1	14 200	1.09	68	58	35
PHPMA$_{35}$-*b*-PDPA$_{75}$	150/2/1	21 000	1.05	72	56	24

standard deviation (SD) and statistical differences were determined by Student's unpaired *t*-test.

■ RESULTS AND DISCUSSION

Synthesis and Characterization of the Block Copolymers. The poly([*N*-(2-hydroxypropyl)]methacrylamide)-*b*-poly[2-(diisopropylamino)ethyl methacrylate] (PHPMA$_m$-*b*-PDPA$_n$) diblock copolymers were successfully synthetized by RAFT polymerization. First, the azide-terminated PHPMA macro chain-transfer agent (azide-macroCTA) was synthesized (M_n = 5000 g mol^{-1}, M_w/M_n = 1.06) and used as macroCTA. The FTIR, ^{1}H NMR, and SEC data are provided in the Supporting Information (Figures S1 and S2). Subsequently, the second block was grown from the macroCTA also by RAFT as depicted in Figure 1.

Although the azide groups are known to be unstable at high temperature as they might promote 1,3-cycloaddition reactions at polymerization environments (~70 °C);[30,33,34] this issue is minimized for methacrylamide monomers (such as HPMA) because of their low reactivity and the presence of the methylene group at the double bond of the monomer, thereby causing steric hindrance and precluding the undesirable side reactions.[30,35,36] Indeed, the presence of the azide groups in the final products was confirmed by FTIR spectroscopy (Figure S1—Supporting Information) and ^{1}H NMR spectroscopy where the presence of the methylene (CH_2) groups (m, l, k) adjacent to the azide group is seen (Figure S2—Supporting Information). Moreover, the azide group functionality was further confirmed by the effective coupling of the DBCO-cyanine dyes via a copper-free click chemistry reaction (discussed hereafter).

The weight-average molecular weight (M_w), number-average molecular weight (M_n), and polydispersity (M_w/M_n) of the polymer chains were estimated by SEC (Table 1 and Figure S3) and the values of M_w/M_n agree with those expected in RAFT polymerization of methacrylamides.[37] The degrees of conversion (~70%) are higher than those obtained by using methacrylate-based macroRAFT agent to initiate the polymerization of methacrylamide monomer (this approach was also tested). ^{1}H NMR (representatively available for PHPMA$_{35}$-*b*-PDPA$_{75}$ as shown in Figure 2) was used to determine the hydrophilic-to-hydrophobic weight ratios.

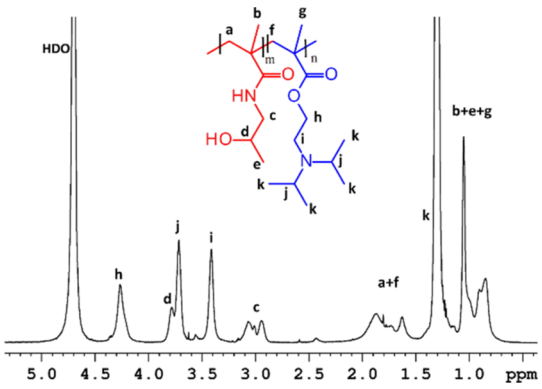

Figure 2. ^{1}H NMR spectrum of PHPMA$_{35}$-*b*-PDPA$_{75}$ diblock copolymer obtained in D_2O/DCl (pH ≈ 2).

The summary of data reported in Table 1 highlights the production of block copolymers with narrowly distributed molecular weights ($M_w/M_n \leq 1.25$) ranging from 10.6 to 21.0 kDa and PDPA content enabling the production of thermodynamically stable polymersomes.

Microfluidic-Assisted Engineering of pH-Responsive Polymersomes. The microfluidic-assisted approach was employed to precisely control the size, morphology, and polydispersity of the self-assembled nanostructures. The experimental procedures were conducted by using microfluidic chips with a micromixing design (Figure 3A,B) for the manufacturing of DOX-free and DOX-loaded polymersomes. The first step regarded the optimization of an organic solvent mixture to properly dissolve the diblock copolymers. We have selected THF/MeOH 80/20 v/v as the organic phase and PBS (pH 7.4) as the aqueous phase. The self-assembly of PHPMA$_{35}$-*b*-PDPA$_{26}$ (f ≈ 53%) resulted in small particles

DOI: 10.1021/acs.langmuir.9b01009
Langmuir 2019, 35, 8363−8372

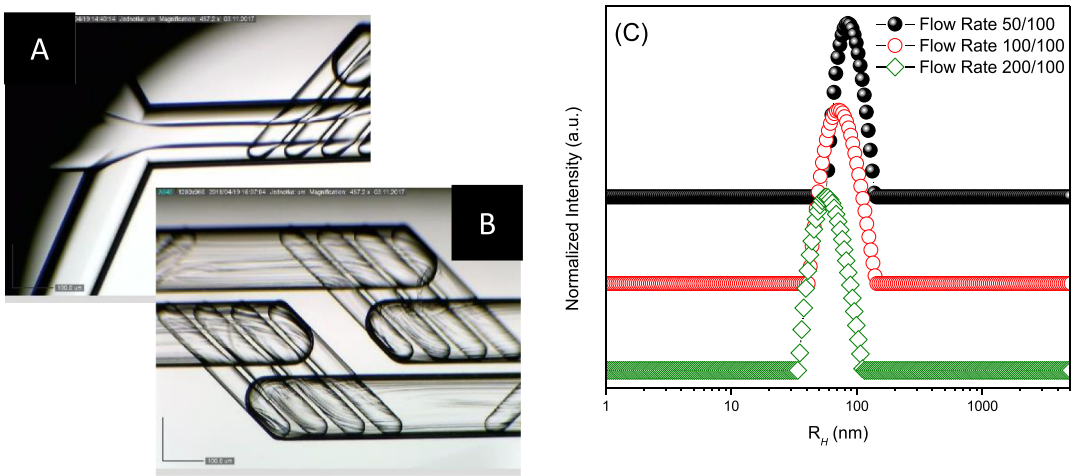

Figure 3. Optical microscopy image of the microfluidic chip depicting the micromixer input orifice where mixing occurs in (A) focused stream and in (B) mixing chambers. Distributions of R_H for $PHPMA_{35}$-*b*-$PDPA_{75}$ polymersomes produced using different flow rates (aqueous phase/organic phase) in μL min^{-1} (C).

(Figure S4) and the average size (R_H = 15.3 nm) is not compatible with polymer vesicles. Indeed, because of the high amount of PHPMA in the copolymer chains, core−shell nanoparticles were presumably obtained (micelles). On the other hand, polymer vesicles were predominantly produced from $PHPMA_{35}$-*b*-$PDPA_{43}$ ($f \approx 35\%$) and $PHPMA_{35}$-*b*-$PDPA_{75}$ ($f \approx 24\%$) as confirmed by TEM images (Figures 4 and S4, respectively) in agreement with the related literature.[38,39] Additionally, the values of the structure-sensitive parameter $\rho = R_G/R_H \approx 1$ and the very low numbers for particle density (Table 2) are robust experimental evidence of the presence of hollow spheres (polymersomes). Indeed, the presence of small particles in addition to the vesicles was observed for self-assembled structures made by $PHPMA_{35}$-*b*-$PDPA_{43}$, and therefore, we have decided to use the block copolymer $PHPMA_{35}$-*b*-$PDPA_{75}$ for further investigations regarding the influence of flow rates on the final properties of the assemblies. The flow rate of the aqueous phase was a variable parameter (50, 100, and 200 μL min^{-1}) while keeping the flow rate of the organic phase constant (100 μL min^{-1}). The results are reported in Figure 3 and Table 2.

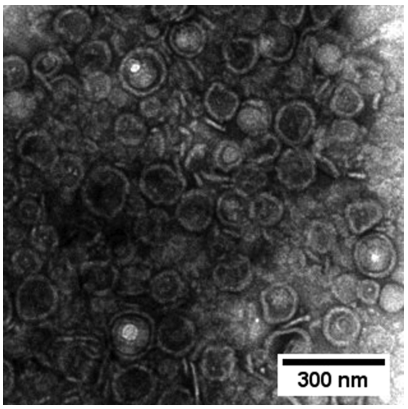

Figure 4. TEM image of $PHPMA_{35}$-*b*-$PDPA_{75}$ polymersomes engineered by microfluidics at aqueous/organic phase flow rates 200/100. (Negatively stained with uranyl acetate, see Supporting Information.)

The precise control over the mechanical parameters of the microfluidic device enabled the manufacturing of highly reproducible polymersomes over different batches. The data displayed in Table 2 demonstrate a reduction in size as the consequence of increasing the flow rate. This is explained by the reduction in mixing time between the phases, thereby leading to faster aggregation kinetics and smaller particles.[21] Taking into account that the assembly process into polymersomes is based on nucleation and aggregation, which takes place at the periphery of the focused stream, the increase in the flow rate of the water streams led to the reduction of the width of the focused polymer solution stream, resulting in a decrease of the length of diffusion between the polymer solution and water. Thus, as the width of the focused stream is reduced by the increase of the water flow rate, faster mixing between the phases and faster nucleation and aggregation take place, leading to production of smaller polymersomes nanoparticles. The TEM image of $PHPMA_{35}$-*b*-$PDPA_{75}$ polymersomes produced using the flow rates of 200 and 100 μL min^{-1} (for water and organic phases, respectively) is portrayed in Figure 4 and demonstrates the engineering of quasi-monodisperse vesicles.

The values of the structure-sensitive parameter ($\rho = R_G/R_H$) ranging from 0.94 to 1.08 also suggest the prevalence of highly hydrated objects compatible to hollow spheres (vesicles). The values of R_G were determined using the SLS data given in Figure S5. The values of aggregation number ($N_{agg} = M_w$ of polymersomes obtained by SLS/M_w of block copolymers

Table 2. Physicochemical Characteristics of the $PHPMA_{35}$-*b*-$PDPA_{75}$ Polymersomes Produced by Microfluidics

flow rate (WP/OP)	R_H (nm)	R_G (nm)	$\rho = R_G/R_H$	PDI	$M_{w(PSomes)}$ (10^7 g mol^{-1})	d (g mL^{-1})	N_{agg}	ζ (mV)
50/100	89.6	84.1	0.94	0.05	3.89	0.02	1850	−4.1
100/100	75.5	80.5	1.06	0.06	2.07	0.02	948	−3.5
200/100	56.9	61.7	1.08	0.06	1.64	0.04	779	−3.8

DOI: 10.1021/acs.langmuir.9b01009
Langmuir 2019, 35, 8363−8372

obtained by SEC) are higher for larger polymersomes. Nevertheless, numbers ranging from ∼800 to 2000 are expected for self-assembled structures larger than $2R_H = D_H \approx 100$ nm.[40] The ζ-potential of the manufactured polymersomes is small and slightly negative, which is indeed desired because higher positive or negative values are normally linked to fast blood clearance of colloidal carriers.[41−43]

The most remarkable features of the produced polymersomes are their low polydispersity (PDI < 0.1) and the precise control over size provided by using the microfluidic approach. Indeed, the manufacturing of polydisperse samples, poor control over size, and low drug LC and encapsulation efficiency[20] are the main drawbacks of the common protocols (thin-film rehydration and pH-switch, for instance) used to manufacture polymersomes. This can be evidenced by comparing the results with those reported in Figure S6 which portrays the distributions of size and TEM image for $PHPMA_{35}$-*b*-$PDPA_{75}$ polymersomes produced by thin-film rehydration and pH-switch. The final structures are bigger ($R_H \approx 100$ nm), polydisperse (PDI > 0.2), and the manufacturing is time consuming. Therefore, the importance of the current data relies primarily on the actual possibility of preparing highly uniform nanoparticles because such particles commonly exhibit more consistent biodistribution and cellular uptake.[44] Accordingly, this result represents an important contribution to progresses in the field. Additionally, the possibility of finely tuning the particle size via changes in the mechanical variables of the microfluidic protocol is particularly relevant because the solid tumor porosity largely depends on tumor location. Indeed, 600 nm-sized particles can still be accumulated to greater extents in hypervascular tumors (such as those located in the lungs), although only much smaller particles (∼30 nm) are able to penetrate poorly permeable tumors (such as those located in the prostate and pancreas). Hence, our system presents a very advantageous property in the possibility of tuning by microfluidics the size of drug-loaded polymersomes to promote enhanced vascular permeability and retention according to the characteristics of the site of action (particularly, the porosity and degree of vascularity of the targeted tumor).

pH-Responsive Behavior of the Polymersomes. The pH-dependent assembly−disassembly behavior of the environmentally responsive nanostructures has been evaluated using ELS and FRET measurements. The values of ζ-potential and light scattering intensity versus pH are given in Figure 5 for $PHPMA_{35}$-*b*-$PDPA_{75}$.

The presence of PHPMA in the polymer chain does not alter remarkably the pK_a of the pH-responsive block (PDPA) because the hydrophilic-to-hydrophobic transition evidenced in the pH range 6.5−6.8 is compatible to values found in the literature for a variety of PDPA-containing materials.[13,45−47] Therefore, the block copolymer behaves as protonated single dissolved polymer chains at pH < 6.5 (positive ζ-potentials were registered), whereas self-assembled nanostructures are present at pH > 6.8. As the light scattering intensity is proportional to the mass of the scattering object, the disassembly of the vesicles at acidic pH is accompanied by a remarkable reduction in the light scattered by the polymer system.

Additionally, FRET measurements have been used to complement the assembly−disassembly investigations. The pair dyes cyanine 3-DBCO (Cy3-DBCO) and cyanine 5-DBCO (Cy5-DBCO) were covalently bound to the block

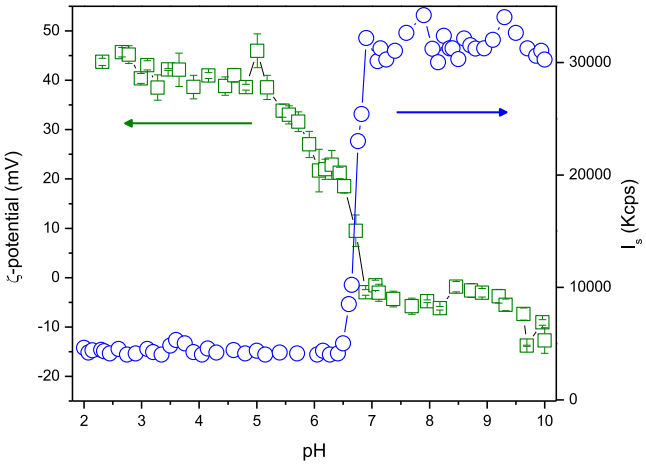

Figure 5. ζ-potential (squares) and overall light scattering intensity (circles) vs pH for $PHPMA_{35}$-*b*-$PDPA_{75}$ in aqueous solution (c = 1.0 mg mL^{-1}).

copolymer via copper-free click chemistry and the polymersomes were produced by microfluidics using a mixture 80:10:10 m/m/m of $PHPMA_{35}$-*b*-$PDPA_{75}$, Cy3-$PHPMA_{35}$-*b*-$PDPA_{75}$, and Cy5-$PHPMA_{35}$-*b*-$PDPA_{75}$. The coupling and formation of dual-fluorescent Cy3−Cy5-polymersomes was evaluated by fluorescence lifetime correlation spectroscopy measurements (Figure S7). The determined values of diffusion time (τ_D = 3.69 ms for Cy3-channel and τ_D = 3.53 ms for Cy5-channel) are very similar, suggesting that both dyes were successfully conjugated to the block copolymer chains, thereby making part of the self-assembled structure. The FRET principle considers the nonradiative energy transfer between a fluorescent donor (Cy3) and an acceptor (Cy5) and it has been applied to evaluate the assembly−disassembly behavior of the manufactured polymersomes at different pH environments: 7.4 (mimicking the bloodstream), pH 5.5 (mimicking intracellular pH of cancer cells), and pH < 3.0 (extreme condition). The FRET efficiency is mathematically described by eq 3, where R_0 is the Förster distance between donor and acceptor at which the FRET efficiency is 50% and R is the donor-to-acceptor separation distance. The FRET efficiency can also be determined using eq 4, where τ_{DA} and τ_D are the fluorescence lifetime of the donor in the presence and in the absence of an acceptor, respectively.[48]

$$E = \frac{{R_0}^6}{{R_0}^6 - R^6} \tag{3}$$

$$E = 1 - \frac{\tau_{DA}}{\tau_D} \tag{4}$$

Eq 4 was used to calculate the FRET efficiency and obtain the FRET efficiency distributions reported in Figure 6. The value for Cy3−Cy5-polymersomes at pH 7.4 was determined as $E = 53.5 \pm 0.2$ and it increases to 80.0 ± 0.1 and 80.2 ± 0.1 when the assemblies were exposed to pH 5.5 and 3.0, respectively. These values certainly reflect variations between pH 7.4 and the acidic pH (pH 5.5 and 3.0) in the structure of the polymersomes mediated by environmental conditions. The protonation of PDPA takes place at pH < $pK_a \approx 6.8$, which increases the FRET efficiency. The unavoidable disassembly of the structures modifies both τ_{DA} and τ_D values in eq 4. Possibly, the pH-induced disassembly and consequently the

DOI: 10.1021/acs.langmuir.9b01009
Langmuir 2019, 35, 8363−8372

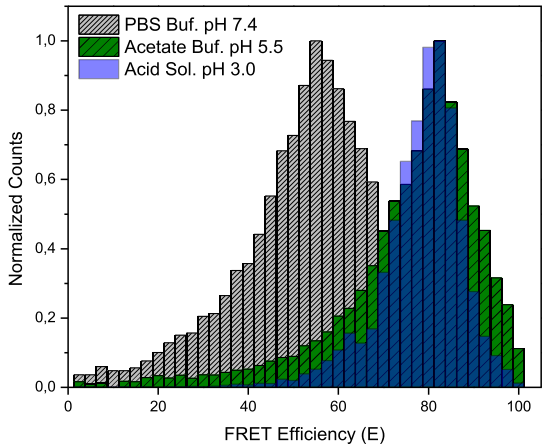

Figure 6. FRET efficiency histograms of Cy3−Cy5-polymersomes incubated in PBS pH 7.4 (gray bars), acetate buffer pH 5.5 (green bars), and acid solution pH ≈ 3.0 (blue bars, adjusted with HCl 1 mol L^{-1}).

presence of free chains lead to the reorganization of the dyes in order to avoid as much as possible the contact with the polar solvent. Cyanine 3-DBCO and cyanine 5-DBCO are highly hydrophobic and therefore the presence of both dyes in a self-organized nonpolar environment within each free-block copolymer chain reduce considerably the inter dye distance, thus increasing the FRET efficiency.

Accordingly, the pH-dependent behavior of the synthesized monodisperse $PHPMA_{35}$-*b*-$PDPA_{75}$ polymersomes can be exploited for the delivery of therapeutic agents into specific sites of action (for instance, the slightly acidic microenvironment of tumor sites).[1,6]

In Vitro Evaluations of DOX-Loaded Monodisperse Polymersomes. The monodisperse $PHPMA_{35}$-*b*-$PDPA_{75}$ polymersomes were loaded with DOX and in vitro evaluations were further performed. The DOX was dissolved in DMSO and added to the block copolymer organic solutions before the microfluidic-assisted fabrication of the polymer vesicles. This has been defined as the more efficient protocol to increase DOX LC and DOX LE. The remaining (unloaded) DOX was removed by dialysis against PBS using a Float-A-Lyzer with MWCO of 3.5−5 kDa. The LC and LE were determined by HPLC (LE = 53.1%; LC = 9.8%). The DOX encapsulation did not substantially affect the polymersome size (R_H = 56.9 nm—DOX-free and R_H = 52.8 nm—DOX-loaded) or morphology. The DOX release was evaluated in pH 7.4 and 5.5 and the results are given in Figure 7.

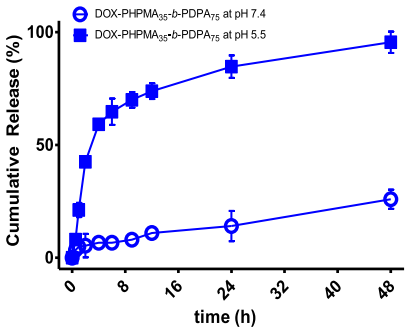

Figure 7. DOX cumulative release from DOX-$PHPMA_{35}$-*b*-$PDPA_{75}$ polymersomes at pH 7.4 (open circles) and pH 5.5 (filled squares).

The data reported in Figure 7 evidence that more than 50% of loaded DOX is released after 4 h at pH 5.5. The values are 80 and 90% after 24 and 48 h, respectively. On the other hand, 11 and 14% of the therapeutic agent are released within 12 and 24 h at pH = 7.4, respectively. Indeed, the cumulative release after 48 h reaches only 25% in such environment. These results suggest that the pH-responsive polymersomes at pH > pK_a are stable and able to carry the anticancer drug in the bloodstream without pronounced drug leakage. Conversely, at pH < pK_a, the polymersomes are triggered and the vesicles are physically disassembled, thereby quickly releasing the loaded active agent.

Subsequently, the cellular uptake and cytotoxicity of the DOX-loaded polymersomes were evaluated. The self-assemblies are stable in the cell culture medium without experimental evidence of aggregation over the time scale probed—24 h (Figure S8—Supporting Information). The cellular uptake experiments were performed by flow cytometry using breast (4T1) and melanoma (B16F10) cancer cell lines. The DOX-loaded polymersomes and free DOX were added to the cells at equivalent concentrations. The mean fluorescence intensity (resulting from DOX uptake) was measured and the quantitative data are portrayed in Figure 8A,B.

The reported results provide evidence that free DOX is uptaken in higher amounts than DOX loaded into polymersomes. Indeed, free DOX can freely diffuse throughout the cell membrane,[14] whereas entrapped DOX can only be uptaken by endocytosis. This might, at least to some extent, explain the results reported in Figure 8 (top). In the next step, the in vitro therapeutic effects of free DOX (control) and DOX-$PHPMA_{35}$-*b*-$PDPA_{75}$ polymersomes were evaluated by using the alamarBlue assay. The assemblies were incubated with cells for 24 h and the results are portrayed in Figure 8C,D. The DOX-free (unloaded) polymersomes are not toxic to B16F10 and 4T1 cells (Figure S9—Supporting Information file), whereas DOX-loaded $PHPMA_{35}$-*b*-$PDPA_{75}$ polymersomes are evidenced to be cytotoxic to both cell lines. The IC_{50} value for free DOX and DOX-$PHPMA_{35}$-*b*-$PDPA_{75}$ polymersomes are ∼0.234 and ∼0.075 μg mL^{-1}, respectively, for 4T1 cells (measured after 24 h of incubation time), whereas inversed values were determined for B16F10 cells (∼0.186 and ∼0.367 μg mL^{-1} for free DOX and DOX-$PHPMA_{35}$-*b*-$PDPA_{75}$ polymersomes, respectively). This is supposed to be associated with particular features and metabolic differences among the cell lines. Nevertheless, the reported cytotoxicity of free DOX and DOX-$PHPMA_{35}$-*b*-$PDPA_{75}$ polymersomes is similar at higher concentrations, pointing out the effectiveness of the formulation against the investigated cancer cell lines. Therefore, although free DOX is uptaken to higher extent, the biological activity is similar to that of DOX loaded into polymersomes, suggesting that nonencapsulated DOX is more susceptible to intracellular degradation, thus justifying the similar levels of cell viability.

■ CONCLUSIONS

We demonstrate the use of microfluidic technology to engineer quasi-monodisperse pH-responsive polymersomes. The protocol also enables DOX encapsulation into the aqueous milieu of the hollow spheres. The microfluidic manufacturing allowed the control over the whole manufacturing process leading to monodisperse (PDI < 0.10) polymersomes with desired size (R_H ≈ 50 nm) for cellular uptake via endocytosis. This is particularly important toward homogeneous biodistribution and cellular uptake. Additionally, the vesicle size can be finely

DOI: 10.1021/acs.langmuir.9b01009
Langmuir 2019, 35, 8363−8372

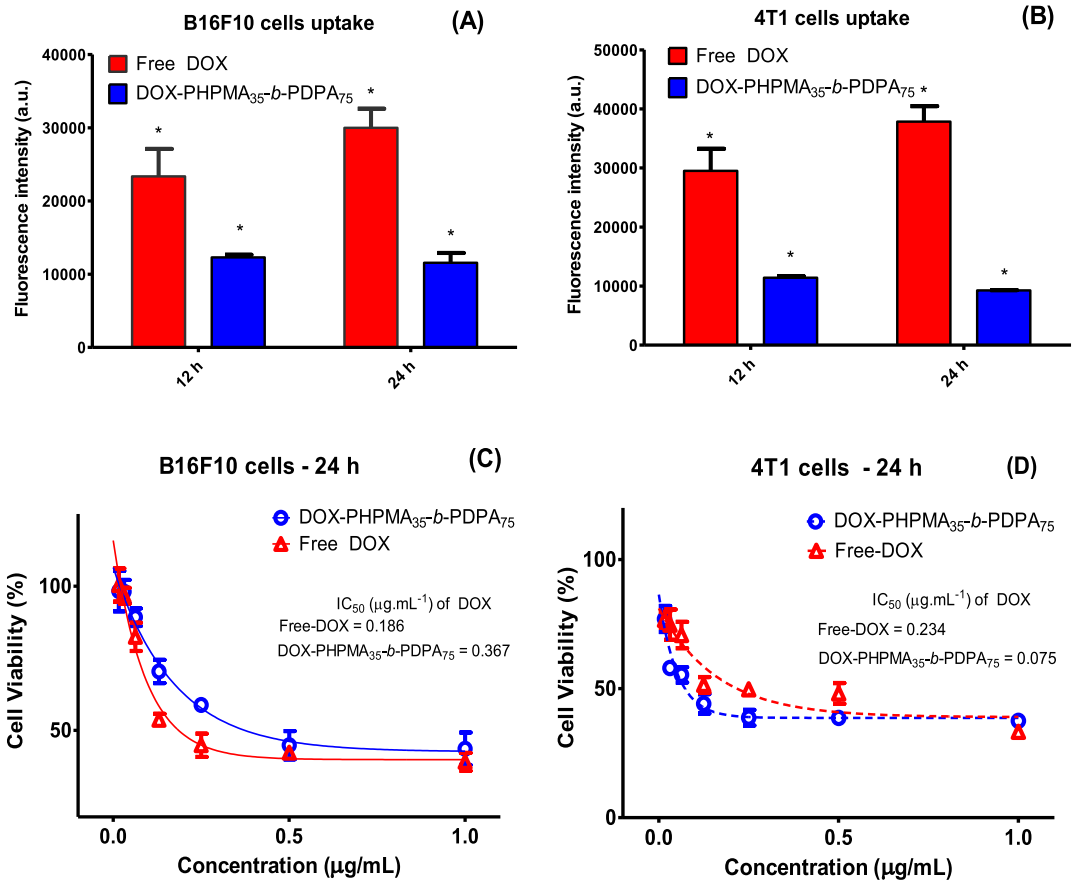

Figure 8. Quantitative flow cytometry data for free DOX and DOX-PHPMA$_{35}$-*b*-PDPA$_{75}$ polymersomes uptaken by B16F10 (A) and 4T1 (B) cancer cells (the mean fluorescence intensities were collected per 10 000 events and the results are expressed as mean ± SD—n = 3) and cellular viability performed in B16F10 (C) and 4T1 (D) cells after 24 h incubation time as a function of free-DOX concentration or DOX equivalent concentration loaded into DOX-PHPMA$_{35}$-*b*-PDPA$_{75}$ polymersomes. *p < 0.05 vs free-DOX.

tuned by playing with the mechanical parameters inherent to the process, particularly the organic and/or aqueous flow rates. We understand these findings as of due relevance within the framework of nanoparticle-based cancer therapies because the leaky vasculature is distinct from tumor to tumor and therefore the size of nanocarriers influences vascular permeability. The possibility of scale-up production of nanoparticles with precisely tuned size may enhance the efficacy of therapies because the assemblies can be engineered bearing in mind tumor location and characteristics (particularly, the porosity). Furthermore, the pH-responsive drug-loaded polymersomes demonstrated sufficient levels of cellular uptake, and they are cytotoxic to tumor cells (B16F10 and 4T1) at similar levels compared to free administrated DOX. These features encourage the use of such assemblies as a potential platform to target damaged cells while preserving healthy environments during systemic circulation.

■ ASSOCIATED CONTENT

Supporting Information

The Supporting Information is available free of charge on the ACS Publications website at DOI: 10.1021/acs.langmuir.9b01009.

Methods, preparation of polymersomes, FTIR spectra, ^{1}H NMR spectrum, SEC traces, TEM images, static light scattering data, distributions of R_H, and fluorescence correlation spectroscopy data (PDF)

■ AUTHOR INFORMATION

Corresponding Authors

*E-mail: lindomar.albuquerque@ufabc.edu.br (L.J.C.A.).
*E-mail: jager@imc.cas.cz (E.J.).

ORCID

Lindomar J. C. Albuquerque: 0000-0003-1443-1795
Alessandro Jäger: 0000-0001-6171-4718
Petr Štěpánek: 0000-0003-1433-678X
Fernando C. Giacomelli: 0000-0002-6872-9354
Eliézer Jäger: 0000-0001-9939-2355

Notes

The authors declare no competing financial interest.

■ ACKNOWLEDGMENTS

This work has been sponsored by the Czech Science Foundation (grant no. 17-09998S), FAPESP (grant no. 2017/00459-4) and by the Czech Ministry of Education, Youth and Sports (grant no. 7AMB18FR038). L.J.C.A. acknowledges financial support from FAPESP (grant no. 2017/11261-0). A.J. acknowledges financial support from Czech Academy of Sciences (Grant MSM200501606). Electron microscopy at the Institute of Macromolecular Chemistry was supported by TA CR (project TN01000008).

DOI: 10.1021/acs.langmuir.9b01009
Langmuir 2019, 35, 8363−8372

REFERENCES

(1) Shi, J.; Kantoff, P. W.; Wooster, R.; Farokhzad, O. C. Cancer Nanomedicine: Progress, Challenges and Opportunities. *Nat. Rev. Cancer* **2017**, *17*, 20−37.

(2) Chen, H.; Zhang, W.; Zhu, G.; Xie, J.; Chen, X. Rethinking Cancer Nanotheranostics. *Nat. Rev. Mater.* **2017**, *2*, 17024.

(3) Maeda, H.; Wu, J.; Sawa, T.; Matsumura, Y.; Hori, K. Tumor Vascular Permeability and the EPR Effect in Macromolecular Therapeutics: A Review. *J. Controlled Release* **2000**, *65*, 271−284.

(4) Maeda, H.; Noguchi, Y.; Sato, K.; Akaike, T. Enhanced Vascular Permeability in Solid Tumor Is Mediated by Nitric Oxide and Inhibited by Both New Nitric Oxide Scavenger and Nitric Oxide Synthase Inhibitor. *Jpn. J. Cancer Res.* **1994**, *85*, 331−334.

(5) Fang, J.; Nakamura, H.; Maeda, H. The EPR Effect: Unique Features of Tumor Blood Vessels for Drug Delivery, Factors Involved, and Limitations and Augmentation of the Effect. *Adv. Drug Delivery Rev.* **2011**, *63*, 136−151.

(6) Corbet, C.; Feron, O. Tumour Acidosis: From the Passenger to the Driver's Seat. *Nat. Rev. Cancer* **2017**, *17*, 577−593.

(7) Funhoff, A. M.; van Nostrum, C. F.; Koning, G. a.; Schuurmans-Nieuwenbroek, N. M. E.; Crommelin, D. J. A.; Hennink, W. E. Endosomal Escape of Polymeric Gene Delivery Complexes Is Not Always Enhanced by Polymers Buffering at Low PH. *Biomacromolecules* **2004**, *5*, 32−39.

(8) Zha, Z.; Li, J.; Ge, Z. Endosomal-Escape Polymers Based on Multicomponent Reaction-Synthesized Monomers Integrating Alkyl and Imidazolyl Moieties for Efficient Gene Delivery. *ACS Macro Lett.* **2015**, *4*, 1123−1127.

(9) Du, A. W.; Stenzel, M. H. Drug Carriers for the Delivery of Therapeutic Peptides. *Biomacromolecules* **2014**, *15*, 1097−1114.

(10) Pang, Z.; Lu, W.; Gao, H.; Hu, K.; Chen, J.; Zhang, C.; Gao, X.; Jiang, X.; Zhu, C. Preparation and Brain Delivery Property of Biodegradable Polymersomes Conjugated with OX26. *J. Controlled Release* **2008**, *128*, 120−127.

(11) Scarpa, E.; Bailey, J. L.; Janeczek, A. A.; Stumpf, P. S.; Johnston, A. H.; Oreffo, R. O. C.; Woo, Y. L.; Cheong, Y. C.; Evans, N. D.; Newman, T. A. Quantification of Intracellular Payload Release from Polymersome Nanoparticles. *Sci. Rep.* **2016**, *6*, 29460.

(12) Hearnden, V.; Lomas, H.; MacNeil, S.; Thornhill, M.; Murdoch, C.; Lewis, A.; Madsen, J.; Blanazs, A.; Armes, S.; Battaglia, G. Diffusion Studies of Nanometer Polymersomes across Tissue Engineered Human Oral Mucosa. *Pharm. Res.* **2009**, *26*, 1718−1728.

(13) Lomas, H.; Du, J.; Canton, I.; Madsen, J.; Warren, N.; Armes, S. P.; Lewis, A. L.; Battaglia, G. Efficient Encapsulation of Plasmid DNA in PH-Sensitive PMPC-PDPA Polymersomes: Study of the Effect of PDPA Block Length on Copolymer-DNA Binding Affinity. *Macromol. Biosci.* **2010**, *10*, 513−530.

(14) Pegoraro, C.; Cecchin, D.; Gracia, L. S.; Warren, N.; Madsen, J.; Armes, S. P.; Lewis, A.; MacNeil, S.; Battaglia, G. Enhanced Drug Delivery to Melanoma Cells Using PMPC-PDPA Polymersomes. *Cancer Lett.* **2013**, *334*, 328−337.

(15) Lee, J. C.-M.; Bermudez, H.; Discher, B. M.; Sheehan, M. A.; Won, Y.-Y.; Bates, F. S.; Discher, D. E. Preparation, Stability, and in Vitro Performance of Vesicles Made with Diblock Copolymers. *Biotechnol. Bioeng.* **2001**, *73*, 135−145.

(16) Greene, A. C.; Henderson, I. M.; Bachand, G. D.; Paxton, W. F.; VanDelinder, V.; Gomez, A. The Role of Membrane Fluidization in the Gel-Assisted Formation of Giant Polymersomes. *PLoS One* **2016**, *11*, No. e0158729.

(17) Pautot, S.; Frisken, B. J.; Weitz, D. A. Production of Unilamellar Vesicles Using an Inverted Emulsion. *Langmuir* **2003**, *19*, 2870−2879.

(18) Allen, S.; Osorio, O.; Liu, Y.-G.; Scott, E. Facile Assembly and Loading of Theranostic Polymersomes via Multi-Impingement Flash Nanoprecipitation. *J. Controlled Release* **2017**, *262*, 91−103.

(19) Wang, L.; Chierico, L.; Little, D.; Patikarnmonthon, N.; Yang, Z.; Azzouz, M.; Madsen, J.; Armes, S. P.; Battaglia, G. Encapsulation of Biomacromolecules within Polymersomes by Electroporation. *Angew. Chem., Int. Ed.* **2012**, *51*, 11122−11125.

(20) Brown, L.; McArthur, S. L.; Wright, P. C.; Lewis, A.; Battaglia, G. Polymersome Production on a Microfluidic Platform Using PH Sensitive Block Copolymers. *Lab Chip* **2010**, *10*, 1922−1928.

(21) Sanson, C.; Schatz, C.; Le Meins, J.-F.; Brûlet, A.; Soum, A.; Lecommandoux, S. Biocompatible and Biodegradable Poly-(trimethylene carbonate)-b-Poly(l-glutamic acid) Polymersomes: Size Control and Stability. *Langmuir* **2010**, *26*, 2751−2760.

(22) Sanson, C.; Schatz, C.; Le Meins, J.-F.; Soum, A.; Thévenot, J.; Garanger, E.; Lecommandoux, S. A Simple Method to Achieve High Doxorubicin Loading in Biodegradable Polymersomes. *J. Controlled Release* **2010**, *147*, 428−435.

(23) Yildiz, M. E.; Prud'homme, R. K.; Robb, I.; Adamson, D. H. Formation and Characterization of Polymersomes Made by a Solvent Injection Method. *Polym. Adv. Technol.* **2007**, *18*, 427−432.

(24) Xu, J.; Zhang, S.; MacHado, A.; Lecommandoux, S.; Sandre, O.; Gu, F.; Colin, A. Controllable Microfluidic Production of Drug-Loaded PLGA Nanoparticles Using Partially Water-Miscible Mixed Solvent Microdroplets as a Precursor. *Sci. Rep.* **2017**, *7*, 4794.

(25) Habault, D.; Dery, A.; Leng, J.; Lecommandoux, S.; Le Meins, J.-F.; Sandre, O. Droplet Microfluidics to Prepare Magnetic Polymer Vesicles and to Confine the Heat in Magnetic Hyperthermia. *IEEE Trans. Magn.* **2013**, *49*, 182−190.

(26) Lomas, H.; Armes, S. P.; Battaglia, G.; Canton, I.; MacNeil, S.; Ryan, A. J.; Du, J.; Lewis, A. L. Biomimetic PH Sensitive Polymersomes for Efficient DNA Encapsulation and Delivery. *Adv. Mater.* **2007**, *19*, 4238−4243.

(27) Canton, I.; Battaglia, G. Endocytosis at the Nanoscale. *Chem. Soc. Rev.* **2012**, *41*, 2718.

(28) Jäger, E.; Jäger, A.; Etrych, T.; Giacomelli, F. C.; Chytil, P.; Jigounov, A.; Putaux, J.-L.; Říhová, B.; Ulbrich, K.; Štěpánek, P. Self-Assembly of Biodegradable Copolyester and Reactive HPMA-Based Polymers into Nanoparticles as an Alternative Stealth Drug Delivery System. *Soft Matter* **2012**, *8*, 9563.

(29) Yang, J.; Kopeček, J. The Light at the End of the Tunnel—Second Generation HPMA Conjugates for Cancer Treatment. *Curr. Opin. Colloid Interface Sci.* **2017**, *31*, 30−42.

(30) Mendonça, P. V.; Serra, A. C.; Popov, A. V.; Guliashvili, T.; Coelho, J. F. J. Efficient RAFT Polymerization of N-(3-Aminopropyl)Methacrylamide Hydrochloride Using Unprotected "Clickable" Chain Transfer Agents. *React. Funct. Polym.* **2014**, *81*, 1−7.

(31) Jäger, E.; Jäger, A.; Chytil, P.; Etrych, T.; Říhová, B.; Giacomelli, F. C.; Štěpánek, P.; Ulbrich, K. Combination Chemotherapy Using Core-Shell Nanoparticles through the Self-Assembly of HPMA-Based Copolymers and Degradable Polyester. *J. Controlled Release* **2013**, *165*, 153−161.

(32) Paget, V.; Dekali, S.; Kortulewski, T.; Grall, R.; Gamez, C.; Blazy, K.; Aguerre-Chariol, O.; Chevillard, S.; Braun, A.; Rat, P.; et al. Specific Uptake and Genotoxicity Induced by Polystyrene Nanobeads with Distinct Surface Chemistry on Human Lung Epithelial Cells and Macrophages. *PLoS One* **2015**, *10*, No. e0123297.

(33) Li, G.; Zheng, H.; Bai, R. A Facile Strategy for the Preparation of Azide Polymers via Room Temperature RAFT Polymerization by Redox Initiation. *Macromol. Rapid Commun.* **2009**, *30*, 442−447.

(34) Ladmiral, V.; Legge, T. M.; Zhao, Y.; Perrier, S. "Click" Chemistry and Radical Polymerization: Potential Loss of Orthogonality. *Macromolecules* **2008**, *41*, 6728−6732.

(35) Höbel, S.; Loos, A.; Appelhans, D.; Schwarz, S.; Seidel, J.; Voit, B.; Aigner, A. Chapter 2. Heat of Polymerization. *J. Macromol. Sci., Part C: Polym. Rev.* **1969**, *3*, 339−356.

(36) Quémener, D.; Davis, T. P.; Barner-kowollik, C.; Stenzel, M. H. RAFT and click chemistry: A versatile approach to well-defined block copolymers. *Chem. Commun.* **2006**, 5051−5053.

(37) Moad, G.; Rizzardo, E.; Thang, S. H. Radical Addition-Fragmentation Chemistry in Polymer Synthesis. *Polymer* **2008**, *49*, 1079−1131.

(38) Guan, L.; Rizzello, L.; Battaglia, G. Polymersomes and Their Applications in Cancer Delivery and Therapy. *Nanomedicine* **2015**, *10*, 2757−2780.

DOI: 10.1021/acs.langmuir.9b01009
Langmuir 2019, 35, 8363−8372

(39) Discher, D. E.; Eisenberg, A. Polymer Vesicles. *Science* **2002**, *297*, 967−973.
(40) de Castro, C. E.; Mattei, B.; Riske, K. A.; Jäger, E.; Jäger, A.; Stepánek, P.; Giacomelli, F. C. Understanding the Structural Parameters of Biocompatible Nanoparticles Dictating Protein Fouling. *Langmuir* **2014**, *30*, 9770−9779.
(41) Johnston, A. H.; Dalton, P. D.; Newman, T. A. Polymersomes, Smaller than You Think: Ferrocene as a TEM Probe to Determine Core Structure. *J. Nanopart. Res.* **2010**, *12*, 1997−2001.
(42) Wang, G.; de Kruijff, R. M.; Abou, D.; Ramos, N.; Mendes, E.; Franken, L. E.; Wolterbeek, H. T.; Denkova, A. G. Pharmacokinetics of Polymersomes Composed of Poly(Butadiene-Ethylene Oxide); Healthy versus Tumor-Bearing Mice. *J. Biomed. Nanotechnol.* **2016**, *12*, 320−328.
(43) Lee, J. S.; Ankone, M.; Pieters, E.; Schiffelers, R. M.; Hennink, W. E.; Feijen, J. Circulation Kinetics and Biodistribution of Dual-Labeled Polymersomes with Modulated Surface Charge in Tumor-Bearing Mice: Comparison with Stealth Liposomes. *J. Controlled Release* **2011**, *155*, 282−288.
(44) Xie, H.; Smith, J. W. Fabrication of PLGA Nanoparticles with a Fluidic Nanoprecipitation System. *J. Nanobiotechnol.* **2010**, *8*, 18.
(45) Jäger, A.; Jäger, E.; Surman, F.; Höcherl, A.; Angelov, B.; Ulbrich, K.; Drechsler, M.; Garamus, V. M.; Rodriguez-Emmenegger, C.; Nallet, F.; et al. Nanoparticles of the Poly([*N*-(2-Hydroxypropyl)]Methacrylamide)-*b*-Poly[2-(Diisopropylamino)-Ethyl Methacrylate] Diblock Copolymer for PH-Triggered Release of Paclitaxel. *Polym. Chem.* **2015**, *6*, 4946−4954.
(46) Giacomelli, F. C.; Stepánek, P.; Giacomelli, C.; Schmidt, V.; Jäger, E.; Jäger, A.; Ulbrich, K. PH-Triggered Block Copolymer Micelles Based on a PH-Responsive PDPA (Poly[2-(Diisopropylamino)Ethyl Methacrylate]) Inner Core and a PEO (Poly(Ethylene Oxide)) Outer Shell as a Potential Tool for the Cancer Therapy. *Soft Matter* **2011**, *7*, 9316−9325.
(47) Pearson, R. T.; Warren, N. J.; Lewis, A. L.; Armes, S. P.; Battaglia, G. Effect of pH and Temperature on PMPC−PDPA Copolymer Self-Assembly. *Macromolecules* **2013**, *46*, 1400−1407.
(48) Chung, H. S.; Gopich, I. V. Fast Single-Molecule FRET Spectroscopy: Theory and Experiment. *Phys. Chem. Chem. Phys.* **2014**, *16*, 18644−18657.

DOI: 10.1021/acs.langmuir.9b01009
Langmuir 2019, 35, 8363−8372

Journal of Controlled Release 332 (2021) 529–538

Contents lists available at ScienceDirect

Journal of Controlled Release

journal homepage: www.elsevier.com/locate/jconrel

pH-responsive polymersome-mediated delivery of doxorubicin into tumor sites enhances the therapeutic efficacy and reduces cardiotoxic effects

Lindomar J.C. Albuquerque [a,b,*], Vladimir Sincari [a], Alessandro Jäger [a], Jan Kucka [a], Jana Humajova [c], Jan Pankrac [d], Petr Paral [d], Tomas Heizer [d], Olga Janouškova [a], Irina Davidovich [e], Yeshayahu Talmon [e], Pavla Pouckova [c], Petr Štěpánek [a], Ludek Sefc [d], Martin Hruby [a], Fernando C. Giacomelli [b], Eliézer Jäger [a,*]

[a] Institute of Macromolecular Chemistry, Academy of Sciences of the Czech Republic, Heyrovského nám. 2, 162 06 Prague 6, Czech Republic
[b] Centro de Ciências Naturais e Humanas, Universidade Federal do ABC, Avenida dos Estados 5001, Santo André 09210-580, Brazil
[c] Institute of Biophysics and Informatics, First Faculty of Medicine, Charles University, Salmovska, 1, 120 00 Prague, Czech Republic
[d] Center for Advanced Preclinical Imaging (CAPI), First Faculty of Medicine, Charles University, Salmovská 3, Prague 2, 120 00, Czech Republic
[e] Department of Chemical Engineering and the Russell Berrie Nanotechnology Institute (RBNI), Technion-Israel Institute of Technology, Haifa 3200003, Israel

ARTICLE INFO

Keywords:
Nanomedicine
pH-responsive polymersomes
Doxorubicin
Antitumor activity
Cardiotoxicity

ABSTRACT

The delivery of therapeutics into sites of action by using cargo-delivery platforms potentially minimizes their premature degradation and fast clearance from the bloodstream. Additionally, drug-loaded stimuli-responsive supramolecular assemblies can be produced to respond to the inherent features of tumor microenvironments, such as extracellular acidosis. We report in this framework the use of pH-responsive polymersomes (PSs) manufactured using poly([*N*-(2-hydroxypropyl)] methacrylamide)$_{35}$-*b*-poly[2-(diisopropylamino)ethyl methacrylate]$_{75}$ as the building unit (PHPMA$_{35}$-*b*-PDPA$_{75}$). The self-assemblies were produced with desired size towards long circulation time and tumor accumulation (hydrodynamic diameter - $D_H \sim 100$ nm), and they could be successfully loaded with 10% *w/w* DOX (doxorubicin), while maintaining colloidal stability. The DOX loaded amount is presumably mainly burst-released at the acidic microenvironment of tumors thanks to the pH-switchable property of PDPA (pKa ~ 6.8), while reduced drug leakage has been monitored in pH 7.4. Compared to the administration of free DOX, the drug-loaded supramolecular structures greatly enhanced the therapeutic efficacy with effective growth inhibition of EL4 lymphoma tumor model and 100% survival rate in female C57BL/6 black mice over 40 days. The approach also led to reduced cardiotoxic effect. These features highlight the potential application of such nanotechnology-based treatment in a variety of cancer therapies where low local pH is commonly found, and emphasize PHPMA-based nanomedicines as an alternative to PEGylated formulations.

1. Introduction

The most recent survey by the International Agency for Research on Cancer reported that the global mortality related to this malignancy was approximately 9.6 million in 2018 [1] (21% higher than in 2008) [2]. This number is predicted to be as high as 19.3 million by 2025 [3], calling for improvements in cancer therapies [4,5]. In this framework, the recent approaches have embraced the design of nanocarriers that can navigate the body and deliver payloads at desired sites. Indeed, chemotherapy is one of the key treatments to fight cancer, but the development of new strategies to improve the efficacy of chemotherapeutic agents, as well as to reduce side effects, is still challenging. Anthracycline doxorubicin (DOX) is one of the most efficient drugs used in chemotherapeutic treatment of lymphoma, acute myeloid leukemia, and breast cancers [6–8]. Nevertheless, side effects such as short blood circulation time and cardiotoxicity limit its use. Truly, DOX cardiotoxicity is of due relevance, and life-threatening heart problems may last for years after treatment [8–10]. Accordingly, DOX-based nanomedicines are currently considered to overcome such noteworthy drawback.

The most successful DOX-loaded carriers are currently the PEGylated

* Corresponding authors at: Institute of Macromolecular Chemistry, Academy of Sciences of the Czech Republic, Heyrovského nám. 2, 162 06 Prague 6, Czech Republic.

E-mail addresses: lindomar.albuquerque@ufabc.edu.br (L.J.C. Albuquerque), jager@imc.cas.cz (E. Jäger).

https://doi.org/10.1016/j.jconrel.2021.03.013
Received 22 October 2020; Received in revised form 11 February 2021; Accepted 9 March 2021
Available online 12 March 2021
0168-3659/© 2021 Elsevier B.V. All rights reserved.

liposomal formulations Caelyx® and Doxil®. These are approximately 100 nm-sized vesicles with 10,000–15,000 encapsulated DOX molecules [11,12]. They are frequently employed as nanotechnology-based chemotherapeutic agents [13]. Nevertheless, despite 60-fold increase in the fraction of the recovered dose in the blood, 4-fold increase in the recovered dose in the liver-spleen, and 25-fold increase in the recovered dose in tumors, the formulations still compromise the effectiveness of treatments due to a lack of specificity and DOX leakage during blood circulation. These issues result in several side effects including hand-foot syndrome [11,14], mouth pain (stomatitis) [11], low white blood cell count, low platelet count, anemia, pseudoallergy [15,16], nausea and vomiting. Furthermore, another important consideration associated to the administration is the presence of anti-PEG antibodies in the immune system as caused by the reuse of PEG-based drugs and formulations [17–19]. Several reports have highlighted reduced therapeutic effect of PEG-based nanomedicines due the accelerated blood clearance (ABC) phenomenon mediated by the anti-PEG antibodies [19–22]. For instance, it has been demonstrated that PEG-modified liposomes induce an IgM response, which results in pronounced ABC after the second injection. Conversely, this phenomenon has not been observed for liposomes stabilized by other water-soluble polymers, including PHPMA [23,24].

Taking these considerations into account, we aimed to fundamentally contribute in circumventing such drawbacks by designing DOX-loaded, stimuli-responsive polymeric vesicles (polymersomes) capable of responding to the inherent features of tumor microenvironments. This strategy may in principle enhance the therapeutic outcomes, and reduce the side-effects of the widely used DOX. In this regard, recent advances in controlled-living polymerization processes have encouraged the preparation of a wide range of macromolecules with controllable architecture, functionality, composition and topology, thereby allowing the engineering of self-assemblies where membrane thickness, flexibility, size, permeability and responsiveness can be controlled [25–28]. Hence, polymersomes (PSs) can be made responsive to a variety of stimuli, including pH, redox potential, light, magnetic field, temperature and the presence of specific enzymes. In this framework, it is well documented that the extracellular and subcellular compartments in tumor sites are characterized by a slightly acidic pH (ranging from 6.2 to 6.8, depending on the tumor site and tumor aggressiveness), as a consequence of the high metabolic rate of cancer cells, thereby leading to the accumulation of H^+ ions in the tumor microenvironment [29,30]. Therefore, the use of DOX-loaded pH-responsive polymersomes able to transport the cargo while navigating through healthy tissues (pH ~ 7.4), and also able to rapidly release the payload under environmental conditions typically found in tumors (for instance the slightly acid pH), is presumably a suitable strategy to enhance the therapeutic efficacy, while reducing the side effects of DOX. This goal was herein hypothesized by using the hydrophilic-hydrophobic pH-responsive polymer poly (2-(diisopropylamino)ethyl methacrylate (PDPA) at the composition of the building unit of the polymersomes. The PDPA becomes hydrophilic when the pH drops to values lower than its pKa ~ 6.8 [31]. The polymer poly(*N*-(2-hydroxypropyl) methacrylamide (PHPMA) was chosen as the hydrophilic stabilizing segment due to its protein-repelling characteristics, and the possibility of avoiding accelerated blood clearance [23,32,33].

Nevertheless, although the usefulness of pH-responsive polymersomes for such purpose is clear, the preparation of polymeric vesicles by using standard protocols usually leads to relatively polydisperse assemblies with poor control over the average size [34]. Additionally, the presence of multiple morphologies is frequently observed. This issue can be circumvented, for instance, by fabricating the assemblies using a microfluidic technique, as previously demonstrated by us [35]. The control over the mixing conditions enables high reproducibility, narrow size distribution and the tuning of the final size of the self-assemblies [36]. The encapsulation of active agents into size-defined and nearly monodisperse PSs may provide enhanced therapeutic effect due to a more homogenous biodistribution of the therapeutic agent in the target site. The herein produced DOX-loaded pH-responsive vesicles were characterized in detail by light and small-angle X-ray scattering, and directly imaged by cryogenic transmission electron microscopy (cryo-TEM). The effectiveness of the DOX-loaded assemblies was evaluated *in vitro* by assessing the cellular uptake behavior and cell viability, and *in vivo* by assessing the biodistribution of the assemblies and their anti-tumor efficacy in mice bearing EL4 lymphoma model. The experimental data were compared whenever appropriate with the administration of free DOX.

2. Experimental section

2.1. Materials and chemicals

The monomer 2-(diisopropylamino)ethyl methacrylate (DPA, 97%, Sigma Aldrich, Czech Republic) was purified by vacuum distillation prior to use. The initiator 2,2′-azobis(2-methylpropionitrile) (AIBN, Sigma Aldrich, Czech Republic) and the chain-transfer agent, 4-cyano-4-(phenylcarbonothioylthio)pentanoic acid (CTA-COOH, Sigma Aldrich, Czech Republic) were used as received. The solvents methanol (MeOH), dimethyl sulfoxide (DMSO), tert-butanol and 1,4-dioxane (Dioxane), and the chemicals sodium sulfate (Na_2SO_4), magnesium sulfate ($MgSO_4$), sodium azide (NaN_3), 3-chloro-1-propanol, *N*-(3-dimethylaminopropyl)-*N*′-ethylcarbodiimide hydrochloride (EDC, 98%), doxorubicin (DOX) and Human plasma were purchased from Sigma Aldrich (Czech Republic). The fluorescent dye dibenzylcyclooctyne-Cyanine7 (Cy7) was purchased from Jena Bioscience (Germany). Dichloromethane (DCM) and acetone were purchased from Lachner (Czech Republic). All the solvents were dried over molecular sieves (48 h) prior to use.

2.2. Synthesis and characterization of the pH-responsive $PHPMA_{35}$-b-$PDPA_{75}$ block copolymer

The synthesis of the block copolymer $PHPMA_{35}$-*b*-$PDPA_{75}$ was performed by RAFT polymerization, and designed to have appropriate hydrophobic fraction towards the fabrication of polymeric vesicles [35]. Firstly, the azide-terminated PHPMA macro-CTA was synthesized in a Schlenk tube equipped with a magnetic stirrer. The HPMA monomer was dissolved in *tert*-butanol, and the solution was filled with argon for 15 min followed by deoxygenation by three freeze-pump-thaw cycles. CTA-azide and the initiator AIBN were dissolved in a small amount of DMSO, this solution was added to the Schlenk tube, and another freeze-pump-thaw cycle was completed. The tube was filled with argon and placed into an oil bath at 70 °C to start the polymerization reaction (18 h), followed by quenching in liquid nitrogen. The product was then precipitated in a cold mixture of acetone/diethyl ether (3/1), further purified by Sephadex LH-20 in methanol, precipitated in cold diethyl ether, and finally vacuum-dried, resulting in a pink solid. Subsequently, in a Schlenk flask with a magnetic stirrer, the PHPMA macro-CTA azide was dissolved in MeOH (10 mL), DPA monomer was dissolved in dioxane (15 mL), and the initiator AIBN was dissolved in DMSO (100 μL), and they were mixed under stirring. The mixture was filled with argon, followed by three freeze-pump-thaw cycles, and the solution was refilled again with argon for 15 min. The tube was placed into an oil bath at 70 °C for 18 h, and then quenched by exposing to air and liquid nitrogen. The block copolymer was obtained after dialysis against deionized water at pH ~ 3.0 for 48 h. The block copolymer was recovered by lyophilization and characterized by ^{1}H NMR and size exclusion chromatography (SEC). The block copolymer $PHPMA_{35}$-*b*-$PDPA_{75}$ with $M_w = 22{,}000\ g{\cdot}mol^{-1}$ and $Đ = (M_w/M_n) = 1.05$ has its details concerning the synthetic approach and molecular characterization is described elsewhere [31,35,37].

2.3. Synthesis and characterization of the Cy7-PHPMA$_{35}$-b-PDPA$_{75}$ conjugate

The coupling between the fluorescent dye Cyanine 7-DBCO (Cy7) and the azide-terminated block copolymer was performed by dissolving 30 mg of the diblock copolymer in 1 mL of DMF in an amber glass vial under stirring. The fluorescent dye (Cyanine 7-DBCO) was further added to the vial at molar ratio 3:1 (fluorescent dye/azide terminated group), and the reaction was carried out overnight in the dark. Afterwards, the solution was dialyzed using a float-A-lyzer MWCO 3.5–5.0 kDa against water for 24 h to remove free-dye and the organic solvent. The Cy7-PHPMA$_{35}$-*b*-PDPA$_{75}$ block copolymer conjugate was recovered by lyophilization with a yield of 56%.

2.4. Manufacturing and characterization of the pH-responsive polymersomes

The DOX-free and DOX-loaded PSs were produced by microfluidics. The block copolymer PHPMA$_{35}$-*b*-PDPA$_{75}$ (5.0 mg) was dissolved in THF/MeOH (60/40) (*v/v*), and the organic solution was pumped through the middle channel of a microfluidic device (Dolomite, United Kingdom) equipped with a glass Micromixer chip of 12 mixing stages micro-channels with 50 μm × 125 μm (depth × width) and 3 inlet channels. The PBS buffer (pH 7.4) was pumped through the side channels. The solutions were pumped to the microfluidic device using two independent Dolomite Mitos P-Pumps controlled *via* PC software. The flow rates were 200 μL·mL^{-1} (water phase) and 100 μL·mL^{-1} (organic phase). The polymer colloids were collected in vials and dialyzed against PBS (pH 7.4) during 12 h to remove the organic solvent. The preparation of the DOX-loaded PSs was conducted essentially using the same procedure with DOX dissolved in DMSO (5 μL) and mixed to the organic phase at drug feeding 20% *w/w*. The Cy7-labeled PSs were prepared in the same way using a mixture 1:1 *w/w* of PHPMA$_{35}$-*b*-PDPA$_{75}$ and Cy7-PHPMA$_{35}$-*b*-PDPA$_{75}$. The assemblies were characterized by dynamic (DLS) and electrophoretic (ELS) light scattering, besides small-angle X-ray scattering (SAXS) and cryogenic transmission electron microscopy (cryo-TEM). The details concerning these methods are given in the Supporting Information File.

2.5. Determination of DOX loading content and DOX encapsulation efficiency

The DOX loading content (DLC) and loading efficiency (LE) were determined by HPLC. The quantities were determined by using an analytical curve with a linear response in the range 0.001–0.5 mg·mL^{-1}. The values were calculated using the following equations:

$$DLC\ (\%) = \frac{DOX\ amount\ in\ PSs}{Mass\ of\ PSs}\ X\ 100 \quad (1)$$

$$LE\ (\%) = \frac{DOX\ amount\ in\ PSs}{DOX\ Feeding}\ X\ 100 \quad (2)$$

The measurements were performed in triplicate and mean values are reported.

2.6. In Vitro DOX Release

The *in-vitro* DOX cumulative release was evaluated by the dialysis method in PBS buffer at pH 7.4 (with and without 1% human plasma), pH 6.6, and in acetate buffer at pH 5.5. A pre-swollen cellulose dialysis membrane tube with MWCO 3.5–5 kDa (Spectra-Por® Float-A-Lyzer® G2) was filled with 2.0 mL of DOX-loaded PSs at 0.5 mg·mL^{-1}. The membrane tube was then immersed into 3 L of the buffers at 37 °C under stirring (500 rpm). At pre-determined times, 10 μL of the DOX-loaded PSs was taken from the membrane tube and diluted into 190 μL of DMSO to determine the amount of remaining DOX as measured by HPLC.

2.7. Biological assays

2.7.1. Cell culture

The T lymphocyte human Jurkat cells (ATCC, Poland) were cultured in RPMI-1640 medium supplemented with 100 units of penicillin and 100 μg·mL^{-1} streptomycin (Life Technologies, Czech Republic) with fetal bovine serum at a concentration of 10% *v/v*. The T lymphocyte mouse EL4 cells (ATCC, Poland) were cultured in Dulbecco's Modified Eagle's Medium (DMEM) supplemented with 100 units of penicillin and 100 μg·mL^{-1} streptomycin (Life Technology, Czech Republic). They were cultured at 37 °C with 5% CO_2 in 25 cm^2 flasks.

2.7.2. Cellular uptake

Flow cytometry analyses were used to quantify the cellular uptake of DOX-loaded PSs as compared to free DOX (the DOX content was set to 10 μg·mL^{-1}). The T lymphocyte cells (1 × 10^5 cells per well) were seeded into 24-well plate the day before incubation. The DOX-loaded PSs and free DOX were incubated for 2 h in 5% CO_2 and 37 °C. After the incubation time, the cells were centrifuged (1 500 rpm) and resuspended in 0.5 mL of PBS with 0.5% *v/v* BSA (this has been repeated two times). The data were acquired using a FACS Verse (Becton Dickinson) flow cytometer (10 000 events per sample) and they were further processed using the FlowJo software V7.6.1. The mean fluorescence intensity (MFI) values were determined and untreated cells were used as negative control. All samples were measured in triplicate in three independent experiments.

2.7.3. Cell viability

The T lymphocyte cell viability was determined using the Alamar Blue® reagent (Life Technologies, Czech Republic) according to the manufacture's protocol. The cells were seeded into 96-well plates (1 × 10^4 cells per well) and allowed to adhere for 24 h. Subsequently, the cells were exposed to serial dilutions of DOX-loaded PSs, DOX-free PSs and free DOX added to the medium at volume of 10 μL for 72 h in 5% CO_2 atmosphere at 37 °C. Subsequently, 10 μL of Alamar Blue® reagent was added to each well and incubated for 4 h in 5% CO_2 atmosphere at 37 °C. Resorufin, which is reduced from resazurin, is the active compound of the Alamar Blue® reagent. Resorufin is highly fluorescent only in the presence of viable cells, and the fluorescence intensity was measured with a Synergy Neo plate reader (Bio-Tek, Prague, Czech Republic) at $\lambda_{ex} = 570$ nm and $\lambda_{em} = 600$ nm. The negative control refers to untreated cells. All samples were measured in triplicate in three independent experiments.

2.7.4. Biodistribution

The biodistribution experiments were performed using female athymic nude foxnl^{nu} mice obtained from AnLab (Prague, Czech Republic). They were kept in a specific pathogen-free environment at constant temperature (21.5 ± 0.5 °C) and humidity (55 ± 5%), 15 air changes/h and 12 h light/dark cycle. Lymphoma EL4 cancer cells (5 × 10^5 cells) were injected subcutaneously into their right flank. After 7 days, the animals were divided into 2 groups ($n = 4$). The first group was treated with free dye (free Cy7) and the second with Cy7-PHPMA$_{35}$-*b*-PDPA$_{75}$ PSs. The Cy7 amount was set to 100 ng·mL^{-1} and 200 μL of the solutions were injected in the tail vein. The fluorescence signals were detected by using the *In Vivo* Xtreme Imaging System (Bruker, Germany) with excitation and emission filters of 750 nm and 830 nm. During the measurements, the mice were imaged at serial time points under inhalation anesthesia with 2% isoflurane (Baxter, United Kingdom). The blood samples were collected from the eyes for pharmacokinetics studies. The quantification of the fluorescence intensity was performed using the open-source image processing software ImageJ/Fiji [38]. Regions of interest (ROI) were selected based on tumor boundaries visible in reflectance and the mean fluorescence intensity in the tumors was

calculated as fluorescence intensity in ROI divided by area of ROI. The mice were sacrificed 144 h after administration of the formulations and the fluorescence intensity was measured in tumor, heart, intestine, kidneys, liver, lungs and spleen. The fluorescence intensities were normalized to the weight of the organs.

2.7.5. In vivo antitumor activity

The *in vivo* antitumor activity of the DOX-loaded PSs was evaluated in female C57BL/6 black mice bearing EL4 lymphoma tumors. Six to eight-week-old C57BL/6 female mice (Anlab, Czech Republic) were used for tumor shrink study (food and water were given *ad libitum*). The right-flank was shaved and EL4 lymphoma cells (5×10^5) were injected subcutaneously. Seven days later, mice with well-grown tumors (size 0.15–0.20 cm^3) were randomly distributed into 3 groups (7 animals/group). The treatment consisted of three injections of 5 mg DOX (or equivalent)/kg dissolved in sodium chloride 0.9% injection (saline solution) administrated intravenously *via* the tail vein. The injections were performed at days 0, 4, and 8. The control group was treated with saline solution, the second group received DOX and the third group received the DOX-loaded polymersomes. Blood samples were collected from the eyes for enzyme quantification. The tumor growth and body weight were monitored every two days for 40 days. The tumor size was measured by a caliper, and the volume (V) was calculated as $V = (\alpha \times b^2 \times \pi)/6$ where α is the length and b the width of the tumor surface area. The survival mice % is given as a Kaplan-Meier plot.

2.7.6. Determination of serum markers of cardiotoxicity

Blood samples were collected from the retro-orbital sinus of anesthetized animals (using inhalation anesthesia with 3% isoflurane) into non-heparinized capillary tubes at day 10 after the third injection. The plasma was separated by centrifugation at 4000 rpm and 4 °C, and stored at −80 °C for further analyses. The enzyme activity of lactate dehydrogenase (LDH) and creatine kinase (CK) were determined using commercially available kits and based on standard protocols.

2.7.7. Blood biochemistry examinations

Peripheral blood samples were collected from the retro-orbital sinus of anesthetized animals and stored into capillaries containing ~2 μL of 0.5 $mol \cdot L^{-1}$ ethylenediaminetetraacetate (EDTA) solution (Sigma Aldrich, Czech Republic). The first blood samples were taken before EL4 tumor cell application and subsequent samples were taken every seven days. The blood samples were analyzed with a BV5300 veterinary hematology analyzer (Mindray, China) and by flow cytometry. The blood cells were pelleted by centrifugation (400 ×*g*, 5 min, 4 °C) and the cells were then stained with a mixture of fluorochrome-conjugated antibodies against lineage markers: anti CD4 (T_h lymphocytes) and anti CD8 (T_c lymphocytes). All the antibodies (Table S1 - Supporting Information File) were purchased from BioLegend (USA). The cells were incubated with the antibody mixture (20 min on ice and dark), washed with PBS and analyzed using a digital FACS Canto II flow cytometer equipped with 405 nm (60 mW), 488 nm (20 mW) and 633 nm (15 mW) lasers, and applicable configuration of optical filters and signal detectors (BD Biosciences, USA). The flow cytometry data were analyzed using FlowJo Vx software (Tree Star, USA).

All the reported *in vivo* experiments were conducted in accordance with The Law of Animal Protection against Cruelty (Act No. 359/2012) of the Czech Republic. The experiments were conducted in accordance with the authority-approved protocol (MSMT-34384/2019–2), leaving the animals left to life. The biodistribution, tumor accumulation and cardiotoxicity were evaluated based on the legislation of Experimental Work with Animals (act no. 246/1992 of the Czech Republic and decree no. 419/2012) that are in full agreement with the European Union directives.

2.8. Statistical analysis

The two-way ANOVA test was used to establish statistical differences among groups. The analyses were performed using the GraphPad Prims 6 software (GraphPad Inc., United States), and $p < 0.05$ was considered statistically significant.

3. Results and discussion

3.1. Preparation and characterization of the DOX-loaded polymersomes

The Fig. 1 summarizes the data with regard to the structural features of the DOX-free and DOX-loaded PSs along with the molecular structure of $PHPMA_{35}$-*b*-$PDPA_{75}$. The measured values are given in Table 1.

The $PHPMA_{35}$-*b*-$PDPA_{75}$ block copolymer was successfully synthetized by RAFT polymerization. The azide-terminated PHPMA macro-chain transfer agent (azide-macro-CTA) was firstly synthesized (M_n = 5000 $g \cdot mol^{-1}$, $Đ$ = 1.06). The molecular characteristics assessed by FTIR, ^1H NMR and SEC are provided in the Supporting Information File (Figs. S1-S3). Subsequently, the PDPA block was grown from the macro-CTA also by RAFT. The synthetic strategy is given in Fig. S4 (Supporting Information File). The block copolymer is *non-biodegradable* and therefore, the molecular weight was selected to ensure body clearance of the chains (M_w ~ 22 kDa). The value is notably below the renal threshold filtration which has a commonly accepted limit for polymers within the range of 40–50 kDa [39,40]. Accordingly, the *in vivo* clearance of the polymer chains is predictable. The optimized conditions for the manufacturing of the pH-responsive PSs were previously established [35]. The use of microfluidics enabled the production of highly uniform self-assemblies with precise control over size and high reproducibility over different batches. The polymer colloids were stable over months when stored at 4 °C. The sizes of the DOX-free (102 nm) and DOX-loaded (95 nm) polymersomes are not statistically different when the reported standard deviations are taken into account. The presence of the fluorophore similarly does not significantly impact the final size of the assemblies. The dimension is indeed desirable for the long circulation and tumor accumulation of nanomedicines [41,42]. The manufactured assemblies are narrowly distributed in size (PDI < 0.10). The slightly negatively charged surfaces are appropriate for colloidal nanocarriers, because higher positive or negative values are normally linked to fast blood clearance [43]. The value of ζ-potential indicates effective shielding and steric stabilization of the polymeric vesicles promoted by the PHPMA shell [43–45]. The reduction in this parameter for DOX-loaded PSs may be caused by drug adsorption at the outer surface of the assemblies. Since DOX has a cationic character in pH 7.4 (pKa = 9.9) [46], it may partially neutralize the negative surface of the polymersomes. Nevertheless, we highlight that the difference is tiny and only the presence of small amounts of DOX at the outer surface of the vesicles can be speculated. The self-assembly of $PHPMA_{35}$-*b*-$PDPA_{75}$ into PSs was robustly confirmed by SAXS (Fig. 1C) and cryo-TEM (Fig. 1D and E). The cryo-TEM images highlight predominantly the presence of vesicular structures (~ 70–90 nm) in reasonable agreement with the size distributions obtained by DLS (Fig. 1B). Indeed, TEM data usually undersize relative to DLS because the last one is weighted by light scattering intensity, whereas TEM gives number-average diameters. Additionally, DOX crystals were observed in the aqueous lumen of the DOX-loaded PSs (Fig. 1E). This is typically observed in liposomal formulations containing DOX [47,48]. Considering the determined drug loading content (10%), respective concentration in the sample (0.1 $mg \cdot mL^{-1}$) and the determined values of N_{agg} and R_H, the DOX concentration inside the vesicles was estimated to be at least 32 mM which is higher than the threshold concentration at which these structures can be evidenced [47]. The well-defined SAXS patterns given in Fig. 1C could be properly fitted only by using the bilayer vesicle form factor with the thickness of the hydrophilic PHPMA shell in contact with water (t_h = 4.5 nm) and the thickness of the hydrophobic PDPA layer (t_t = 10.7 nm) as adjustable

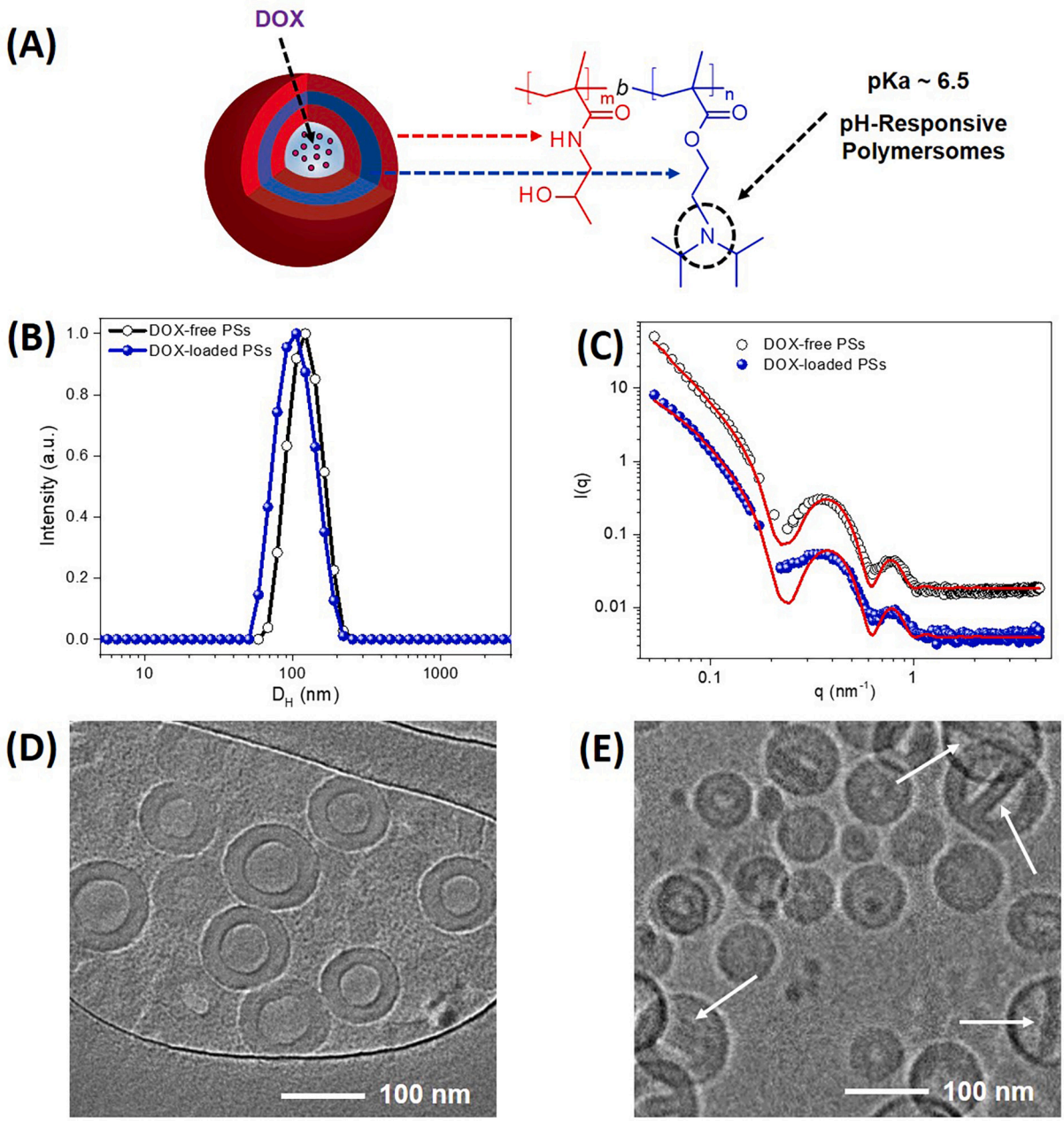

Fig. 1. Molecular structure and schematic representation of DOX-loaded self-assembled $PHPMA_{35}$-*b*-$PDPA_{75}$ PSs (A); size distributions obtained by DLS (B) and analogous SAXS data (C) for DOX-free and DOX-loaded PSs; cryo-TEM imagens for DOX-free (D) and DOX-loaded (E) PSs (arrows depict DOX crystals).

parameters (DOX-free PSs). These dimensions were essentially not affected by DOX loading (t_h = 4.4 nm and t_t = 10.8 nm).

The DOX loading content and encapsulation efficiency were determined as 10% and 53%, respectively. The DOX release profile was subsequently evaluated in simulated blood (pH 7.4, with and without serum medium), pathophysiological condition (pH ~ 6.5) and the acid environment of endosomes and lysosomes (pH ~ 5.5). These data are reported in Fig. 2A. The DOX is released much faster in the acidic environments. The protonation of the PDPA block causes the disassembly of the vesicles when pH < pKa ~ 6.8, thereby promoting DOX release. At this condition, ~ 70–80% of the encapsulated DOX is released within 24 h and 80–90% after 48 h. On the other hand, DOX-loaded PSs are stable at physiological pH (pH 7.4) and under such environmental condition, roughly 22% of the encapsulated DOX is released within the first 24 h, and only 31% cumulative release has been monitored after 72 h. Similar behavior has been observed also in serum medium at the same pH.

3.2. *In vitro assays*

The cellular uptake and cytotoxicity of the produced PSs were further evaluated by putting them in contact with EL4 lymphoma and Jurkat cells. The results were compared to those of free DOX at equivalent amounts. The mean fluorescence intensity (MFI) values estimated from the DOX cellular uptake are given in Figs. 2B. The intrinsic fluorescence intensity of DOX is useful to evaluate its cellular uptake. The results demonstrate that the amount of DOX uptaken by the cells is similar, regardless of its encapsulation or not, although only free DOX is presumably able to be internalized by the cells *via* the diffusion pathway, whereas DOX-loaded PSs are possibly internalized only by endocytosis due to their large size. The data reported in Fig. 2B are indeed not statistically different ($p < 0.05$). The *in vitro* anticancer performance of the DOX-loaded PSs was subsequently evaluated in both cell lines and compared to free DOX (Fig. 2C–D). The IC_{50} values for EL4 lymphoma

Table 1
Structural features of the prepared DOX-free and DOX-loaded PSs.

Entry	D_H (nm)[a]	PDI[a]	t_t (nm)[b]	t_h (nm)[b]	ζ potential (mV)[c]	DLC (%)[d]	LE (%)[d]
DOX-free PSs	102 ± 6	0.06 ± 0.01	10.7	4.5	−8.8 ± 0.6	–	–
DOX-loaded PSs	95 ± 6	0.08 ± 0.01	10.8	4.4	−3.9 ± 0.4	10 ± 2	53 ± 4
Cy7-PSs	93 ± 4	0.05 ± 0.01	–	–	−11.3 ± 1.4	–	–

t_t: thickness of the PDPA hydrophobic layer; t_h: thickness of the PHPMA hydrophilic layer.
[a] Measured by DLS.
[b] Measured by SAXS.
[c] Measured by ELS.
[d] Measured by HPLC.

cells are 0.034 and 0.021 μg·mL^{-1} for DOX-loaded PSs and free DOX, and respectively 0.064 and 0.036 μg·mL^{-1} for Jurkat cells. The fairly similar values confirm that the assemblies are efficient in delivering the chemotherapeutic agent to both cell lines, thereby causing efficient cytotoxic effects. The slightly lower IC_{50} values for free DOX is possibly associated to its ability to diffuse across the cell membranes [49]. The viability of cells in contact with DOX-free (unloaded) polymersomes suggests negligible cytotoxicity effect of the nanoplatform since the values are above 70% (Fig. S5A - Supporting Information File) in the same concentration range. The behavior was similarly confirmed in other cell lines [35].

3.3. In vivo assays

3.3.1. Biodistribution of PHPMA$_{35}$-*b*-PDPA$_{75}$ polymersomes in nude mice

The biodistribution assays were performed using the fluorescent dye DBCO-Cyanine7 (Cy7), which can be detected in deep tissues *in vivo* [50]. The nu/nu mouse strain was selected for biodistribution assays to reduce the background signal during fluorescence detection. The polymeric vesicles were produced using a mixture 1:1 *w/w* of PHPMA$_{35}$-*b*-PDPA$_{75}$ and Cy7-PHPMA$_{35}$-*b*-PDPA$_{75}$ which nevertheless does not modify the final size and polydispersity of the self-assembled vesicles (93 nm; 0.05). The biodistribution data are reported in Fig. 3.

The fluorescence intensities of free Cy7 and Cy7-PHPMA$_{35}$-*b*-PDPA$_{75}$ PSs are similar at $t = 0.5$ h (Fig. S6 - Supporting Information File) however, the fluorescence signal of free Cy7 decreases remarkably faster and almost vanishes after 24 h of injection, which is very different compared to the behavior reported for Cy7-PSs (Fig. 3A–B). The fluorescent signal from Cy7-PSs is somehow distributed throughout the mice even after 6 days of injection. These data notably highlight that the pH-responsive polymeric vesicles remain *in vivo* for a fairly long time. The results reported in Fig. 3C highlight that 96 h after the administration, the fluorescence intensity in the tumor is still higher than 50% compared to the value initially monitored (0.5 h).

The mice were subsequently sacrificed by cervical dislocation to obtain tissue samples for quantification analysis. The relative amounts of Cy7 in different organs were determined by mean fluorescence intensities in ROI (based on tumor boundaries visible in reflectance). The higher amounts were found in liver and spleen after the timescale of the experiment (Fig. 3D) nonetheless, enhanced accumulation is also noticed at the tumor region for Cy7-PSs. The smallest amount was found in the heart tissue suggesting reduced cardiotoxic effects. The images in

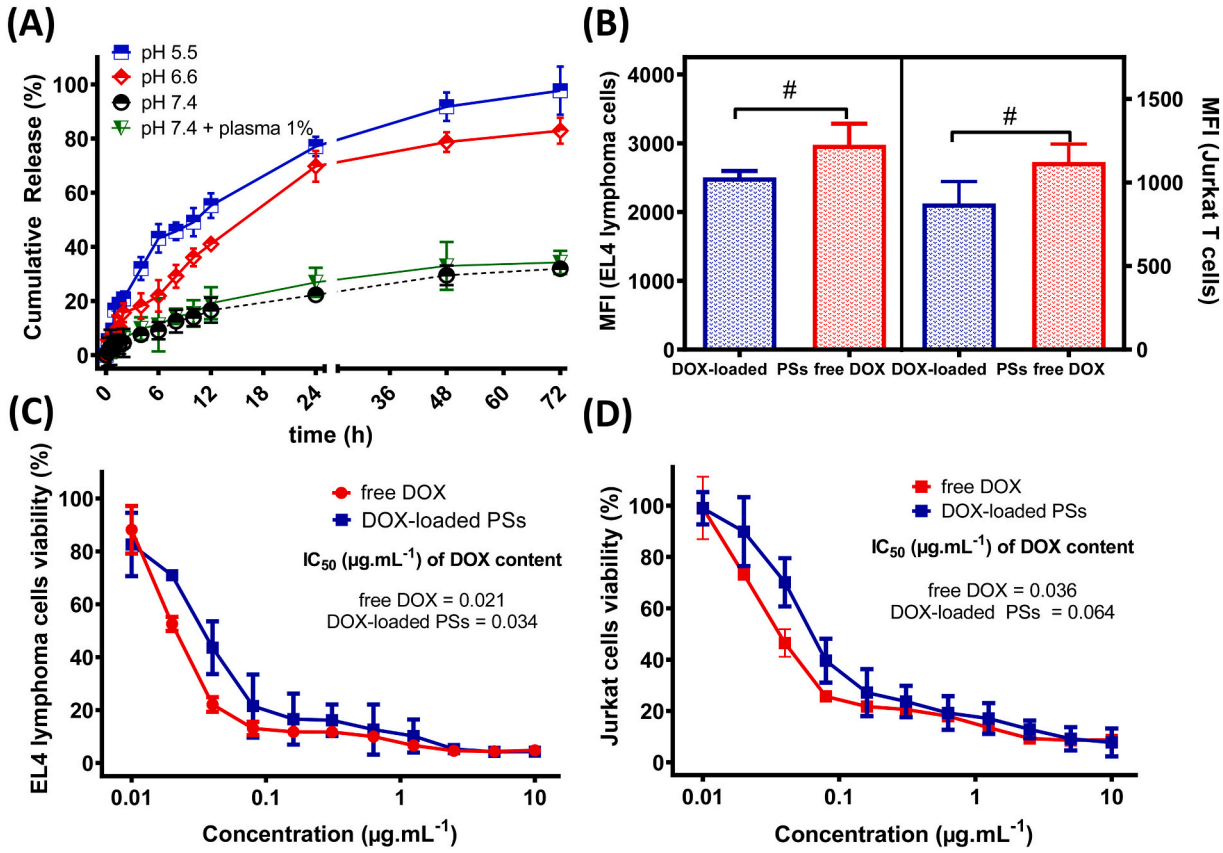

Fig. 2. Cumulative DOX release from PHPMA$_{35}$-*b*-PDPA$_{75}$ PSs at different pH and in serum environment (A); Cellular uptake of free DOX and DOX-loaded PSs as determined by flow cytometry (MFI per 10,000 events) after 2 h incubation time with EL4 lymphoma and Jurkat cells (B); EL4 lymphoma (C) and Jurkat (D) cell viability % after 72 h of contact with free DOX and DOX-loaded PSs. # in 2B represent non-significant differences ($p < 0.05$).

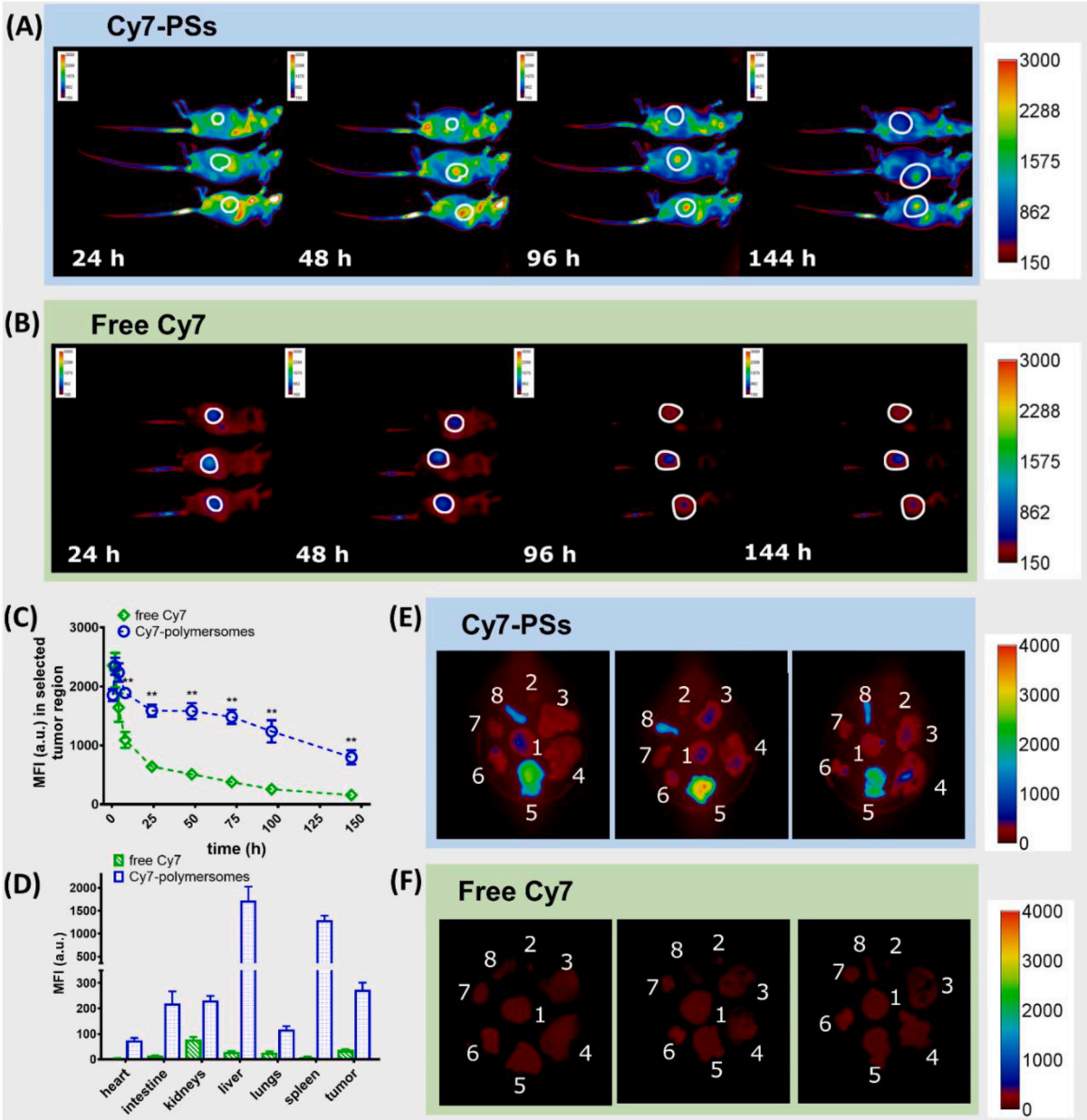

Fig. 3. *In vivo* biodistribution analysis of Cy7-PSs (A) and free fluorescent dye DBCO-Cy7 (free Cy7) (B) as a function of time (the white circles assign the tumor area) in mice bearing EL4 T lymphoma tumors; (C) Mean fluorescence intensity (MFI) as a function of time monitored *in-vivo* at the tumor region of nude mice bearing EL4 T lymphoma tumor (** represents statistically significant difference of at least $p < 0.05$ between Cy7 and Cy7-PSs as provided by one-way ANOVA; $n = 3$ mice/group); (D) *ex-vivo* Cy7-PSs accumulation in different organs and in EL4 T lymphoma tumor after 7 days of administration; *Ex-vivo* images of tumor and organs (1: tumor; 2: heart; 3: small intestine; 4: large intestine and cecum; 5: liver; 6: kidneys; 7: lungs; 8: spleen) after 7 days of administration of Cy7-PSs (E) and free Cy7 (F).

Fig. 3E and F corroborate the tumor accumulation, however higher intensities are note in the spleen and liver as commonly observed in such type of treatment.

3.3.2. *In vivo antitumor activity and cardiotoxicity evaluation*

We have observed negligible cytotoxicity of the pure assemblies *in vitro* as previously underlined. Moreover, DOX-free $PHPMA_{35}$-*b*-$PDPA_{75}$ polymersomes were administrated in healthy C57BL/6 black mice and no notable body weight change along 21 days has been monitored (Fig. S5B - Supporting Information File). The *in vivo* therapeutic effect of the DOX-loaded PSs was then further investigated in C57BL/6 black mice bearing EL4 lymphoma tumors. The data regarding tumor volume, body weight change and survival rate are given in Fig. 4A–C.

The reported data indeed highlight the antitumor activity of the DOX-loaded PSs. The aggressiveness of the EL4 lymphoma tumor leads to rapid growth of the tumor volume in untreated mice (saline), causing the death of the whole group within 22 days. The treatment with free DOX is not effective to reduce the tumor volume and, taking into account the drug half-life (30 min - 3 h) [51,52], the fast clearance of the therapeutic agent is presumably linked to the ineffective reduction in tumor growth. Nevertheless, the free DOX treatment prolongs the survival time by roughly 10–14 days. The visual inspection of the control group (saline) and the group treated with free DOX revealed the presence of ulcerated and necrotic tumors. Representative images of different groups during the treatment are provided in the Supporting Information File (Fig. S7).

On the other hand, tumor volume reduction was clearly observed when the mice were treated with DOX-loaded PSs. The body weight

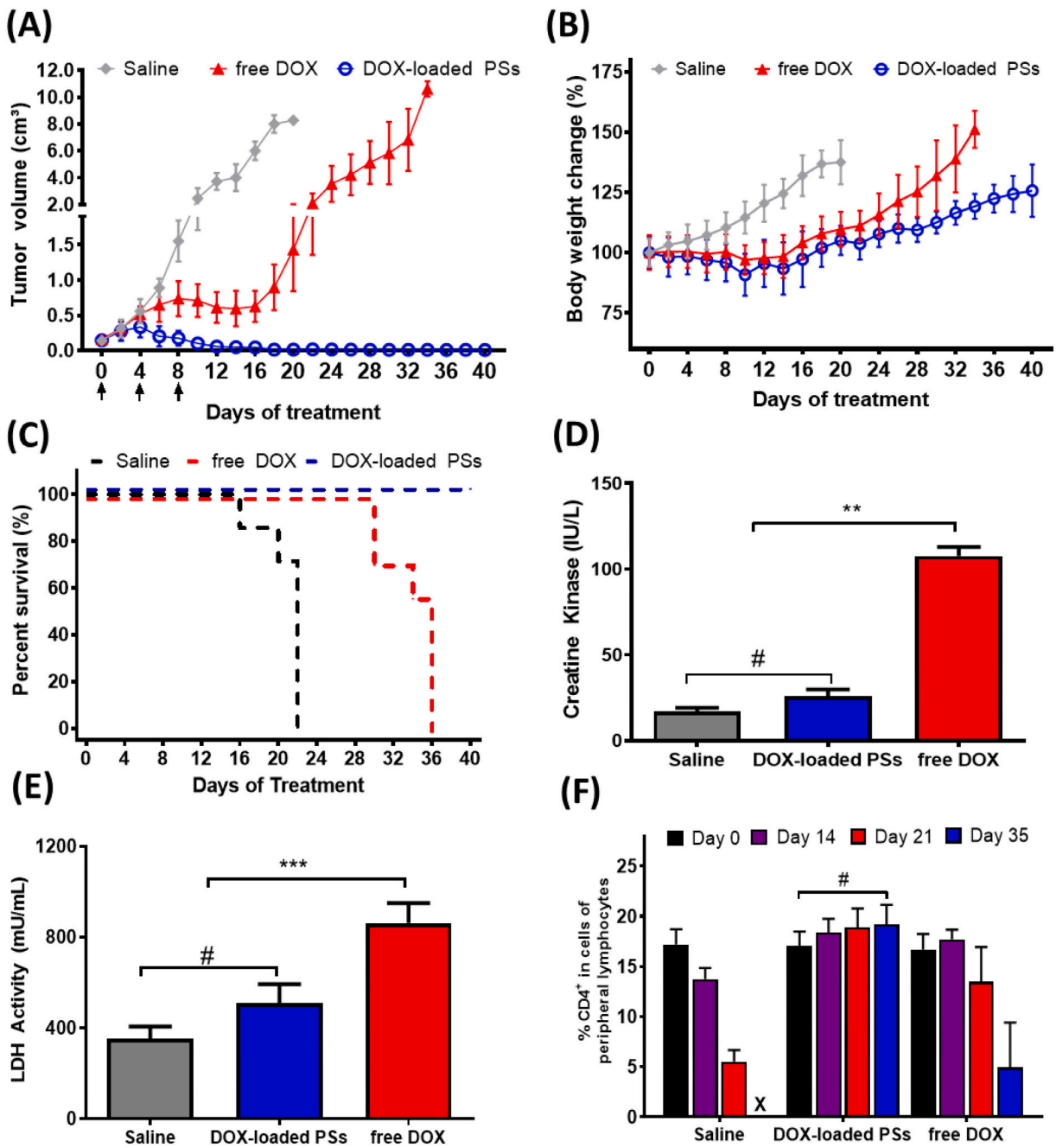

Fig. 4. Tumor volume in cm^3 (A), body weight change % (B), and Kaplan-Meier survival plot (C) as a function of time for mice treated with saline, DOX-loaded PSs and free DOX at 5 mg·kg^{-1} DOX or equivalent according to the legends (the data are given as mean ± SD; $n = 7$). The arrows indicate the days of DOX or equivalent administrations. Serum creatine kinase - CK (D) and lactate dehydrogenase - LDH (E) levels after free DOX and DOX-loaded PSs administration (10 days after third injection) in mice bearing EL4 lymphoma tumors (the data are given as mean ± SD). Quantification of CD4+ cells in peripheral blood during the chemotherapeutic treatment using free DOX, DOX-loaded PSs and saline (F). # non-significant difference ($p < 0.05$); ** statistically significant difference ($p < 0.05$); *** statistically significant difference ($p < 0.005$).

increased quickly in the control group and in the group treated with free DOX due to the faster tumor growth, whereas the body weight within the first 20 days was maintained in the group treated with DOX-loaded PSs. The animals looked healthy, and they started to gain weight afterwards. Most important, the survival rate was maintained at 100% without deaths in the treated group within the timescale of the experiment (40 days), thereby demonstrating the effectiveness of the DOX-loaded pH-responsive PSs in suppressing tumor growth and extending mouse survival time. Such outstanding result can presumably be attributed to the preferred tumor accumulation of the nanomedicines as evidenced in the data reported in Fig. 3, and the pH-responsive behavior of PDPA enabling triggered and fast DOX release in slightly acid environments. Additionally, in the groups treated with free DOX, hair loss in the flank-caudal region was observed. This is a side effect of chemotherapeutic treatments that nevertheless has not been observed in the group treated with DOX-loaded PSs (Fig. S8 - Supporting Information File).

In the step further, blood samples collected 10 days after the third injection (day 18) were selected for CK and LDH quantification. The cardiotoxicity is one of the main drawbacks of therapeutic treatments based on DOX [10], and measuring the production of these specific enzymes is a common approach to identify cardiotoxic effects [53,54], although the markers can also be used to probe the toxicity to other

organs. The data reported in Fig. 4D and E clearly reveals higher CK and LDH levels in the plasma of the group treated with free DOX, whereas the levels of these clinically well-established markers of biochemical cardiomyocyte damage are remarkably lower when DOX was loaded into the polymeric vesicles, therefore suggesting reduced cardiotoxic effects.

Finally, the quantitative values of $CD4^+$ and $CD8^+$ cells were determined by flow cytometry during the chemotherapeutic treatment. Fig. 4F reports the levels of $CD4^+$ detected in mice treated with free DOX and DOX-loaded PSs, and the values for $CD8^+$ cells are given in the Supporting Information File (Fig. S9). The $CD4^+$ and $CD8^+$ cells play an important role in the immune system as they are associated with the production of T helper and cytotoxic T cells, respectively. The level of $CD4^+$ cells consistently reduces over time for untreated mice (saline) reaching a value of ~7% after 21 days. The level of $CD4^+$ cells in mice treated with free DOX remained at similar levels during the first two weeks of treatment, and then it decreases leading to a loss of therapeutic response presumably linked to free DOX clearance which consequently induce increased tumor volume (Fig. 4A). On the other hand, the treatment using the pH-responsive DOX-loaded PSs promote an augmentation in the % of $CD4^+$ (and also $CD8^+$, Fig. S9) cells during the timescale of the experiment suggesting anti-tumor T-cell immunity aiding the tumor suppression.

Taken together, the results underline the potential DOX delivery into solid tumors by using the proposed pH-responsive nanoplatform. We have explored the known acidic tumor microenvironment to achieve preferred drug accumulation by using a supramolecular structure sensitive to the low local pH. The strategy provided enhanced efficacy of DOX with remarkably reduced side effects. The findings are expected to have future implications in the success of chemotherapies based on this active agent.

4. Conclusions

The engineering of DOX-loaded pH-responsive polymeric vesicles by using the block copolymer $PHPMA_{35}$-*b*-$PDPA_{75}$ as the building unit is reported. The stimuli-responsive supramolecular self-assemblies have been rationally designed to respond the extracellular tumor acidosis and they could be successfully loaded with 10% *w/w* DOX while maintaining colloidal stability. The designed nanoplatform enabled effective growth inhibition of EL4 lymphoma tumor with 100% survival rate over 40 days, and with reduced cardiotoxic effect. The proposed pH-switchable system may constitute a step forward in the design of carriers for cancer treatment. The low drug leakage in conditions mimicking the bloodstream possibly reduces DOX plasma concentration, thus attenuating unwanted side effects. Alongside, the biodistribution data suggest that high DOX doses can be preferably administered in localized acidic tumor tissues, and bypassing the ABC phenomenon thanks to the presence of PHPMA at the outer surface of the assemblies. Truthfully, drug leakage and short plasma half-life are commonly underlined as main drawbacks of non-pegylated liposomal doxorubicin [55,56], whereas the ABC effect is evidenced upon repeated administration of PEGylated DOX-loaded formulations [57].

Credit author statement

E.J. designed the experiments. L.J.C.A., V.S., A.J., J.K., J.H., and E.J. performed the experiments. A.J., V.S., and L.J.C.A. conduct the microfluidics. I.D., and I.T. conducted the cryo-TEM experiments. O.J. conducted the *in vitro* cell experiments. J.H., J.K., P.P., T.H., J.P., P.P., and L. S. contributed to the animal studies. L.J.C.A., J.H., J.P., M.H., F.C.G., P. S., and E.J. analyzed the data. L.C.J.A., F.C.G. and E.J. drafted the manuscript. The manuscript was written through contributions of all authors. All authors have given approval to the final version of the manuscript.

Declaration of Competing Interest

The authors declare no conflict of interest.

Acknowledgments

These investigations have been sponsored by the Czech Science Foundation (grant 20-15077Y) and by FAPESP (grant 2019/06634-8). A.J. acknowledges Czech Science Foundation (grant 20-13946Y). P.S. acknowledges grant LM2018133 ERIC and POLYMAT grant LO1507. M. H thanks the Ministry of Education, Youth and Sports of the Czech Republic (grant INTER-COST # LTC19032). L.J.C.A. acknowledges FAPESP (grants 2016/23844-8 and 2017/11261-0). The CAPI experiments were supported by Ministry of Education, Youth and Sports of the Czech Republic (Large RI Project LM2018129 Czech-BioImaging), by Charles University (SVV 260519/2020) and by European Regional Development Fund (Project CZ.02.1.01/0.0/0.0/16_013/0001775). The cryo-TEM work was performed at the Technion Center for Electron Microscopy of Soft Matter, supported by the Technion Russell Berrie Nanotechnology Institute (RBNI).

Appendix A. Supplementary data

Supplementary data to this article can be found online at https://doi.org/10.1016/j.jconrel.2021.03.013.

References

[1] Latest Global Cancer Data, Cancer burden rises to 18.1 million new cases and 9.6 million cancer deaths in 2018, 2018. https://www.who.int/cancer/PRGlobocanFinal.pdf?ua=1 (accessed September 20, 2020).
[2] R.L. Siegel, K.D. Miller, A. Jemal, Cancer statistics, 2019, CA Cancer J. Clin. 69 (2019) 7–34, https://doi.org/10.3322/caac.21551.
[3] T. Yamauchi, A. Yoshida, T. Ueda, Camptothecin induces DNA strand breaks and is cytotoxic in stimulated normal lymphocytes, Oncol. Rep. 25 (2011) 347–352, https://doi.org/10.3892/or.2010.1100.
[4] T. Rupp, D. Zuckerman, Quality of life, overall survival, and costs of cancer drugs approved based on surrogate endpoints, JAMA Intern. Med. 177 (2017) 276–277, https://doi.org/10.1001/jamainternmed.2016.7761.
[5] H. Maeda, M. Khatami, Analyses of repeated failures in cancer therapy for solid tumors: poor tumor-selective drug delivery, low therapeutic efficacy and unsustainable costs, Clin. Transl. Med. 7 (2018) 1–20, https://doi.org/10.1186/s40169-018-0185-6.
[6] D. Patt, M. Gauthier, S. Giordano, Paclitaxel in breast cancer, Women's Heal. 2 (2006) 11–21, https://doi.org/10.2217/17455057.2.1.11.
[7] A.U. Buzdar, C. Marcus, G.R. Blumenschein, T.L. Smith, Early and delayed clinical cardiotoxicity of doxorubicin, Cancer. 55 (1985) 2761–2765, https://doi.org/10.1002/1097-0142(19850615)55:12<2761::AID-CNCR2820551206>3.0.CO;2-P.
[8] M.J. Gil-Gil, M. Bellet, S. Morales, B. Ojeda, L. Manso, C. Mesia, E. Garcia-Martínez, N. Martinez-Jáñez, M. Melé, A. Llombart, S. Pernas, P. Villagrasa, C. Blasco, J. Baselga, Pegylated liposomal doxorubicin plus cyclophosphamide followed by paclitaxel as primary chemotherapy in elderly or cardiotoxicity-prone patients with high-risk breast cancer: results of the phase II CAPRICE study, Breast Cancer Res. Treat. 151 (2015) 597–606, https://doi.org/10.1007/s10549-015-3415-2.
[9] E.A. Perez, V.J. Suman, N.E. Davidson, P.A. Kaufman, S. Martino, S.R. Dakhil, J. N. Ingle, R.J. Rodeheffer, B.J. Gersh, A.S. Jaffe, Effect of doxorubicin plus cyclophosphamide on left ventricular ejection fraction in patients with breast cancer in the north central cancer treatment group N9831 intergroup adjuvant trial, J. Clin. Oncol. 22 (2004) 3700–3704, https://doi.org/10.1200/JCO.2004.03.516.
[10] S. Turakhia, C.D. Venkatakrishnan, K. Dunsmore, H. Wong, P. Kuppusamy, J. L. Zweier, G. Ilangovan, Doxorubicin-induced cardiotoxicity: direct correlation of cardiac fibroblast and H9c2 cell survival and aconitase activity with heat shock protein 27, Am. J. Physiol. Heart Circ. Physiol. 293 (2007) H3111–H3121, https://doi.org/10.1152/ajpheart.00328.2007.
[11] N. Katsumata, Y. Fujiwara, T. Kamura, T. Nakanishi, M. Hatae, D. Aoki, K. Tanaka, H. Tsuda, S. Kamiura, K. Takehara, T. Sugiyama, J. Kigawa, K. Fujiwara, K. Ochiai, R. Ishida, M. Inagaki, K. Noda, Phase II clinical trial of pegylated liposomal doxorubicin (JNS002) in Japanese patients with müllerian carcinoma (Epithelial ovarian carcinoma, primary carcinoma of fallopian tube, peritoneal carcinoma) having a therapeutic history of platinum-based chem, Jpn. J. Clin. Oncol. 38 (2008) 777–785, https://doi.org/10.1093/jjco/hyn101.
[12] T.O.B. Olusanya, R.R.H. Ahmad, D.M. Ibegbu, J.R. Smith, A.A. Elkordy, Liposomal drug delivery systems and anticancer drugs, Molecules 23 (2018) 1–17, https://doi.org/10.3390/molecules23040907.
[13] Doxorubicin Market By Application, (Ovarian, Multiple Myeloma, Kaposi Sarcoma, Leukemia, Bone Sarcoma, Breast, Endometrial, Gastric, Liver, Kidney, Other

Cancers), And Segment Forecasts, 2018–2024. http://www.grandviewresearch.com/industry-analysis/doxorubicin-market, 2016.
[14] J. Qiao, H. Fang, Hand-foot syndrome related to chemotherapy, Can. Med. Assoc. J. 184 (2012) E818, https://doi.org/10.1503/cmaj.111309.
[15] B. Zhang, Q. Li, C. Shi, X. Zhang, Drug-induced pseudoallergy: a review of the causes and mechanisms, Pharmacology 101 (2018) 104–110, https://doi.org/10.1159/000479878.
[16] I.C. Macdougall, K. Vernon, Complement activation-related pseudo-allergy: a fresh look at hypersensitivity reactions to intravenous Iron, Am. J. Nephrol. 45 (2017) 60–62, https://doi.org/10.1159/000451069.
[17] P. Zhang, F. Sun, S. Liu, S. Jiang, Anti-PEG antibodies in the clinic: current issues and beyond PEGylation, J. Control. Release 244 (2016) 184–193, https://doi.org/10.1016/j.jconrel.2016.06.040.
[18] B. Neun, Y. Barenholz, J. Szebeni, M. Dobrovolskaia, Understanding the role of anti-PEG antibodies in the complement activation by doxil in vitro, Molecules. 23 (2018) 1700, https://doi.org/10.3390/molecules23071700.
[19] A. Moreno, G.A. Pitoc, N.J. Ganson, J.M. Layzer, M.S. Hershfield, A.F. Tarantal, B. A. Sullenger, Anti-PEG antibodies inhibit the anticoagulant activity of PEGylated aptamers, Cell Chem. Biol. 26 (2019), https://doi.org/10.1016/j.chembiol.2019.02.001, 634–644.e3.
[20] A.S. Abu Lila, H. Kiwada, T. Ishida, The accelerated blood clearance (ABC) phenomenon: clinical challenge and approaches to manage, J. Control. Release 172 (2013) 38–47, https://doi.org/10.1016/j.jconrel.2013.07.026.
[21] Q. Yang, S.K. Lai, Anti-PEG immunity: emergence, characteristics, and unaddressed questions, Wiley Interdiscip. Rev. Nanomedicine Nanobiotechnology. 7 (2015) 655–677, https://doi.org/10.1002/wnan.1339.
[22] H. Kiwada, Accelerated clearance of pegylated liposomes in rats after repeated injections, J. Control. Release 88 (2003) 35.
[23] P.H. Kierstead, H. Okochi, V.J. Venditto, T.C. Chuong, S. Kivimae, J.M.J. Fréchet, F.C. Szoka, The effect of polymer backbone chemistry on the induction of the accelerated blood clearance in polymer modified liposomes, J. Control. Release 213 (2015) 1–9, https://doi.org/10.1016/j.jconrel.2015.06.023.
[24] T. Minko, HPMA copolymers for modulating cellular signaling and overcoming multidrug resistance, Adv. Drug Deliv. Rev. 62 (2010) 192–202, https://doi.org/10.1016/j.addr.2009.12.002.
[25] L. Simon-Gracia, H. Hunt, P.D. Scodeller, J. Gaitzsch, G.B. Braun, A.-M. A. Willmore, E. Ruoslahti, G. Battaglia, T. Teesalu, Paclitaxel-loaded polymersomes for enhanced intraperitoneal chemotherapy, Mol. Cancer Ther. 15 (2016) 670–680, https://doi.org/10.1158/1535-7163.MCT-15-0713-T.
[26] L. Guan, L. Rizzello, G. Battaglia, Polymersomes and their applications in cancer delivery and therapy, Nanomedicine (Lond) 10 (2015) 2757–2780, https://doi.org/10.2217/nnm.15.110.
[27] H. De Oliveira, J. Thevenot, S. Lecommandoux, Smart polymersomes for therapy and diagnosis: fast progress toward multifunctional biomimetic nanomedicines, Wiley Interdiscip. Rev. Nanomedicine Nanobiotechnology. 4 (2012) 525–546, https://doi.org/10.1002/wnan.1183.
[28] K.K. Upadhyay, A.K. Mishra, K. Chuttani, A. Kaul, C. Schatz, J.-F. Le Meins, A. Misra, S. Lecommandoux, The in vivo behavior and antitumor activity of doxorubicin-loaded poly(γ-benzyl l-glutamate)-block-hyaluronan polymersomes in Ehrlich ascites tumor-bearing BalB/c mice, Nanomed. Nanotechnol. Biol. Med. 8 (2012) 71–80, https://doi.org/10.1016/j.nano.2011.05.008.
[29] C. Corbet, O. Feron, Tumour acidosis: from the passenger to the driver's seat, Nat. Rev. Cancer 17 (2017) 577–593, https://doi.org/10.1038/nrc.2017.77.
[30] B.A. Webb, M. Chimenti, M.P. Jacobson, D.L. Barber, Dysregulated pH: a perfect storm for cancer progression, Nat. Rev. Cancer 11 (2011) 671–677, https://doi.org/10.1038/nrc3110.
[31] F.C. Giacomelli, P. Stepánek, C. Giacomelli, V. Schmidt, E. Jäger, A. Jäger, K. Ulbrich, pH-triggered block copolymer micelles based on a pH-responsive PDPA (poly[2-(diisopropylamino)ethyl methacrylate]) inner core and a PEO (poly (ethylene oxide)) outer shell as a potential tool for the cancer therapy, Soft Matter 7 (2011) 9316–9325, https://doi.org/10.1039/c1sm05992k.
[32] E. Jäger, A. Jäger, P. Chytil, T. Etrych, B. Říhovaá, F.C. Giacomelli, P. Štěpánek, K. Ulbrich, Combination chemotherapy using core-shell nanoparticles through the self-assembly of HPMA-based copolymers and degradable polyesters, J. Control. Release 165 (2012) 153–161, https://doi.org/10.1016/j.jconrel.2012.11.009.
[33] L.W. Seymour, R. Duncan, J. Strohalm, J. Kopeek, Effect of molecular weight (Mw) ofN-(2-hydroxypropyl)methacrylamide copolymers on body distribution and rate of excretion after subcutaneous, intraperitoneal, and intravenous administration to rats, J. Biomed. Mater. Res. 21 (1987) 1341–1358, https://doi.org/10.1002/jbm.820211106.
[34] L. Brown, S.L. McArthur, P.C. Wright, A. Lewis, G. Battaglia, Polymersome production on a microfluidic platform using pH sensitive block copolymers, Lab Chip 10 (2010) 1922–1928, https://doi.org/10.1039/c004036c.
[35] L.J.C. Albuquerque, V. Sincari, A. Jäger, R. Konefał, J. Pánek, P. Černoch, E. Pavlova, P. Štěpánek, F.C. Giacomelli, E. Jäger, Microfluidic-assisted engineering of quasi-monodisperse pH-responsive polymersomes toward advanced platforms for the intracellular delivery of hydrophilic therapeutics, Langmuir 35 (2019), https://doi.org/10.1021/acs.langmuir.9b01009, 8363–8272.
[36] J. Xu, S. Zhang, A. MacHado, S. Lecommandoux, O. Sandre, F. Gu, A. Colin, Controllable microfluidic production of drug-loaded PLGA nanoparticles using partially water-miscible mixed solvent microdroplets as a precursor, Sci. Rep. 7 (2017) 1–12, https://doi.org/10.1038/s41598-017-05184-5.
[37] A. Jäger, E. Jäger, F. Surman, A. Höcherl, B. Angelov, K. Ulbrich, M. Drechsler, V. M. Garamus, C. Rodriguez-Emmenegger, F. Nallet, P. Štěpánek, Nanoparticles of the poly([N-(2-hydroxypropyl)]methacrylamide)-b-poly[2-(diisopropylamino) ethyl methacrylate] diblock copolymer for pH-triggered release of paclitaxel, Polym. Chem. 6 (2015) 4946–4954, https://doi.org/10.1039/C5PY00567A.
[38] C.A. Schneider, W.S. Rasband, K.W. Eliceiri, NIH image to ImageJ: 25 years of image analysis, Nat. Methods 9 (2012) 671–675, https://doi.org/10.1038/nmeth.2089.
[39] G. Pasut, F.M. Veronese, Polymer-drug conjugation, recent achievements and general strategies, Prog. Polym. Sci. 32 (2007) 933–961, https://doi.org/10.1016/j.progpolymsci.2007.05.008.
[40] M. Kissel, P. Peschke, V. Subr, K. Ulbrich, J. Schuhmacher, J. Debus, E. Friedrich, Synthetic macromolecular drug carriers: biodistribution of poly[(N-2-hydroxypropyl)methacrylamide] copolymers and their accumulation in solid rat tumors, PDA J. Pharm. Sci. Technol. 55 (2001) 191–201. http://www.ncbi.nlm.nih.gov/pubmed/11417110.
[41] J. Fang, H. Nakamura, H. Maeda, The EPR effect: unique features of tumor blood vessels for drug delivery, factors involved, and limitations and augmentation of the effect, Adv. Drug Deliv. Rev. 63 (2011) 136–151, https://doi.org/10.1016/j.addr.2010.04.009.
[42] A. Nel, E. Ruoslahti, H. Meng, New insights into "permeability" as in the enhanced permeability and retention effect of cancer nanotherapeutics, ACS Nano 11 (2017) 9567–9569, https://doi.org/10.1021/acsnano.7b07214.
[43] J.S. Lee, M. Ankone, E. Pieters, R.M. Schiffelers, W.E. Hennink, J. Feijen, Circulation kinetics and biodistribution of dual-labeled polymersomes with modulated surface charge in tumor-bearing mice: comparison with stealth liposomes, J. Control. Release 155 (2011) 282–288, https://doi.org/10.1016/j.jconrel.2011.07.028.
[44] A.H. Johnston, P.D. Dalton, T.A. Newman, Polymersomes, smaller than you think: ferrocene as a TEM probe to determine core structure, J. Nanopart. Res. 12 (2010) 1997–2001, https://doi.org/10.1007/s11051-010-9886-5.
[45] G. Wang, R.M. de Kruijff, D. Abou, N. Ramos, E. Mendes, L.E. Franken, H. T. Wolterbeek, A.G. Denkova, Pharmacokinetics of polymersomes composed of poly(butadiene-ethylene oxide); healthy versus tumor-bearing mice, J. Biomed. Nanotechnol. 12 (2016) 320–328, https://doi.org/10.1166/jbn.2016.2178.
[46] A.C. Alves, A. Magarkar, M. Horta, J.L.F.C. Lima, A. Bunker, C. Nunes, S. Reis, Influence of doxorubicin on model cell membrane properties: insights from in vitro and in silico studies, Sci. Rep. 7 (2017) 1–11, https://doi.org/10.1038/s41598-017-06445-z.
[47] X. Li, D.J. Hirsh, D. Cabral-Lilly, A. Zirkel, S.M. Gruner, A.S. Janoff, W.R. Perkins, Doxorubicin physical state in solution and inside liposomes loaded via a pH gradient, Biochim. Biophys. Acta Biomembr. 1415 (1998) 23–40, https://doi.org/10.1016/S0005-2736(98)00175-8.
[48] P.P. Wibroe, D. Ahmadvand, M.A. Oghabian, A. Yaghmur, S.M. Moghimi, An integrated assessment of morphology, size, and complement activation of the PEGylated liposomal doxorubicin products Doxil®, Caelyx®, DOXOrubicin, and SinaDoxosome, J. Control. Release 221 (2016) 1–8, https://doi.org/10.1016/j.jconrel.2015.11.021.
[49] C. Cui, Y.-N. Xue, M. Wu, Y. Zhang, P. Yu, L. Liu, R.-X. Zhuo, S.-W. Huang, Cellular uptake, intracellular trafficking, and antitumor efficacy of doxorubicin-loaded reduction-sensitive micelles, Biomaterials. 34 (2013) 3858–3869, https://doi.org/10.1016/j.biomaterials.2013.01.101.
[50] K. Yang, S. Zhang, G. Zhang, X. Sun, S.T. Lee, Z. Liu, Graphene in mice: ultrahigh in vivo tumor uptake and efficient photothermal therapy, Nano Lett. 10 (2010) 3318–3323, https://doi.org/10.1021/nl100996u.
[51] W.Y. Ayen, N. Kumar, In vivo evaluation of doxorubicin-loaded (PEG)3-PLA nanopolymersomes (PolyDoxSome) using DMBA-induced mammary carcinoma rat model and comparison with marketed LipoDoxTM, Pharm. Res. 29 (2012) 2522–2533, https://doi.org/10.1007/s11095-012-0783-8.
[52] J. Van Asperen, O. Van Tellingen, F. Tijssen, A.H. Schinkel, J.H. Beijnen, Increased accumulation of doxorubicin and doxorubicinol in cardiac tissue of mice lacking mdr1a P-glycoprotein, Br. J. Cancer 79 (1999) 108–113, https://doi.org/10.1038/sj.bjc.6690019.
[53] D. Guo, C. Shi, X. Wang, L. Wang, S. Zhang, J. Luo, Riboflavin-containing telodendrimer nanocarriers for efficient doxorubicin delivery: high loading capacity, increased stability, and improved anticancer efficacy, Biomaterials. 141 (2017) 161–175, https://doi.org/10.1016/j.biomaterials.2017.06.041.
[54] K.K. Upadhyay, A.N. Bhatt, A.K. Mishra, B.S. Dwarakanath, S. Jain, C. Schatz, J.-F. Le Meins, A. Farooque, G. Chandraiah, A.K. Jain, A. Misra, S. Lecommandoux, The intracellular drug delivery and anti tumor activity of doxorubicin loaded poly (γ-benzyl l-glutamate)-b-hyaluronan polymersomes, Biomaterials. 31 (2010) 2882–2892, https://doi.org/10.1016/j.biomaterials.2009.12.043.
[55] D.N. Waterhouse, P.G. Tardi, L.D. Mayer, M.B. Bally, A comparison of liposomal formulations of doxorubicin with drug administered in free form, Drug Saf. 24 (2001) 903–920, https://doi.org/10.2165/00002018-200124120-00004.
[56] J.W. Cowens, P.J. Creaven, W.R. Greco, D.E. Brenner, Y. Tung, M. Ostro, F. Pilkiewicz, R. Ginsberg, N. Petrelli, Initial clinical (phase I) trial of TLC D-99 (doxorubicin encapsulated in liposomes), Cancer Res. 53 (1993) 2796–2802.
[57] T. Suzuki, M. Ichihara, K. Hyodo, E. Yamamoto, T. Ishida, H. Kiwada, H. Ishihara, H. Kikuchi, Accelerated blood clearance of PEGylated liposomes containing doxorubicin upon repeated administration to dogs, Int. J. Pharm. 436 (2012) 636–643, https://doi.org/10.1016/j.ijpharm.2012.07.049.

Biomacromolecules

pubs.acs.org/Biomac Article

Reactive Oxygen Species (ROS)-Responsive Polymersomes with Site-Specific Chemotherapeutic Delivery into Tumors via Spacer Design Chemistry

Eliézer Jäger,* Vladimir Sincari, Lindomar J. C. Albuquerque, Alessandro Jäger, Jana Humajova, Jan Kucka, Jan Pankrac, Petr Paral, Tomas Heizer, Olga Janouskova, Rafał Konefał, Ewa Pavlova, Ondrej Sedlacek, Fernando C. Giacomelli, Pavla Pouckova, Ludek Sefc, Petr Stepanek, and Martin Hruby

Cite This: *Biomacromolecules* 2020, 21, 1437−1449 Read Online

ACCESS | Metrics & More | Article Recommendations | Supporting Information

ABSTRACT: The lack of cellular and tissue specificities in conventional chemotherapies along with the generation of a complex tumor microenvironment (TME) limits the dosage of active agents that reaches tumor sites, thereby resulting in ineffective responses and side effects. Therefore, the development of selective TME-responsive nanomedicines is of due relevance toward successful chemotherapies, albeit challenging. In this framework, we have synthesized novel, ready-to-use ROS-responsive amphiphilic block copolymers (BCs) with two different spacer chemistry designs to connect a hydrophobic boronic ester-based ROS sensor to the polymer backbone. Hydrodynamic flow focusing nanoprecipitation microfluidics (MF) was used in the preparation of well-defined ROS-responsive PSs; these were further characterized by a combination of techniques [^{1}H NMR, dynamic light scattering (DLS), static light scattering (SLS), transmission electron microscopy (TEM), and cryogenic TEM (cryo-TEM)]. The reaction with hydrogen peroxide releases an amphiphilic phenol or a hydrophilic carboxylic acid, which affects polymersome (PS) stability and cargo release. Therefore, the importance of the spacer chemistry in BC deprotection and PS stability and cargo release is herein highlighted. We have also evaluated the impact of spacer chemistry on the PS-specific release of the chemotherapeutic drug doxorubicin (DOX) into tumors in vitro and in vivo. We demonstrate that by spacer chemistry design one can enhance the efficacy of DOX treatments (decrease in tumor growth and prolonged animal survival) in mice bearing EL4 T cell lymphoma. Side effects (weight loss and cardiotoxicity) were also reduced compared to free DOX administration, highlighting the potential of the well-defined ROS-responsive PSs as TME-selective nanomedicines. The PSs could also find applications in other environments with high ROS levels, such as chronic inflammations, aging, diabetes, cardiovascular diseases, and obesity.

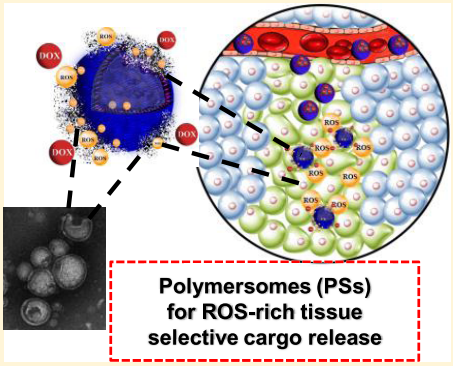

■ INTRODUCTION

The most recent survey by the International Agency for Research on Cancer reported that global deaths related to malignancy were about 9.6 million in 2018 (21% higher than those in 2008).[1,2] This number is predicted to be as high as 19.3 million by 2025,[2] calling for improvements in cancer treatments.[3] In this framework, cancer therapies have been tackled to design nanomedicines that can navigate the body and deliver their cargos at desired tumor sites. Nanomedicines able to fast disassemble in vivo to release their cargo specifically in the tumor microenvironment (TME) [including polymer drug conjugates, polymer micelles, and polymersomes (PSs)] are currently investigated as platforms toward more effective tumor treatments.[4−9] Particularly, PSs made from block copolymers (BCs) are spherical self-assembled nanostructures that resemble the cell membranes of living organisms.[10−12] Nevertheless, compared to biological membranes (such as phospholipids), BC vesicles are easily functionalized and their mechanical properties can be finely tuned.[6,7,11] Moreover, enhanced stability and higher loading capacity have been demonstrated compared to liposomes and micelles.[10−13] These advantages have led to greater interest in recent years toward the development of novel PSs with applications as enzymatic nanoreactors and drug delivery systems, for instance.[6,7,13,14] The PSs are able to encapsulate hydrophobic compounds in the bilayer and hydrophilic drugs in the aqueous lumen,[15,16] and the cargo release can be triggered by external or internal physical or chemical stimuli such as pH, redox potential, light, magnetic field, temperature,

Received: December 18, 2019
Revised: February 20, 2020
Published: February 21, 2020

Downloaded via ACADEMY OF SCIENCES CZECH REPUBLIC on September 16, 2022 at 15:24:14 (UTC).
See https://pubs.acs.org/sharingguidelines for options on how to legitimately share published articles.

ACS Publications © 2020 American Chemical Society

https://dx.doi.org/10.1021/acs.biomac.9b01748
Biomacromolecules 2020, 21, 1437−1449

or the presence of specific enzymes.[13,15,17] The so-called "smart" PSs have been able to release their payloads or show size reduction or charge conversion under the conditions found in tumor microenvironments (reduced pH, hypoxia, tumor-specific enzymes).[15−22] Among the aforementioned stimuli, one can explore the presence of higher levels of reactive oxygen species (ROSs) in tumor sites.[23,24] ROSs, such as hydrogen peroxide (H_2O_2), are a component of the cellular signaling pathways that are necessary for the growth, development, and fitness of living organisms.[25,26] On the other hand, imbalances in H_2O_2 production lead to oxidative stress and inflammatory events that damage tissues and organs, which is correlated with the onset and progression of various diseases, including cancer. Hence, the design of PSs able to respond to these inherent features of TME has been proposed as a promising approach for cancer treatments.[19,27]

Taking into account the abovementioned issues, we have developed a novel platform that allows the specific release of bioactive cargo, such as DOX, in response to ROS levels typically found in TME. Well-defined BCs were synthesized using two different spacer chemistry designs to connect the hydrophobic boronic ester-based ROS sensor to a polymer backbone. The novel materials were further used to prepare oxidative−reductive PSs using the MF technique. The self-assembled structures were characterized by a variety of techniques, and it has been subsequently demonstrated that the employed chemistry plays an important role in BC and PS deprotection rate and in the release of encapsulated double-quenched green bovine serum albumin (DQ-BSA) or DOX. Furthermore, in vitro studies suggest that DOX-loaded ROS-responsive PSs could be efficiently delivered into two different tumor cell lines, providing enhanced biological activity to the antitumor agent. The in vivo biodistribution studies in nude mice bearing EL4 T cell lymphoma demonstrated that the PSs circulate for a longer time and are accumulated to a greater extent compared to the free fluorescent probe. The in vivo investigations also highlight that side effects (such as weight loss and cardiotoxicity) were remarkably reduced using the PS platforms for DOX release and the effectiveness of the treatment (reduction in tumor growth and prolonged animal survival) can be significantly improved using specific boronic acid-based monomeric spacers.

■ EXPERIMENTAL SECTION

Materials. 3-Chloro-1-propanol, NaN_3, 3-azido-1-propanol, *N*-ethyl-*N*′-(3-dimethylaminopropyl)carbodiimide hydrochloride (EDC) triethylamine (TEA), hydrogen peroxide (H_2O_2, 30% w/w solution in H_2O), 4-hydroxymethylphenylboronic acid pinacol ester, 4-aminophenylboronic acid pinacol ester, magnesium sulfate ($MgSO_4$), sodium sulfate (Na_2SO_4), silica gel (70−230 mesh), Sephadex LH-20, 1-hydroxybenzotriazole hydrate (HOBt), ethanolamine, phorbol 12-myristate 13-acetate (PMA), *N*-acetyl-L-cysteine (NAC), and the chain-transfer agent 4-cyano-4-(phenylcarbonothioylthio)pentanoic acid (CTA) were purchased from Sigma-Aldrich and were used as received. Doxorubicin, hydrochloride salt >99% was purchased from LC Laboratories. Double-quenched green bovine serum albumin (DQ-BSA) was purchased from Thermo Fischer Scientific (Czech Republic). Methanol (MeOH), *N*,*N*-dimethylacetamide (DMAc), diethyl ether (Et_2O), 1,4-dioxane, ethanol, tetrahydrofuran (THF), *N*,*N*-dimethyl formamide (DMF), dichloromethane (DCM), toluene, ethyl acetate, petroleum ether, and hexane were purchased from Lachner and dried over molecular sieves (3 Å). Methacryloyl chloride (Sigma-Aldrich) was distilled before use. Deuterated solvents ($CDCL_3$, DMF-d_7, DMSO-d_6, CD_3OD) were purchased from Eurisotop (France). The initiator azobis isobutyronitril (AIBN, Sigma-Aldrich) was recrystallized from methanol prior to use.

Methods. *Synthesis of the Azide-Containing Chain-Transfer Agent (CTA-Azide).* The CTA-Azide was synthesized following the procedure described elsewhere.[28] Briefly, 3-chloro-1-propanol (3.0 g, 31.7 mmol) and NaN_3 (3.5 g, 54.0 mmol) were dissolved in a mixture of acetone (50 mL) and water (5 mL) in a round-bottom flask and refluxed overnight. Acetone was removed under reduced pressure, and 35 mL of water was added to the remaining solution. The product was extracted with diethyl ether (3 × 70 mL), the organic layer was dried over anhydrous Na_2SO_4, and 3-azido-1-propanol was obtained as a colorless oil (1.6 g, 53%) after solvent removal under reduced pressure. The pure product was analyzed by Fourier transform infrared (FTIR) spectroscopy. In the step further, a mixture of CTA-COOH (700 mg, 2.51 mmol), 3-azido-1-propanol (380 mg, 3.76 mmol), and dry DCM (40 mL) was added to a round flask equipped with a magnetic bar and a rubber stopper. The solution was cooled to 0 °C and filled with argon. A solution of EDC (720 mg, 3.76 mmol) and DMAP (50 mg, 0.38 mmol) in DCM (10 mL) was added under an argon atmosphere to react at 0 °C for 2 h and then at room temperature overnight. The reaction mixture was washed with water (100 mL, five times) and dried over anhydrous Na_2SO_4. The DCM was removed under reduced pressure, and the crude product was purified by column chromatography [SiO_2 and hexane/ethyl acetate = 4/1 (v/v)]. The pure product (0.38 g, 42%) was characterized by ^1H NMR and ^{13}C NMR.

^1H NMR (600 MHz, $CDCl_3$, δ): 7.90 (d, 2H, Ar H), 7.56 (t, 1H, Ar H), 7.38 (t, 2H, Ar H), 4.26 (t, 2H, CH_2), 3.61 (t, 2H, CH_2), 2.69 (m, 2H, CH_2), 2.60 (m, 1H, CH_2), 2.43 (m, 1H, CH_2), 2.10 (p, 2H, CH_2), 1.93 (s, 3H, CH_3). ^{13}C NMR ($CDCl_3$, δ): 221.49, 171.52, 144.63, 133.22, 129.13, 128.74, 126.81, 118.60, 61.92, 45.85, 41.26, 33.50, 31.52, 29.87, 24.30.

Synthesis of the Azide-Terminated Poly([N-(2-hydroxypropyl)]-methacrylamide) (PHPMA) MacroCTA. *N*-(2-Hydroxypropyl)-methacrylamide (HPMA) monomer was prepared as previously described.[28] The synthesis of azide-terminated PHPMA macroCTA was performed by reversible addition−fragmentation chain-transfer (RAFT) polymerization. In a Schlenk tube equipped with a magnetic bar, the HPMA monomer (1 g, 7 mmol) was dissolved in 6.62 mL of *tert*-butanol. This solution was filled with argon for 15 min and deoxygenated by three freeze−pump−thaw cycles. The CTA-Azide (118.4 mg, 0.326 mmol) and the initiator AIBN (33.2 mg, 0.204 mmol) were dissolved in 0.736 mL of dimethyl sulfoxide (DMSO), and this solution was added to the Schlenk tube and another freeze−pump−thaw cycle was completed. The tube containing the pink solution was filled with argon again and placed into an oil bath at 70 °C to start the polymerization. After 16 h, the polymerization was quenched by exposing the reaction mixture to air and liquid nitrogen. The polymerization solution was precipitated in a cold mixture of acetone/diethyl ether (v/v = 3/1) followed by a centrifugation step to isolate the product. The product was dissolved in a small amount of methanol, and the azide-terminated PHPMA macroCTA was purified by Sephadex LH-20 using methanol as the mobile phase. The product was precipitated in cold diethyl ether and vacuum-dried to yield a pink solid. The obtained polymer was characterized by size exclusion chromatography (SEC) and ^1H NMR (PHPMA mCTA azide M_n = 3600 g·mol^{-1}, $Đ$ = 1.08).

^1H NMR (600 MHz, MeOD, δ): 7.86 (s, 2H, Ar H), 7.76 (s, 1H, Ar H), 7.67 (s, 2H, Ar H), 7.45 (bp, 1H, NH), 4.20 (s, 2H, CH_2), 3.88 (s, 1H, CH), 3.41 (s, 2H, CH_2), 3.10 (bp, 2H, CH_2), 2.52 (s, 2H, CH_2), 2.15−1.60 (bp, 2H, CH_2), 1.55−0.90 (bp, 3H, CH_3).

Synthesis of the ROS-Responsive Monomers 1 and 2. 4-Aminophenylboronic acid pinacol ester (25 mmol, 5.48 g; for the ROS-responsive monomer 1, M_w = 219.09 g·mol^{-1}) or 4-(hydroxymethyl)phenylboronic acid pinacol ester (25 mmol, 5.85 g; for the ROS-responsive monomer 2, M_w = 234.10 g·mol^{-1}) was dissolved in anhydrous DCM (60 mL) followed by the addition of 30 mmol of TEA (3.05 g). After cooling to 0 °C, 30 mmol (3.23 g) of methacryloyl chloride in ∼5 mL of dried DCM was added dropwise within ∼1 h (temperature not exceeding 0 °C). Then, the reaction

https://dx.doi.org/10.1021/acs.biomac.9b01748
Biomacromolecules 2020, 21, 1437−1449

Table 1. Synthetic Parameters and Molecular Weight Data of the Polymers Prepared via RAFT Polymerization

(Co)polymer code	sample	$[M]_0/[CTA]_0/[I]_0$	time (h)	Conversion (%)[a]	$M_{n,th}$[b] ($g \cdot mol^{-1}$)	$M_{n,SEC}$ ($g \cdot mol^{-1}$)	$M_{n,NMR}$ ($g \cdot mol^{-1}$)	Đ	ϕ[g] (%)
P(HPMA)	$P(HPMA)_{37}$	100/2/1[e]	16	46	7200	3600[c]	5300	1.08[c]	
BC1	$P[(HPMA)_{37}$-*b*-$(ROS\text{-}1)_{31}]$	100/2/1[f]	24	86	30 200	20 300[d]	14 200	1.09[d]	18
BC2	$P[(HPMA)_{37}$-*b*-$(ROS\text{-}2)_{42}]$	100/2/1[f]	24	89	28 700	21 500[d]	18 000	1.13[d]	17

[a]Determined by ^1H NMR in D_2O. [b]Theoretical $M_n = [M]_0/[CTA]_0 \times$ conversion $\times M_{w(monomer)} + MW_{CTA}$. [c]Determined by SEC in MeOH/acetate buffer, pH 6.5, 80/20 vol %. [d]Determined by SEC in DMF using PMMA as the standard. [e]Conditions: *tert*-butanol, $[M]_0$ = 1.5 M, 70 °C. [f]Conditions: 1,4-dioxane/MeOH, 60/40 vol %, [M]0 = 3 M, 70 °C. [g]Weight fraction of the hydrophilic block (SEC).

mixture was warmed to room temperature, stirred for 10 h, and filtered. The filtrate was concentrated on a rotary evaporator, diluted by ethyl acetate, and washed with brine thrice. After drying over $MgSO_4$, the organic solution was concentrated and purified by silica column chromatography using hexane/ethyl acetate (v/v = 2/1) as the eluent. The ROS monomer 1 (M_w = 287.16 $g \cdot mol^{-1}$) was obtained as a colorless crystal with a yield of 80%. The ROS monomer 2 (M_w = 302.17 $g \cdot mol^{-1}$) was obtained as a colorless oil with a yield of 75%. ROS monomers 1 and 2 were characterized by ^1H NMR.

Nitrogen-containing 4-(*N*-methacryloylaminomethyl)-phenylboronic acid pinacol ester monomer—ROS-responsive monomer 1: ^1H NMR (600 MHz, $CDCl_3$, δ): 7.76 (d, *J* = 8 Hz, 2H, Ar H), 7.56 (d, *J* = 8 Hz, 2H, Ar H), 7.53 (s, 1H, NH), 5.78 (s, 1H, $=CH_2$), 5.46 (s, 1H, $=CH_2$), 2.05 (s, 3H, CH_3), 1.33 (s, 12H, CH_3). ^{13}C NMR ($CDCl_3$, δ): 166.66, 141.11, 140.64, 136.03, 124.93, 120.17, 118.92, 83.95, 25.07, 18.95.

Oxygen-containing 4-(*O*-methacryloylaminomethyl)phenylboronic acid pinacol ester monomer—ROS-responsive monomer 2: ^1H NMR (600 MHz, $CDCl_3$, δ): 7.79 (d, *J* = 8 Hz, 2H, Ar H), 7.36 (d, *J* = 8 Hz, 2H, Ar H), 6.14 (s, 1H, $=CH_2$), 5.57 (s, 1H, $=CH_2$), 5.19 (s, 2H, CH_2), 1.95 (s, 3H, CH_3), 1.33 (s, 12H, CH_3). ^{13}C NMR ($CDCl_3$, δ): 167.38, 139.32, 136.38, 135.20, 128.94, 127.36, 126.08, 84.05, 25.06, 18.55.

Synthesis of the Block Copolymers 1 (BC1) and 2 (BC2). In a Schlenk flask equipped with a magnetic bar, PHPMA mCTA azide (100 mg) was dissolved in MeOH (2 mL), and different amounts of the ROS-responsive monomer 1 or ROS-responsive monomer 2 (cf. Table 1) and the initiator AIBN (0.5 $mol \cdot L^{-1}$ related to PHPMA mCTA azide) were dissolved in 1,4-dioxane (4 mL) and added to the Schlenk flask under stirring. The solution was filled with argon, and three freeze−pump−thaw cycles were performed. Afterward, the solution was again filled with argon and placed into an oil bath at 70 °C to start the polymerization. After 24 h, the polymerization was stopped with a quench step using liquid nitrogen. The BCs were obtained after dialysis against deionized water (pH 7.4) for 48 h using a dialysis membrane with MWCO of 3.5−5 kDa. The water was changed every 12 h, and the BCs were recovery by lyophilization. They were further characterized by ^1H NMR and SEC.

BC1: $M_n \approx$ 20.3 kDa, Đ = 1.09; conversion: 86%; ^1H NMR (600 MHz, MeOD, δ): 7.65 (bp, 2H, Ar H), 7.40 (bp, 2H, Ar H; 1H, NH), 3.88 (s, 1H, CH), 3.10 (bp, 2H, CH_2), 2.40−1.60 (bp, 2H, CH_2), 1.50−1.25 (bp, 12H, CH_3), 1.25−0.85 (bp, 3H, CH_3).

BC2: $M_n \approx$ 21.5 kDa, Đ = 1.13; conversion: 89%; ^1H NMR (600 MHz, DMF-d_7, δ): 7.75 (s, 2H, Ar H), 7.35 (s, 2H, Ar H; 1H, NH), 4.90 (bp, 2H, CH_2; 1H, OH), 3.85 (s, 1H, CH), 3.05 (bp, 2H, CH_2), 2.15−1.60 (bp, 2H, CH_2), 1.40−1.20 (bp, 12H, CH_3), 1.15−0.80 (bp, 3H, CH_3).

Size Exclusion Chromatography (SEC). The number-average molecular weight (M_n) and its distribution (Đ) were obtained by SEC. SEC of the isolated copolymers was performed at 25 °C with two PLgel MIXED-C columns (300 mm × 7.5 mm, SDV gel with particle size 5 μm; Polymer Laboratories) and with UV (UVD 305; Watrex, Czech Republic) and RI (RI-101; Shodex, Japan) detectors. DMF was used as the mobile phase at a flow rate of 1 $mL \cdot min^{-1}$. The molecular weight values were calculated using the Clarity software (DataApex, Czech Republic). Calibration with PMMA standards was used. The M_n and its distribution (Đ) for PHPMA macroCTA were determined on a HPLC Shimadzu system equipped with a Superose 12 column, UV, Optilab rEX differential refractometer, and multiangle light scattering DAWN 8 (Wyatt Technology) detectors. These experiments used a 0.3 M sodium acetate buffer/MeOH (pH 6.5, 80:20) containing 0.5 $g \cdot L^{-1}$ sodium azide as the mobile phase.

^1H NMR and ^{13}C NMR Spectra. ^1H NMR spectra of the monomers (300 or 600 MHz) were recorded using a Bruker Avance DPX 300 MHz NMR spectrometer or Bruker 600 MHz NMR spectrometer (for ^{13}C NMR only) with $CDCl_3$ or DMF-d_7 as solvents at 25 and 37 °C in deuterated PBS/DMF-d_7 for polymer deprotection studies (described hereafter). The chemical shifts are relative to TMS using hexamethyldisiloxane (HMDSO, 0.05 for ^1H NMR and 2.0 ppm for ^{13}C NMR) as the internal standard. Chemical shifts, δ, are in units of parts per million (ppm).

^1H NMR Measurements of the Polymersome Deprotection. BCs (2 mg) were loaded separately into 50 μL of DMF-d_7, followed by the addition of 550 μL of deuterated phosphate-buffered saline (PBS, pH 7.4). The solution was transferred to a NMR tube and incubated at 37 °C. To the solution, 0.6 μL of H_2O_2 was added to make a 10 mM or 1 mM H_2O_2 solution (H_2O_2 previously diluted). The BCs incubated at 37 °C in deuterated PBS (550 μL) and 50 μL of DMF-d_7 were used as the control.

Dynamic Light Scattering (DLS). The DLS measurements were performed using an ALV CGE laser goniometer consisting of a 22 mW HeNe linear polarized laser operating at a wavelength λ = 632.8 nm, an ALV 6010 correlator, and a pair of avalanche photodiodes operating in the pseudo-cross-correlation mode. The samples were loaded into 10 mm diameter glass cells and maintained at 25 ± 1 °C. The data were collected using the ALV Correlator Control software, and the counting time was 30 s. To avoid multiple light scattering, the samples were diluted 100 times before the measurements. The intensity correlation functions $g_2(t)$ were analyzed using the algorithm REPES (incorporated in the GENDIST program), resulting in the distributions of relaxation times shown in the equal-area representation as $\tau A(\tau)$. The mean relaxation time or relaxation frequency ($\Gamma = \tau^{-1}$) is related to the diffusion coefficient (D) of the polymersomes as $D = \Gamma/q^2$, where $q = (4\pi n \sin(\theta/2))/\lambda$ is the scattering vector with n being the refractive index of the solvent and θ the scattering angle. The hydrodynamic radius (R_H) or the distributions of R_H were calculated using the well-known Stokes−Einstein relation

$$R_H = (k_B T)/6\pi n D \quad (1)$$

where k_B is the Boltzmann constant, T is the absolute temperature, and η is the viscosity of the solvent.

Static Light Scattering (SLS). In the SLS mode, the scattering angle was varied from 30° to 150° with a 10° stepwise increase. The absolute light scattering is related to the weight-average molar mass [$M_{w(PSs)}$] and the radius of gyration (R_G) of the polymersomes by the Zimm formalism, represented as

$$Kc/R_\theta = 1/M_w(1 + R_G^2 q^2/3) \quad (2)$$

where K is the optical constant, which includes the square of the refractive index increment (dn/dc); R_θ is the excess normalized scattered intensity (toluene was used as the standard solvent); and c is the polymer concentration given in $mg \cdot mL^{-1}$. The refractive index increment (dn/dc) of the PSs in pure water was determined using a

https://dx.doi.org/10.1021/acs.biomac.9b01748
Biomacromolecules 2020, 21, 1437−1449

Brice−Phoenix differential refractometer operating at λ = 632.8 nm (0.180 and 0.173 mL/g for PS1 and PS2, respectively).

Electrophoretic Light Scattering (ELS). The ELS measurements, performed using a Zetasizer NanoZS instrument (Malvern Instruments, U.K.), were employed to determine the average zeta potential (ζ) of the PSs. The equipment measures the electrophoretic mobility (U_E) and converts the value into ζ-potential (mV) through Henry's equation. Henry's function was calculated through the Smoluchowski approximation.

Transmission Electron Microscopy (TEM) and Cryogenic Transmission Electron Microscopy (Cryo-TEM). TEM observations were performed on a Tecnai G2 Spirit Twin 120 kV (FEI, Czech Republic) using a bright-field imaging mode at an accelerating voltage of 120 kV. The polymersomes (4 μL) were dropped onto a copper TEM grid (300 mesh), which was coated with a thin, electron-transparent carbon film. The excess of the solution was removed by touching the bottom of the grid with a filtering paper. This fast removal of the solution was performed after 5 min of sedimentation to minimize oversaturation during the drying process. Afterward, the samples were negatively stained with uranyl acetate (2 μL of 1 wt % solution dropped onto the dried polymersomes and removed after 30 s, as described above). The samples were left to dry at room temperature and then observed in the TEM microscope. Under these conditions, the micrographs displayed a negatively stained background with bright polymersomes. The image analysis was performed using the Image J software. The polymersomes were also imaged by cryo-TEM, where 4 μL of the sample solution was loaded into an electron microscopy grid covered with a holey or lacey carbon supporting film (Electron Microscopy Science), which was hydrophilized just before the experiment via glow discharge (Expanded Plasma Cleaner, Harrick Plasma). The excess of the solution was removed by blotting (Whatman no. 1 filter paper) for ∼1 s, and the grid was plunged into liquid ethane held at −182 °C. The vitrified sample was then immediately transferred into the microscope and observed at −173 °C at an accelerating voltage of 120 kV.

Polymersome Production by Microfluidics. The PSs were produced after testing different polymer concentrations, organic solvents, and flow rates of the organic and aqueous phases according to the method previously described.[28] Briefly, BC1 and BC2 were dissolved in THF/MeOH (80/20) (v/v) to produce a final concentration of 5.0 mg·mL^{-1}. Polymersomes were produced using the microfluidic device setup from Dolomite (Royston, United Kingdom) equipped with a glass Micromixer chip with 12 mixing-stage microchannels of 50 μm × 125 μm (depth × width). The polymer solution was pumped through the middle channel and PBS through the side channels using two independent Dolomite Mitos P-Pumps (Royston, United Kingdom) controlled via PC software. For the production of DOX-loaded PS, the drug (1 mg·mL^{-1}) was dissolved in PBS. All solutions were previously filtrated (0.22 μm). The flow rates were 200 μL·mL^{-1} for the water phase and 100 μL·mL^{-1} for the organic phase, resulting in a flow rate ratio of 2:1. The polymer colloids were collected in vials and dialyzed against PBS for 12 h to remove the organic solvent and unloaded DOX. They were further characterized by DLS, SLS, ELS, and TEM. DOX was determined by UV−vis using an analytical curve with a linear response in the range of 0.001−0.5 mg·mL^{-1}. DOX loading content (LC) and DOX loading efficiency (LE) were calculated using the standard equations

$$\text{LC (\%)} = (\text{DOX ammount in PSs})/(\text{mass of PSs}) \times 100 \quad (3)$$

$$\text{LE (\%)} = (\text{DOX ammount in PSs})/(\text{DOX feeding}) \times 100 \quad (4)$$

The quantifications were always performed in triplicate, and the mean values are reported throughout the article.

The Cy7-PS1 and Cy7-PS2 conjugates containing the Cy7 fluorescent dye were also produced by microfluidics. First, the coupling between the fluorescent dye Cyanine 7-DBCO (Cy7) and the azide-terminated BC1 and BC2 was performed using an adapted procedure as described elsewhere.[28] Briefly, in an amber glass vial, 30 mg of the BCs was dissolved in 1 mL of DMF under stirring. The fluorescent dye (Cyanine 7-DBCO) was added in the molarity 5:1 (fluorescent dye:azide-terminated group) and kept reacting overnight in the dark. Afterward, the solution was dialyzed in a Float-A-Lyzer (3.5−5 kDa) against water for 24 h to remove the free dye and organic solvent. The Cy7-BC1 and Cy7-BC2 conjugates were recovered by lyophilization with a yield of ∼60%. For the production of the Cy7-PSs, the BC powder was mixed 1:1 weight ratio (BC1/Cy7-BC1 and BC2/Cy7-BC2), and the mixtures were dissolved in THF/MeOH (80/20 v/v) to produce final concentrations of 5.0 mg·mL^{-1}. The chemical structure of the Cy7-BC2 conjugate is shown in the Supporting Information. The PSs were produced as mentioned before, and the amount of Cy7 fluorescent dye was measured by fluorescence spectroscopy (750/780 nm, Ex/Em) and adjusted to 30 μg·mL^{-1} for both PSs.

In Vitro Drug Release. The in vitro DOX release was investigated in PBS and PBS with 1 mM H_2O_2 at 37 °C using the dialysis method. A preswollen cellulose dialysis membrane tube with MWCO 3.5−5 kDa (Spectra-Por Float-A-Lyzer G2) was filled with 2.0 mL of DOX-loaded PSs at 0.5 mg·mL^{-1}. The membrane tube was then immerged into 3 L of PBS at 37 °C and 350 rpm. At predetermined times, 10 μL of the DOX-loaded PSs was removed and diluted into 90 μL of MeOH for the determination of the remaining DOX. The DOX amount was quantified by UV−vis at λ = 480 nm.

Cell Culture. The T-lymphocyte-derived human cell line Jurkat (LGC standard, Poland) was cultured in RPMI-1640 medium supplemented with 100 units of penicillin and 100 μg·mL^{-1} streptomycin (Thermo Fischer Scientific, Czech Republic) with fetal bovine serum. The T-lymphocyte murine cell line EL4 (LGC standard, Poland) was cultured in Dulbecco's modified Eagle's medium (DMEM) supplemented with 100 units of penicillin and 100 μg·mL^{-1} streptomycin (Thermo Fischer Scientific, Czech Republic). Both cell cultures were incubated and cultivated in a humidified incubator at 37 °C with 5% CO_2 in 25 cm^2 flasks.

Cellular Uptake. Both cell lines were plated into 24-well plates at density 1 × 10^5 cells per well the day before incubation with PSs. PSs were incubated with cells for 2 h in 5% CO_2 at 37 °C. The amount of DOX-loaded PSs was normalized to DOX content (10 μg·mL^{-1}). After the incubation time, the cells were centrifuged (1500 rpm) and washed two times with 0.5 mL of PBS containing 0.5% BSA. The cells were then resuspended in PBS/BSA and analyzed by flow cytometry using a FACS Verse (Becton Dickinson) (1 × 10^4 events per sample) apparatus. The data were processed using the FlowJo software V7.6.1. The median of the fluorescence intensity was determined, and the signal of negative cells was subtracted to calculate the relative uptake (DOX median of fluorescence was assigned as 100%). Only untreated cells and cells incubated with DOX were used as the controls. All samples were measured in duplicate in four independent experiments.

Cell Viability Assays. Cell viability assays were conducted using the Alamar Blue cell viability reagent (Thermo Fischer Scientific, Czech Republic) according to the manufacturer's protocol. Cells were seeded in 100 μL of media into 96-well plates 24 h prior to treatment at a density of 1 × 10^4 cells per well. Serial dilutions of PSs and DOX were added to the medium (10 μL). The cells were subsequently incubated for 72 h in 5% CO_2 at 37 °C. After the incubation time, 10 μL of the Alamar Blue reagent was added to each well and incubated for 4 h in 5% CO_2 at 37 °C. Resorufin, which is reduced from resazurin, is the active compound of the Alamar Blue reagent. Resorufin is highly fluorescent only in viable cells, and its intensity was measured using a Synergy Neo plate reader (Bio-Tek, Prague, Czech Republic) at 570 nm/600 nm (Ex/Em). DOX-free PSs (concentrations from 0.1625 up to 100 μg·mL^{-1}), untreated cells, and cells incubated with free DOX were used as the controls. All samples were measured in triplicate in three independent experiments.

DQ-BSA Assay. To determine the intracellular degradation of the polymersomes, EL4 cells were plated into 96-well plates at a density of 3 × 10^4 cells per well the day before incubation with PSs. DQ-BSA-loaded PSs (1 mg·mL^{-1}; DQ-BSA adjusted to 50 μg·mL^{-1} by UV−vis) were incubated with cells for 2 h in 5% CO_2 at 37 °C. For PMA-treated cells, PMA was added (100 nM) 1 h after the 2 h incubation

https://dx.doi.org/10.1021/acs.biomac.9b01748
Biomacromolecules 2020, 21, 1437−1449

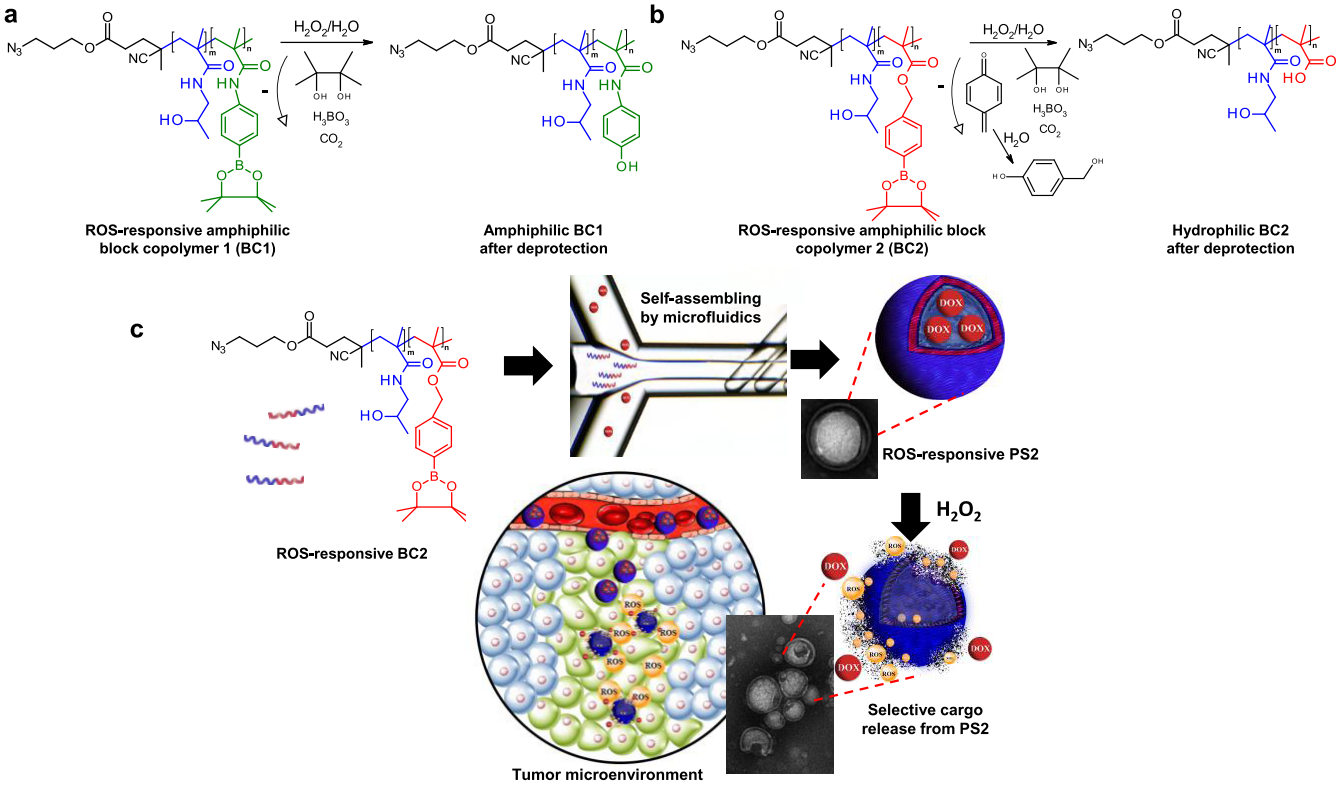

Figure 1. Spacer-design-chemistry-envisaged (a) BC1 and (b) BC2 and their respective mechanisms of ROS-triggered deprotection by H_2O_2. PHPMA is shown in blue, the nitrogen-containing boronic spacer ("amphiphilic", partially hydrophilic, BC1) in green, and the oxygen-containing boronic spacer (fully hydrophilic, BC2) in red. (c) Microfluidics manufacturing of DOX-loaded PS2 from BC2 and the ROS deprotection under H_2O_2. Cargo chemotherapeutic DOX release is shown in red.

time (aforementioned). For NAC-treated cells, NAC was added (3 mM) at the same time as the DQ-BSA-loaded PSs and 1 h after PMA (100 nM) was added. After the incubation time, the cells were resuspended with 0.5 mL of PBS containing 0.5% BSA and analyzed by flow cytometry using a BD FACS Aria II (Becton Dickinson) (1×10^4 events per sample). The data were processed using the FlowJo software v 7.6.1. The median of the fluorescence intensity was determined, and the signals of negative cells were subtracted for the calculation of DQ-BSA intracellular degradation. All samples were measured in duplicate.

In Vivo Biological Studies. The animal experiments described in this study were performed in accordance with the corresponding legislation in the Act on Experimental Work with Animals (act no. 246/1992 of the Czech Republic and decrees no. 419/2012), which is fully compatible with the corresponding European Union directives. For the antitumor effect of the PSs, healthy inbred C57BL/6J mice (females, 8 weeks old, obtained from AnLab, Ltd., Prague, Czech Republic) were used. After the mice were shaved, EL4 lymphoma carcinoma cells (1×10^5 cells in PBS) were injected subcutaneously into the right flank. When the tumors reached a diameter of 4−5 mm, the animals were randomly divided into four groups ($n = 8$). Subsequently, the first group received PBS (named the saline group) intravenously into the tail vein. Injection was repeated on days 4 and 8 from the first application (day 0). The second group received the DOX-free formulation [5 mg DOX (equiv)/kg dissolved in PBS on the same days, and the third and fourth groups received, respectively, DOX-loaded PS1 and PS2 formulations (100 μg of DOX in 5 mg of PSs in 250 μL)]. Subsequently, the survival of all animals was monitored for 40 days and the tumor volume was measured twice a week using eq 5, where a is the length and b is the width of the tumor.

$$V = (a \times b^2 \times \pi)/6 \quad (5)$$

Biodistribution Studies. The biodistribution of Cy7-PS1, Cy7-PS2, and free Cy7 was determined by fluorescence intensity in athymic nude mice 0, 4, 8, 24, 48, 96, and 144 h after intravenous injection (mice injected with 250 μL of PSs containing 30 μg of Cy7/mL; PSs ∼ 10 mg). Fluorescence was detected using the Xtreme In Vivo Imaging System (Bruker, Germany). For fluorescence imaging, the excitation filter 750 nm and the emission filter 830 nm were used. During the measurements, mice were anesthetized using 2% isoflurane (Aerrane, Baxter, U.K.). The greyscale adjustments and quantification of the fluorescence intensity were performed using open-source image processing software Fiji. Regions of interest (ROIs) were selected based on tumor boundaries visible in reflectance, and the mean fluorescence intensity in the tumors was calculated as fluorescence intensity in ROI divided by the area of ROI. Mice were sacrificed 144 h after administration of polymersomes, and the fluorescence intensity was measured in the tumor, heart, intestine, kidneys, liver, lungs, and spleen. The signals were normalized by the weight of the organs.

Peripheral Blood Collection. Peripheral blood was collected with capillaries containing ∼2 μL of 0.5 mol·L^{-1} ethylenediaminetetraacetate (EDTA) solution (Sigma-Aldrich, Czech Republic) from the retro orbital sinus of anaesthetized animals (using inhalation anesthesia with 3% isoflurane). The first blood samples were taken before EL4 cell application and the subsequent blood samples in the following 7 day intervals. The blood samples were analyzed with a BV5300 veterinary haemoanalyzer (Mindray, China) and using flow cytometry.

Determination of Creatine Kinase Levels. Blood samples were collected from the retro orbital plexus under inhalation anesthesia using 3% isoflurane into nonheparinized capillary tubes on day 10 after the third injection of free DOX, PS1, PS2, and saline groups. Plasma was separated by centrifugation at 4000 rpm and 4 °C and further stored at −80 °C until analysis. Creatine phosphokinase enzyme activity levels were quantified using a commercially available kit, Creatine Kinase Activity Assay Kit (Sigma-Aldrich, Czech Republic), based on the protocol described by the manufacturer.

https://dx.doi.org/10.1021/acs.biomac.9b01748
Biomacromolecules 2020, 21, 1437−1449

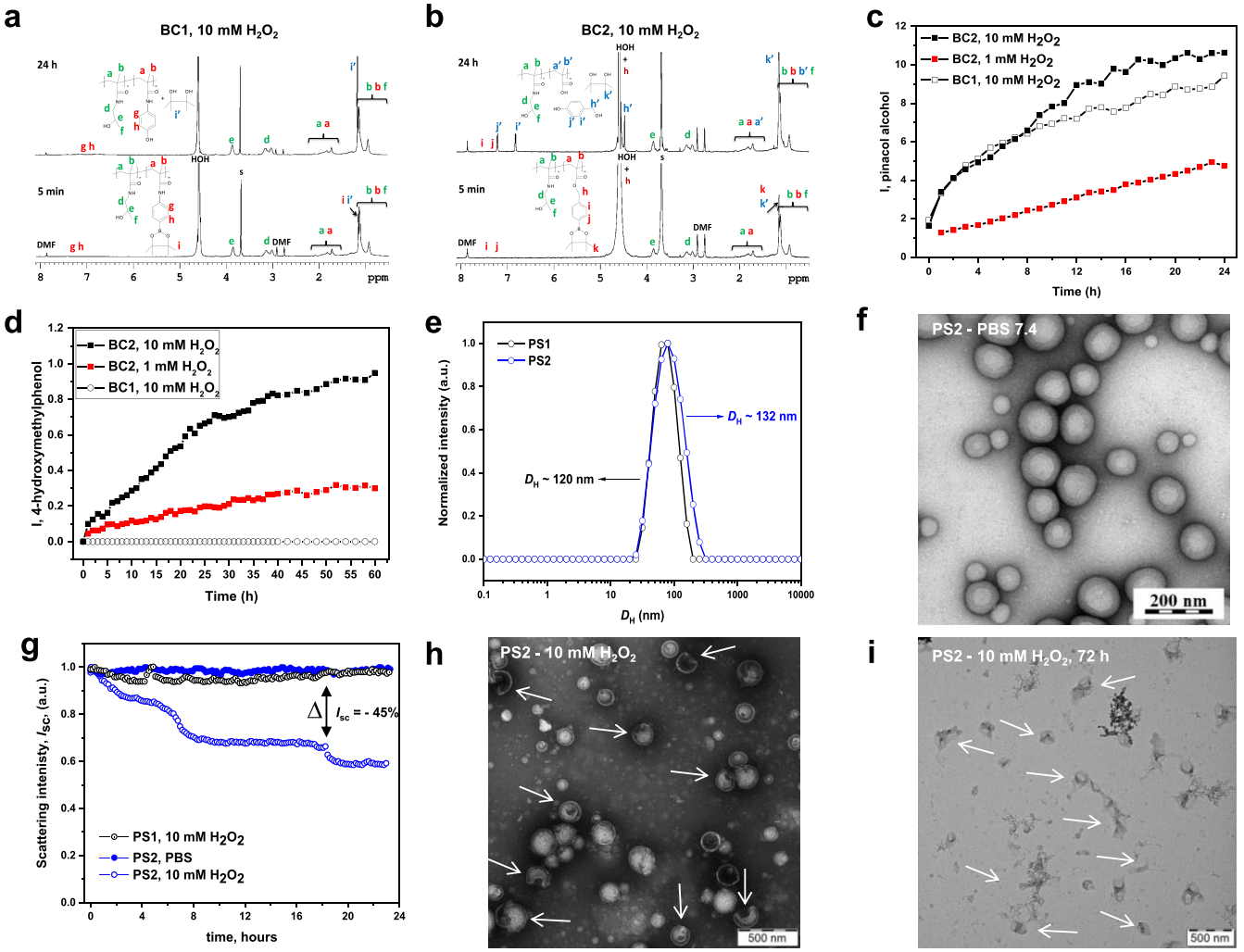

Figure 2. ^{1}H NMR spectra of (a) BC1 and (b) BC2 deprotection after 5 min (bottom) and 24 h (top) of incubation in 10 mM H_2O_2 in DMF-d_7, deuterium PBS. (c) ^{1}H NMR integral intensities related to the deprotection of the pinacol ester-protected boronic groups and the appearance of pinacol alcohol, a product of the degradation, along 24 h of incubation of BC1 in 10 mM H_2O_2 (open black circles) and BC2 in 1 mM (solid red squares) or 10 mM (solid black squares) H_2O_2. (d) ^{1}H NMR integral intensities related to the appearance of 4-hydroxymethyl phenol, a product of degradation of BC2, during 60 h of incubation in 1 mM (solid red squares) or 10 mM (solid black squares) H_2O_2 and BC1 during 60 h of incubation in 10 mM H_2O_2 (open black circles). (e) Distributions of diameters for PS1 (open black circles) and PS2 (open blue circles) in PBS (pH 7.4) and (f) TEM micrographs of PS2 upon incubation in PBS pH 7.4. (g) Changes in light scattering intensity (I_{sc}) after incubation of PS2 in PBS (pH 7.4) (solid blue circles) and 10 mM H_2O_2 (open blue circles) and PS1 (open black circles) at 37 °C during 24 h. TEM micrographs of PS2 after (h) 24 h and (i) 72 h of incubation in 10 mM H_2O_2 (arrows depict the deprotected or disassembled PS2).

Statistical Analysis. The two-way analysis of variance (ANOVA) test was applied to identify statistical differences among groups. Survival curves were generated using the Kaplan−Meier method. Analyses were performed with GraphPad Prism 6 software (GraphPad Inc, United States), and $P < 0.05$ was considered statistically significant.

■ RESULTS AND DISCUSSION

Synthesis of the ROS-Responsive Building Blocks. The ROS-responsive BC backbones were envisaged based on pinacol-type boronic ester-protecting groups (Figure 1a, green and Figure 1b, red and Figure S1). Among the oxidative-responsive moieties, boronic acids and boronic esters undergo oxidation-triggered hydrolysis in the presence of biologically relevant levels of H_2O_2, thereby making these compounds candidates for ROS-induced polymer decomposition. The pinacol-type boronic ester groups have been shown to be the most ROS-selective and sensitive probes to respond to H_2O_2 at physiological concentrations with high specificity.[29−32] At physiologically relevant H_2O_2 concentrations (100 μM to 1 mM of H_2O_2),[31,33,34] benzylic-based boronic esters are oxidized to phenols, which then undergo a quinone methide rearrangement, leading to a strong hydrophilization of the polymer block (discussed hereafter) and subsequent PS disassembly and cargo release (Figure 1c).

Accordingly, under the envisaged targeted site-specific ROS-rich environment, derivative benzylic esters can undergo complete self-immolative deprotection, resulting in a hydrophilic polymer after the reaction, while partial deprotection occurs in the aniline derivative, resulting in a relatively less hydrophilic polymer containing phenols (Figure 1a,b). The polymer poly([*N*-(2-hydroxypropyl)]methacrylamide) (PHPMA) (Figure 1a, blue) was chosen as the hydrophilic segment due to its stealth property and biocompatibility. The polymer block PHPMA bearing azide functional groups was synthesized using the HPMA monomer and a modified chain-

https://dx.doi.org/10.1021/acs.biomac.9b01748
Biomacromolecules 2020, 21, 1437−1449

Table 2. Structural Features of the Manufactured PSs as Determined by Light Scattering Measurements

PSs	R_H (nm)[a] diameter = $2R_H$	PDI[a]	ζ[b] (mV)	R_G[c] (nm)	$\rho^c = R_G/R_H$	M_W[c] PS × 10^7 (g·mol^{-1})	N_{Agg}[c,d]
PS1	60.0	0.09	−8.4	65	1.1	5.45	2460
PS2	65.0	0.10	−8.9	64	1.0	6.06	2450
DOX-PS1	62.5	0.15	−8.5				
DOX-PS2	68.0	0.18	−8.2				
PS1, 10 mM H_2O_2	63.0	0.10	−15.4	50	0.8	5.29	2388
PS2, 10 mM H_2O_2	62.0	0.08	−23.4	56	0.9	3.12	1280

[a]Dynamic light scattering. [b]Electrophoretic light scattering. [c]Static light scattering. [d]Weight-average molecular weight (M_w) of the BC.

transfer agent (CTA) by the reversible addition−fragmentation chain-transfer (RAFT) polymerization, and it was used as a macro chain-transfer agent (PHPMA mCTA azide, M_n = 3.6 kDa, $Đ$ = 1.08; Figures S1a, S2, and Table 1). The introduction of the clickable azide group to the end of the PHPMA BCs allows further PS functionalization with fluorescent dyes or antibodies for imaging and selective targeting, for instance. Subsequently, the 4-aminophenylboronic acid pinacol ester (compound 1, Figure S3) was reacted with methacryloyl chloride to generate the methacrylamide pinacol ester-protected ROS monomer 1 (Figures S1b and S3). 4-(Hydroxymethyl)phenylboronic acid pinacol ester (compound 2, Figure S3) was methacryloylated to generate the methacrylate pinacol ester-protected ROS monomer 2 (Figures S1c and S3). The ROS methacrylic monomers were further polymerized using the PHPMA mCTA azide to generate the ROS-responsive amphiphilic BC1 (Figures 1a and S1b) and ROS-responsive amphiphilic BC2 (Figures 1b and S1c). The BCs were successfully synthesized by RAFT polymerization with similar M_w and desired polydispersity (Table 1).

We targeted the synthesis of BCs with the appropriate hydrophilic/hydrophobic weight ratio (ϕ = the weight fraction of the hydrophilic block at the BCs of 10−40%)[16,28] (Table 1), aiming at the preparation of PSs to enable the DOX solubilization in their aqueous lumen. Successful BC synthesis was confirmed by ^{1}H NMR (Figure S4) and size exclusion chromatography (SEC) analysis (Figure S5). The M_n of BC1 is ∼20.3 kDa with low dispersity of $Đ$ ∼ 1.09, and these values are M_n ∼ 21.5 kDa and $Đ$ ∼ 1.13 for BC2 as determined by SEC (Table 1 and Figure S5). The characteristic proton signals corresponding to the repeating units of the monomers are assigned in the ^{1}H NMR spectra given in Figure S4.

Deprotection of the ROS-Responsive Building Blocks. The deprotection of the BCs was followed by ^{1}H NMR in 1 and 10 mM H_2O_2 environments in DMF-d_7/PBS (pH 7.4).[31,33,34] Figure 2 shows high-resolution ^{1}H NMR spectra of BCs recorded from 5 min to 24 h after the addition of 1 or 10 mM H_2O_2. The spectra portrayed in Figure 2a,b (5 min, bottom) evidence weak and broad signals from the hydrophobic block and strong signals from the hydrophilic PHPMA block for both BC1 (Figure 2a) and BC2 (Figure 2b) prior to H_2O_2 addition. These results demonstrate that the protons corresponding to the hydrophobic block are restricted in mobility (not observed in spectra), whereas the protons of the PHPMA block corresponding to the hydrophilic segment of the BCs are visible. Nevertheless, different behaviors after H_2O_2 addition were observed for BC1 (Figure 2a, top) and BC2 (Figure 2b, top). The aryl boronic ester groups of BC1 are oxidized and subsequently hydrolyzed, evidencing the stable intermediate 4-amino-phenol that does not undergo quinone methide rearrangement. On the other hand, for BC2, the aryl boronic ester groups are oxidized and hydrolyzed with the intermediate phenol in water quickly turning into 4-(hydroxymethyl)phenol (Figures 1b and 2b). The ^{1}H NMR spectra evidence that the side chains of the BCs are fully deprotected after 24 h (BC1, Figures 2a and S6; BC2, Figures 2b and S7) in the 10 mM H_2O_2 environment. The deprotection is time- and H_2O_2-concentration-dependent, as evidenced by the course of the pinacol alcohol appearance (Figure 2c), a product of deprotection of the pinacol ester-protected boronic groups. For BC2 (Figure 2b, top), it is clearly observed that the broad peaks in the ^{1}H NMR spectrum related to the BC are replaced by the sharp peaks of the low-molecular-weight side groups, demonstrating the subsequent self-immolative reaction triggered by H_2O_2. The self-immolative reaction proceeds more extensively by increasing incubation time or H_2O_2 concentration, as observed by evaluating the time-dependent ^{1}H NMR integral intensities of the appearance of the 4-(hydroxymethyl)phenol group (Figure 2d). The former group is a product of the quinone methide rearrangement on the benzylic group that takes place only in BC2 (Figures 1b, 2d, S6, and S7). This step of deprotection is slower, and after 60 h (in 10 mM H_2O_2), ∼53% of BC2 underwent the self-immolative reaction (Figure 2d, black squares and Figure S7b). The spectra recorded in solvents suitable for both blocks were also compared (MeOD, DMF-d_7, cf. the Supporting Information, Figure S4).

We further evaluated the H_2O_2 scavenging ability of the BCs. In the experiment, 1 mg of BC1 and BC2 was added to 1 mL of different H_2O_2 concentrations (200 and 100 μM) and after 3 h of incubation, the concentration of H_2O_2 in the supernatants was determined by the Amplex Red Hydrogen Peroxide/Peroxidase Assay.[35] Figure S8 evidences that both BCs are reactive to H_2O_2 to similar extent [poly(lactic) acid-*block*-poly(ethylene) oxide (PLA-*b*-PEO) was used as a control]. The similar ability of both BCs to react with H_2O_2 is probably due to the similar amounts of pinacol-protected boronic groups (Table 1). We highlight that both BCs respond to pathophysiological relevant levels of H_2O_2 ($\lesssim$1 mM).[26,33]

Characterization of the ROS-Responsive Polymersomes. Block copolymers containing hydrophilic PHPMA and the hydrophobic boronic-based monomer in a given weight ratio and with desired molecular weight can generate self-assembled PSs in aqueous solution.[10,16,28] The manufacturing of the self-assemblies has been conducted using the microfluidic technique.[28] Spherical and uniform PSs were obtained from both BCs after dialysis, and they were detailedly characterized by dynamic (DLS), static (SLS), and electrophoretic (ELS) light scattering; transmission electron microscopy (TEM); and cryogenic TEM (cryo-TEM). The size distribution is monomodal with average diameter D_H ∼ 120 nm (PDI = 0.09) for PS1 (Figure 2e, black circles) and D_H ∼ 132 nm (PDI = 0.10) for PS2 (Figure 2e, blue circles) after 24

https://dx.doi.org/10.1021/acs.biomac.9b01748
Biomacromolecules 2020, 21, 1437−1449

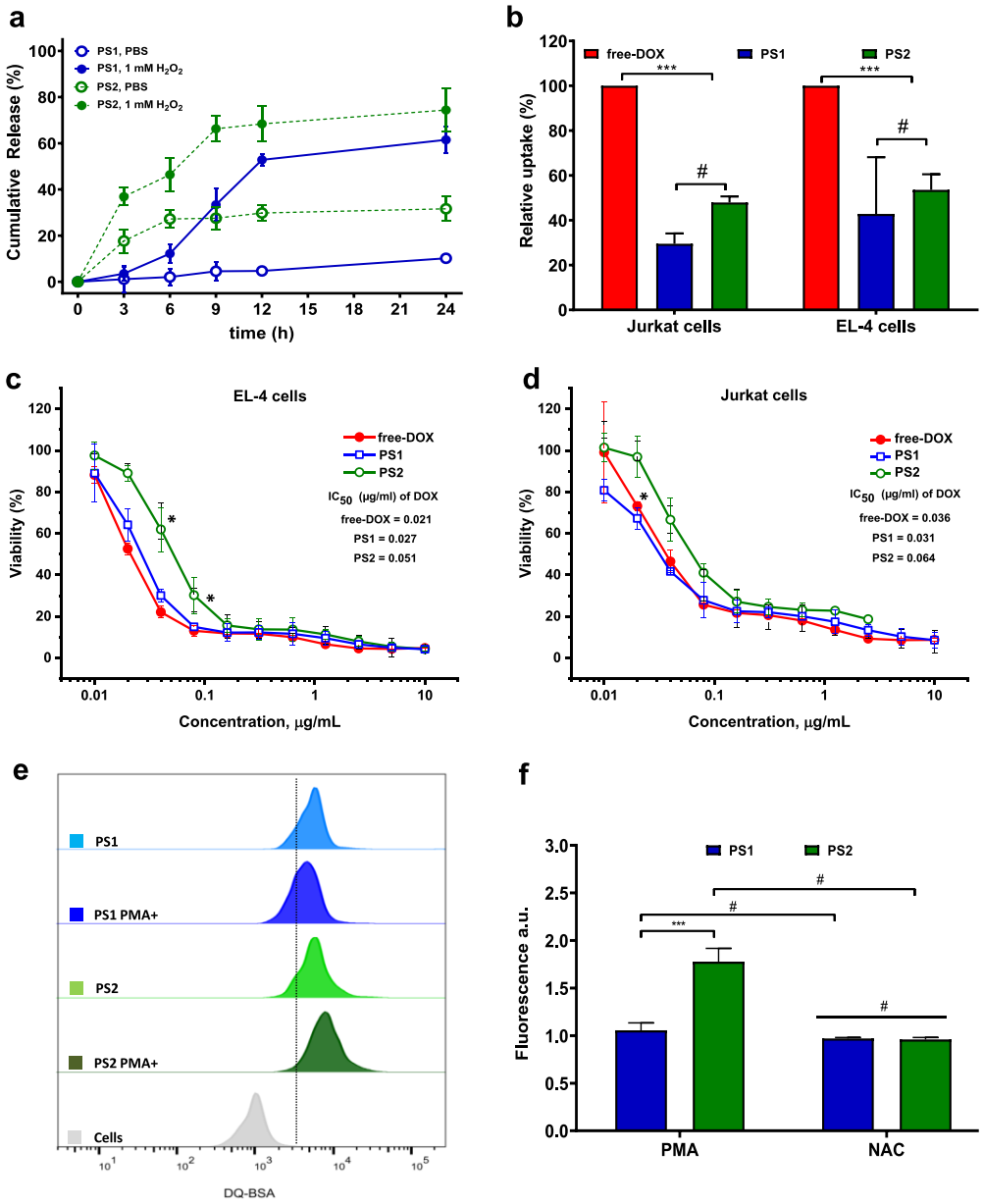

Figure 3. (a) Doxorubicin cumulative release in PBS buffer (pH 7.4) (open blue circles, PS1; open green circles, PS2) and in 1 mM H_2O_2 (solid blue circles, PS1; solid green circles, PS2) over 24 h (n = 2). (b) PSs and free DOX cellular uptake by Jurkat and EL4 tumor cell lines after 2 h incubation time (n = 4). Cell viability of (c) EL4 and (d) Jurkat cell lines after 72 h incubation time with different concentrations of free DOX (red circles) and DOX-loaded PS1 (blue squares) and DOX-loaded PS2 (green circles) (n = 4). (e) Flow cytometry analysis of EL4 cells preincubated with PSs containing double-quenched bovine serum albumin (DQ-BSA) in the absence and presence of PMA (100 nM). (f) DQ-BSA release from PS1 and PS2 in the presence of PMA (100 nM; ROS inducer) and in the presence of NAC (3 mM; ROS scavenger). Data are the ratio between cells treated and untreated with PMA or NAC (+PMA) (n = 2). *$p < 0.05$; ***$p < 0.001$; #, nonsignificant.

h in PBS. The DOX loading leads to a gentle increase in the diameter (~5−10 nm) and polydispersity (~0.18) of PS2 (Table 2), although not affecting its stability and applicability.

The combination of DLS and SLS data (Figure S9) provides important information regarding the structural features of the assemblies. The ratio R_G/R_H ~ 1.0 (Table 2) is the characteristic of hollow spheres (vesicles).[28,36] The high numbers for N_{Agg} are also expected for the vesicular morphology.[28,37] The size and morphology were confirmed by the TEM images portrayed in Figure 2f (PS2) and Figure S10a (PS1), where spherical and homogeneous PSs are observed.

Subsequently, the PS stability was evaluated under relevant H_2O_2 concentration (10 mM H_2O_2) as a function of time to demonstrate the ROS responsiveness.[31,33,34,38] The PSs are stable without changes in particle size during 24 h of incubation in PBS at pH 7.4 (Figure 2e); nevertheless, polymer deprotection and particle damage are observed after incubation with H_2O_2. For PS2, the scattering intensity (I_{sc}) drops almost 2-fold (Figure 2g, blue open circles) compared with I_{sc} in PBS (Figure 2g, blue filled circles) and PS1 in 10 mM H_2O_2 (Figure 2g, open black circles). The more negative surface charge (ζ-potential) after H_2O_2 incubation also suggests the deprotection of PS2 to the final carboxyl groups (Figure 1b and Table 2). The DLS data agree with ^{1}H NMR

https://dx.doi.org/10.1021/acs.biomac.9b01748
Biomacromolecules 2020, 21, 1437−1449

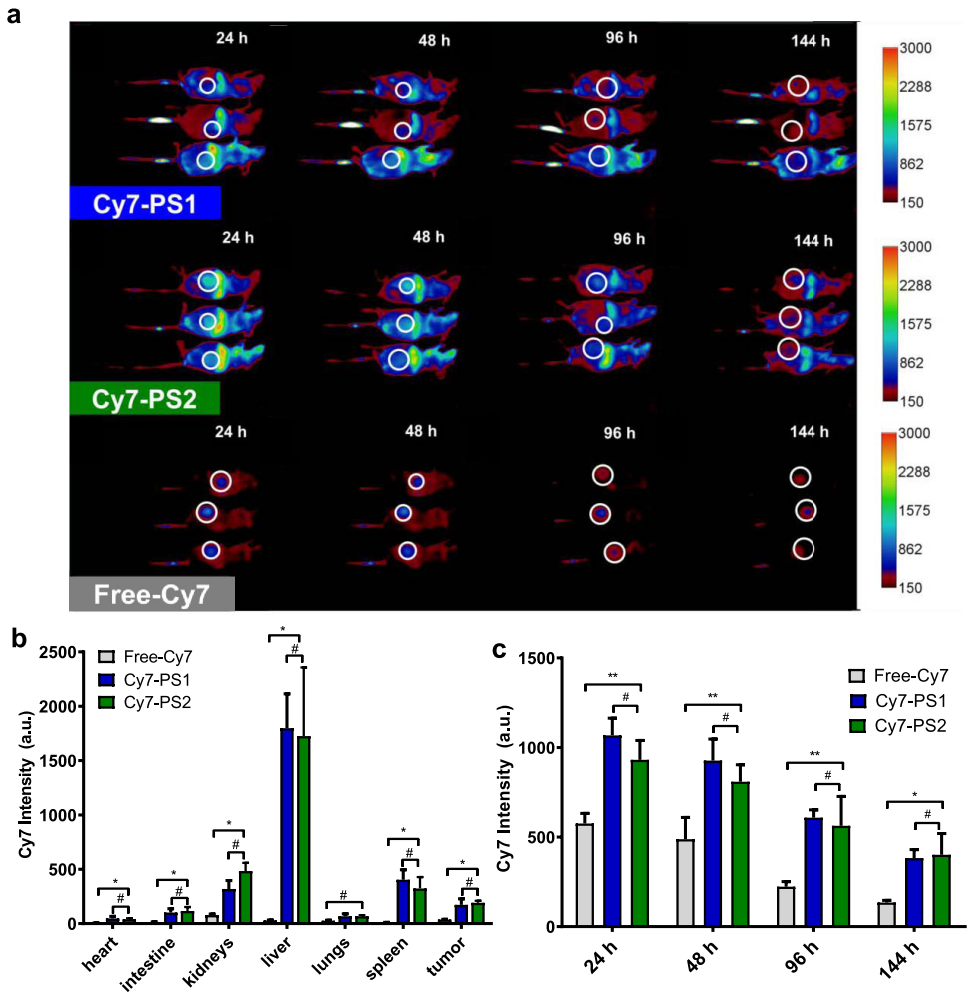

Figure 4. (a) In vivo biodistribution analysis of Cy7-PSs and free fluorescent dye DBCO-Cy7 (free Cy7) over 144 h in mice bearing EL4 T lymphoma tumors. The mice were imaged in the right flank using an Ex/Em = 750/830 nm filter pair to visualize the Cy7 dye (white circles refer to the tumor area). (b) Cy7-PS accumulation in different organs and in EL4 T lymphoma tumors after 7 days of PS administration. (c) Time-dependent accumulation of Cy7-PSs in EL4 T lymphoma tumors compared to free Cy7 administration (* indicates statistical significance provided by one-way ANOVA; $*p < 0.05$; $**p < 0.01$; #, nonsignificant; $n = 3$ mice/group).

deprotection experiments discussed above and confirm that the deprotection (following the self-immolative reaction) of BC2 is more evident than in BC1 (Figures 2, S6, and S7). For BC2, H_2O_2-triggered polymer deprotection is most likely due to the surface-eroded PSs (decrease in $I_{sc} \sim 45\%$) (Figure 2g). The changes in I_{sc} are mostly related to the reduction in $M_{w(PS2)}$ (Table 2 and Figure S9), although a minor change in the refractive index of the polymer was monitored (from 0.173 to 0.166 $mL \cdot g^{-1}$ before and after deprotection, respectively).

PS2 also has been imaged by TEM after incubation in 10 mM H_2O_2 (Figure 2h,i). The PS2 self-assemblies become irregular after 24 h incubation (Figure 2h, arrows) and vanish after 72 h (Figure 2i). The polymeric vesicles were complementarily imaged by cryo-TEM (Figure S10b,c), and surprisingly, PS2 showed a little difference in morphology after incubation in H_2O_2 (Figure S10c), in contrast with PS2 incubated in PBS for 72 h (Figure S10b), suggesting that it is still not completely damaged. Nevertheless, it is much more permeable after H_2O_2 incubation, in agreement with the reduction in light scattering monitored (Figure 2g, open blue circles). The contrast change upon incubation in H_2O_2 is confirmed by plotting the profile of the gray value of the particles using the Image J software (Figure S10b,c, inset).

In Vitro Assays. The ROS responsiveness of the manufactured polymersomes evidenced by ^{1}H NMR, DLS, TEM, and cryo-TEM was expected to influence the release of DOX encapsulated into their aqueous lumen. To evaluate this feature, we prepared DOX-loaded PSs. The values of LE and LC were determined by UV−vis (LE = 36.5% and LC = 3.65% for DOX-PS1 and LE = 34.2% and LC = 3.42% for DOX-PS2). The DOX release was monitored in vitro by UV−vis during 24 h of incubation in PBS or 1 mM H_2O_2. DOX release in the H_2O_2 environment is faster than in PBS, regardless of the polymersome, although a faster release is monitored for PS2 (Figure 3a). Both PSs released DOX twice faster in the simulated ROS-rich microenvironment compared to the release in PBS. This behavior preliminary suggests that they could play an important role in the cytotoxicity to cancer cells.[32−34] In a step further, we evaluated the cellular uptake of DOX-loaded PSs in EL4 and Jurkat lymphoma cells. The cell lines were selected due to their clinical relevance (DOX is frequently used in the treatment of lymphoma tumors) and due to their ROS overproduction.[39−41] The presence of DOX (470/585 nm, Ex/Em) enables the investigation of cellular uptake by flow cytometry. Free DOX and PS1 and PS2 with DOX-loaded equivalent amounts were incubated with the cells,

https://dx.doi.org/10.1021/acs.biomac.9b01748
Biomacromolecules 2020, 21, 1437−1449

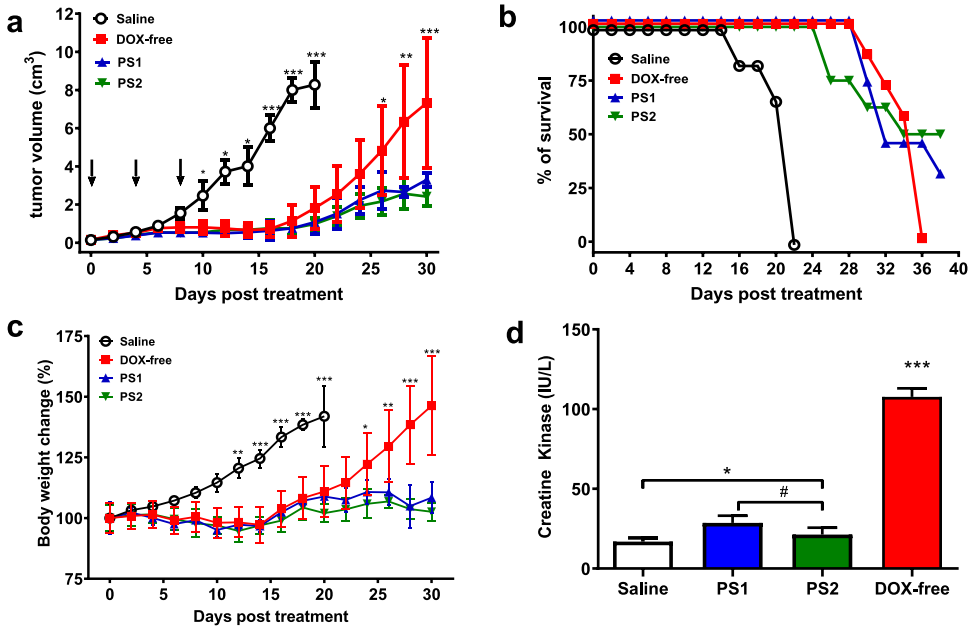

Figure 5. (a) In vivo therapeutic effects of PSs, free DOX, and saline on the growth of T cell lymphoma EL4 (black arrows indicate injections). (b) Kaplan−Meier survival plot of mice after 3 × 5 mg DOX (equiv)/kg administration and untreated control. (c) Body weight changes during PSs and free DOX treatment. (d) Serum creatine kinase levels in the blood after saline, free DOX, PS1, and PS2 administration in mice bearing EL4 T lymphoma. *$p < 0.05$; **$p < 0.01$; ***$p < 0.001$; #, nonsignificant (saline: $n = 6$; free DOX: $n = 8$; PS1: $n = 8$; PS2: $n = 8$).

and fluorescent intensity was monitored. The results provided in Figure 3b evidence similar uptakes of PS1 and PS2, regardless of the cell line. Indeed, the cellular uptake of nanostructures is influenced by the particle size, shape, and surface charge, for instance. Nevertheless, similar uptake behavior is probably due to the identical chemical nature of the nanoparticle shell (PHPMA-stabilized assemblies). Additionally, both assemblies are spherical with similar sizes and surface charges (Table 1).

Afterward, the in vitro therapeutic effect of DOX-loaded PSs for Jurkat and EL4 cells was evaluated using the Alamar Blue assay after 72 h incubation time. Drug-free PSs were also evaluated up to the maximum concentration of 100 $\mu g \cdot mL^{-1}$. In such cases, cell viability was never lower than ∼60% (Figure S12). The cytotoxicities of free DOX and DOX-loaded PSs are similar, as confirmed by the IC_{50} values (Figure 3c,d). The slightly lower IC_{50} value for free DOX, particularly to EL4 cells, is probably due to its ability to diffuse into the cell nuclei.[42−44] Nevertheless, the cytotoxicities of free DOX and DOX-loaded PSs are similar at higher DOX concentrations, pointing out the effectiveness of both formulations against the cancer cell lines. Accordingly, although free DOX is uptaken to a greater extent (Figure 3b), the biological activity is similar to that of DOX-loaded PSs, suggesting that the ROS responsiveness helps the intracellular delivery of the active agent endorsing an efficient cytotoxic effect. Indeed, to demonstrate intracellular polymersome degradation, PSs were also loaded with double-quenched DQ-BSA, which emits fluorescence upon protease cleavage.[45] They were further incubated with EL4 cells, and the fluorescence intensity was monitored by flow cytometry (Figure 2e). The cells were also treated with the ROS inducer phorbol 12-myristate 13-acetate (PMA, 100 nM).[46] In the presence of PMA, the fluorescence was markedly higher in EL4 cells incubated with PS2 (PS2 PMA+) compared to any other evaluated formulation. This is clearly seen in Figure 3f. Furthermore, the same fluorescence intensity is observed for both PSs (Figure 3f) after preincubation with NAC (ROS scavenger)[47] and treatment with PMA, confirming that PS2 is able to selectively release its cargo into ROS-stimulated cancer cells.

In Vivo Assays. The biodistribution assays were performed using the fluorescent dye DBCO-Cyanine7 (Cy7, Figure S11), which can be detected in deep tissues.[48] The Cy7 was conjugated to the ROS-responsive BCs by the copper-free click-chemistry reaction, and the fluorescence in vivo was monitored after the administration of free Cy7 and Cy7-PSs. The in vivo imaging is provided in Figure 4a and the quantitative values in Figure 4b. The PS accumulation is more noticeable in the liver, kidneys, spleen, and tumor. The PS accumulation is generally dependent on the administration route, size, and chemistry (surface charge, hydrophilic shell, shell density). Nevertheless, a higher accumulation in these organs is frequently reported.[48−51] The free Cy7 accumulated ∼2−3 times less in the tumor compared with the PSs at longer incubation times, such as 3−7 days, which is most likely an effect of the long blood circulation promoted by the PSs (Figure 4a,c). The observed enhanced tumor accumulation with prolonged circulation times is favorable for the efficacy of the therapeutic treatment and is in agreement with the results obtained for other similar stealth nanomedicines.[43,49−54]

The accumulation of Cy7-PS1 and Cy7-PS2 in the organs and in the tumor is similar as a consequence of the related features of the vesicles (size, shape, and surface charge). Overall, these results demonstrated that the PSs circulate for reasonably long times in vivo, suggesting that they are potentially able to promote the accumulation of loaded drugs into tumor sites, thereby enhancing the effectiveness of chemotherapeutic treatments.

In line with this, we further evaluated the in vivo antitumor efficacy of the DOX-loaded polymersomes intravenously injected into the tail vein of mice bearing EL4 T cell lymphoma. DOX-loaded PS1 and PS2, PBS, and free DOX

https://dx.doi.org/10.1021/acs.biomac.9b01748
Biomacromolecules 2020, 21, 1437−1449

were administered at a dose of 5 mg DOX (equiv)/kg after 7 days of tumor transplantation on days 0, 4, and 8 (named days of treatment). The tumor growth and mouse survival were monitored, and the results are provided in Figure 5. Enhanced suppression of tumor cell growth and extended survival time are observed when the animals were treated with PSs (Figure 5a,b). Additionally, the side effects of the chemotherapeutic treatment were remarkably reduced when DOX was encapsulated into the polymersomes. This is evidenced by the balanced body weight (Figure 5c) and reduced DOX cardiotoxicity (one of its main shortcomings), as suggested by the reduction of serum creatine kinase levels monitored in mice blood (Figure 5d). Accordingly, the in vivo accumulations of PS1 and PS2 as well as in vitro cellular uptake (for EL4 cells) and cytotoxicity at concentrations higher than 0.1 $\mu g \cdot mL^{-1}$ are similar. Therefore, although PS2 demonstrates deprotection followed by the self-immolative reaction, releasing the cargo (DOX, DQ-BSA) to a greater extent compared to PS1, the efficacy in the treatment of lymphomas in vivo was similar for both evaluated ROS-responsive assemblies.

■ CONCLUSIONS

We describe the successful development of ROS-responsive BCs to manufacture PSs with the tunable site-specific release of the chemotherapeutic drug DOX. We demonstrated that BC and PS chemistry influences the deprotection behavior, showing dependence on BC deprotection linkage and H_2O_2 conditions. The results from this pioneering work suggest that the ROS-responsive PSs produced exhibit the physicochemical and biological properties required for practical applications as nanomedicines with potential for tumor-targeting DOX delivery based on the ROS-triggered release mechanism in vitro and in vivo. Furthermore, the simplicity and effectiveness of the PS approach and the ability to chemically modify the resulting particles ensure the application in various fields of research and for different disease treatments.

■ ASSOCIATED CONTENT

Supporting Information

The Supporting Information is available free of charge at https://pubs.acs.org/doi/10.1021/acs.biomac.9b01748.

Synthetic routes and molecular structures of PHPMA macroCTA, ROS-responsive monomers, and BCs; SEC chromatograms of PHPMA macroCTA and of the BCs before and after deprotection; ^{1}H NMR spectra of PHPMA macroCTA and BCs; ^{1}H NMR spectra of the BCs during deprotection; H_2O_2 scavenging ability test; Zimm plots of the PSs before and after deprotection; TEM and cryo-TEM micrographs; and cellular viability data (PDF)

■ AUTHOR INFORMATION

Corresponding Author

Eliézer Jäger − *Institute of Macromolecular Chemistry, 162 06 Prague, Czech Republic;* orcid.org/0000-0001-9939-2355; Email: jager@imc.cas.cz

Authors

Vladimir Sincari − *Institute of Macromolecular Chemistry, 162 06 Prague, Czech Republic*

Lindomar J. C. Albuquerque − *Centro de Ciências Naturais e Humanas, Universidade Federal do ABC, Santo André 09210-580, Brazil;* orcid.org/0000-0003-1443-1795

Alessandro Jäger − *Institute of Macromolecular Chemistry, 162 06 Prague, Czech Republic;* orcid.org/0000-0001-6171-4718

Jana Humajova − *Institute of Biophysics and Informatics, First Faculty of Medicine, Charles University in Prague, 120 00 Prague, Czech Republic*

Jan Kucka − *Institute of Macromolecular Chemistry, 162 06 Prague, Czech Republic*

Jan Pankrac − *Center for Advanced Preclinical Imaging (CAPI), First Faculty of Medicine, Charles University, 120 00 Prague, Czech Republic*

Petr Paral − *Center for Advanced Preclinical Imaging (CAPI), First Faculty of Medicine, Charles University, 120 00 Prague, Czech Republic*

Tomas Heizer − *Center for Advanced Preclinical Imaging (CAPI), First Faculty of Medicine, Charles University, 120 00 Prague, Czech Republic*

Olga Janouskova − *Institute of Macromolecular Chemistry, 162 06 Prague, Czech Republic*

Rafał Konefał − *Institute of Macromolecular Chemistry, 162 06 Prague, Czech Republic*

Ewa Pavlova − *Institute of Macromolecular Chemistry, 162 06 Prague, Czech Republic*

Ondrej Sedlacek − *Institute of Macromolecular Chemistry, 162 06 Prague, Czech Republic;* orcid.org/0000-0001-5731-2687

Fernando C. Giacomelli − *Centro de Ciências Naturais e Humanas, Universidade Federal do ABC, Santo André 09210-580, Brazil;* orcid.org/0000-0002-6872-9354

Pavla Pouckova − *Institute of Biophysics and Informatics, First Faculty of Medicine, Charles University in Prague, 120 00 Prague, Czech Republic*

Ludek Sefc − *Center for Advanced Preclinical Imaging (CAPI), First Faculty of Medicine, Charles University, 120 00 Prague, Czech Republic*

Petr Stepanek − *Institute of Macromolecular Chemistry, 162 06 Prague, Czech Republic;* orcid.org/0000-0003-1433-678X

Martin Hruby − *Institute of Macromolecular Chemistry, 162 06 Prague, Czech Republic;* orcid.org/0000-0002-5075-261X

Complete contact information is available at: https://pubs.acs.org/10.1021/acs.biomac.9b01748

Author Contributions

The manuscript was written through contributions of all authors. All authors have given approval to the final version of the manuscript.

Notes

The authors declare no competing financial interest.

■ ACKNOWLEDGMENTS

This work was sponsored by the Czech Science Foundation (grant no. 17-09998S). A.J. and V.S. acknowledge the Czech Ministry of Education, Youth and Sports (grant no. 8J18FR038). P.S. acknowledges grant no. LM2015064 ERIC and grant POLYMAT#LO1507. M.H. thanks the Ministry of Health of the Czechia (grant no. AZV16-30544A). F.C.G. and L.J.C.A. acknowledge FAPESP (grants 2017/00459-4 and 2017/11261-0). Electron microscopy was supported by TA CR (no. TN01000008). The CAPI experiments were

supported by the Ministry of Education, Youth and Sports of the Czech Republic (Large RI Project LM2015062 Czech-BioImaging and SVV 260371/2019) and by the European Regional Development Fund (Project No. CZ.02.1.01/0.0/0.0/16_013/0001775). The authors would like to thank Dr. Martijn Verdoes for his valuable comments and suggestions.

■ REFERENCES

(1) Siegel, R.; Naishadham, D.; Jemal, A. Cancer statistics, 2013. *CA Cancer J. Clin.* **2013**, *63*, 11−30.

(2) Rupp, T.; Zuckerman, D. Quality of Life, Overall Survival, and Costs of Cancer Drugs Approved Based on Surrogate Endpoints. *JAMA Intern. Med.* **2017**, *177*, 276−277.

(3) Maeda, H.; Khatami, M. Analyses of repeated failures in cancer therapy for solid tumors: poor tumor-selective drug delivery, low therapeutic efficacy and unsustainable costs. *Clin. Transl. Med.* **2018**, *7*, No. 11.

(4) Ellis, E.; Zhang, K.; Lin, Q.; Ye, E.; Poma, A.; Battaglia, G.; Loh, X. J.; Lee, T.-C. Biocompatible pH-responsive nanoparticles with a core-anchored multilayer shell of triblock copolymers for enhanced cancer therapy. *J. Mater. Chem. B* **2017**, *5*, 4421−4425.

(5) Joseph, A.; Contini, C.; Cechin, D.; Nyberg, S.; Ruiz-Perez, L.; Gaitzsch, J.; Fullstone, G.; Tian, X.; Azizi, J.; Preston, J.; Volpe, G.; Battaglia, G. Chemotactic synthetic vesicles: Design and applications in blood-brain barrier crossing. *Sci. Adv.* **2017**, *3*, No. e1700362.

(6) Marguet, M.; Bonduellea, C.; Lecommandoux, S. Multicompartmentalized polymeric systems: towards biomimetic cellular structure and function. *Chem. Soc. Rev.* **2013**, *42*, 512−529.

(7) Palivan, C. G.; Goers, R.; Najer, A.; Zhang, X.; Car, A.; Meier, W. Bioinspired polymer vesicles and membranes for biological and medical applications. *Chem. Soc. Rev.* **2016**, *45*, 377−411.

(8) Hu, X.; Zhang, Y.; Xie, Z.; Jing, X.; Belloti, A.; Gu, Z. Stimuli-Responsive Polymersomes for Biomedical Applications. *Biomacromolecules* **2017**, *18*, 649−673.

(9) Yao, P.; Zhang, Y.; Meng, H.; Sun, H.; Zhong, Z. Smart Polymersomes Dually Functionalized with cRGD and Fusogenic GALA Peptides Enable Specific and High-Efficiency Cytosolic Delivery of Apoptotic Proteins. *Biomacromolecules* **2019**, *20*, 184−191.

(10) Schatz, C.; Louguet, S.; Le Meins, J. F.; Lecommandoux, S. Polysaccharide-block-polypeptide copolymer vesicles: towards synthetic viral capsids. *Angew. Chem., Int. Ed.* **2009**, *48*, 2572−2575.

(11) Le Meins, J. F.; Sandre, O.; Lecommandoux, S. Recent trends in the tuning of polymersomes' membrane properties. *Eur. Phys. J. E* **2011**, *2*, 1−17.

(12) Rideau, E.; Dimova, R.; Schwille, P.; Wurm, F. R.; Landfester, K. Liposomes and polymersomes: a comparative review towards cell mimicking. *Chem. Soc. Rev.* **2018**, *47*, 8572−8610.

(13) Meng, F.; Zhong, Z.; Feijen, J. Stimuli-Responsive Polymersomes for Programmed Drug Delivery. *Biomacromolecules* **2009**, *10*, 197−209.

(14) Peters, R. J. R. W.; Marguet, M.; Marais, S.; Fraaije, M. W.; Van Hest, J. C. M.; Lecommandoux, S. Cascade reactions in multicompartmentalized polymersomes. *Angew. Chem., Int. Ed.* **2014**, *53*, 146−150.

(15) Chen, W.; Meng, F.; Cheng, R.; Zhong, Z. pH-Sensitive degradable polymersomes for triggered release of anticancer drugs: A comparative study with micelles. *J. Controlled Release* **2010**, *142*, 40−46.

(16) Lee, J. S.; Feijen, J. Polymersomes for drug delivery: Design, formation and characterization. *J. Controlled Release* **2012**, *161*, 473−483.

(17) Oliveira, H.; Peres-Andres, E.; Thevenot, J.; Sandre, O.; Berra, E.; Lecommandoux, S. Magnetic field triggered drug release from polymersomes for cancer therapeutics. *J. Controlled Release* **2013**, *169*, 165−170.

(18) Che, H.; Hest, J. C. M. Adaptive Polymersome Nanoreactors. *ChemNanoMat* **2019**, *5*, 1092−1109.

(19) Deng, Z.; Hu, J.; Liu, S. Reactive Oxygen, Nitrogen, and Sulfur Species (RONSS)-Responsive Polymersomes for Triggered Drug Release. *Macromol. Rapid Commun.* **2017**, *38*, No. 1600685.

(20) Tanner, P.; Balasubramanian, V.; Palivan, C. G. Aiding Nature's Organelles: Artificial Peroxisomes Play Their Role. *Nano Lett.* **2013**, *13*, 2875−2883.

(21) Richard, P. U.; Craciun, I.; Gaitzsch, J.; Weiner, L.; Palivan, C. G. Delivery of ROS Generating Anthraquinones Using Reduction-Responsive Peptide-Based Nanoparticles. *Helv. Chim. Acta* **2018**, *101*, No. e1800064.

(22) Kim, K. T.; Cornelissen, J. J. L. M.; Nolte, R. J. M.; van Hest, J. C. M. A Polymersome Nanoreactor with Controllable Permeability Induced by Stimuli-Responsive Block Copolymers. *Adv. Mater.* **2009**, *21*, 2787−2791.

(23) Liou, G. Y.; Storz, P. Reactive oxygen species in cancer. *Free Radical Res.* **2010**, *44*, 479−496.

(24) Minelli, A.; Bellezza, I.; Conte, C.; Culig, Z. Oxidative stress-related aging: A role for prostate cancer? *Biochim. Biophys. Acta* **2009**, *1795*, 83−91.

(25) Hancock, J. T.; Desikan, R.; Neill, S. J. Role of reactive oxygen species in cell signalling pathways. *Biochem. Soc. Trans.* **2001**, *29*, 345−350.

(26) D'Autréaux, B.; Toledano, M. B. ROS as signalling molecules: mechanisms that generate specificity in ROS homeostasis. *Nat. Rev. Mol. Cell Biol.* **2007**, *8*, 813−824.

(27) Ye, H.; Zhou, Y.; Liu, X.; Chen, Y.; Duan, s.; Zhu, R.; Liu, Y.; Yin, L. Recent Advances on Reactive Oxygen Species-Responsive Delivery and Diagnosis System. *Biomacromolecules* **2019**, *20*, 2441−2463.

(28) Albuquerque, L. J. C.; Sincari, V.; Jäger, A.; Konefał, R.; Pánek, J.; Černoch, P.; Pavlova, E.; Štěpánek, P.; Giacomelli, F. C.; Jäger, E. Microfluidic-assisted engineering of quasi-monodisperse pH-responsive polymersomes toward advanced platforms for the intracellular delivery of hydrophilic therapeutics. *Langmuir* **2019**, *35*, 8363−8372.

(29) Zhao, W. Lighting up H_2O_2: the molecule that is a "necessary evil" in the cell. *Angew. Chem., Int. Ed.* **2009**, *48*, 3022−3024.

(30) Lin, V. S.; Dickinson, B. C.; Chang, C. J. Boronate-based fluorescent probes: imaging hydrogen peroxide in living systems. *Methods Enzymol.* **2013**, *526*, 19−43.

(31) de Gracia Lux, C.; Joshi-Barr, S.; Nguyen, T.; Mahmoud, E.; Schopf, E.; Fomina, N.; Almutairi, A. Biocompatible polymeric nanoparticles degrade and release cargo in response to biologically relevant levels of hydrogen peroxide. *J. Am. Chem. Soc.* **2012**, *134*, 15758−15764.

(32) Stubelius, A.; Lee, S.; Almutairi, A. The Chemistry of Boronic Acids in Nanomaterials for Drug Delivery. *Acc. Chem. Res.* **2019**, *52*, 3108−3119.

(33) Wang, J.; Wang, X.; Zhang, S.; Yu, D.; Wen, Q.; Hu, Y.; Ye, H. H.; Bomba, X.; Hu, Z.; Liu, G.; Dotti, Z.; Gu. In situ formed reactive oxygen species-responsive scaffold with gemcitabine and checkpoint inhibitor for combination therapy. *Sci. Transl. Med.* **2018**, *10*, No. eaan3682.

(34) Jäger, E.; Höcherl, A.; Janoušková, O.; Jäger, A.; Hrubý, M.; Konefał, R.; Netopilik, M.; Pánek, J.; Šlouf, M.; Ulbrich, K.; Štěpánek, P. Fluorescent boronate-based polymer nanoparticles with reactive oxygen species (ROS)-triggered cargo release for drug-delivery applications. *Nanoscale* **2016**, *8*, 6958.

(35) Liang, X.; Duan, J.; Li, X.; Zhu, X.; Chen, Y.; Wang, X.; Sun, H.; Kong, D.; Li, C.; Yang, J. Improved vaccine-induced immune responses via a ROS-triggered nanoparticle-based antigen delivery system. *Nanoscale* **2018**, *10*, 9489−9503.

(36) Lebleu, C.; Rodrigues, L.; Guigner, J.-M.; Brulet, A.; Garanger, E.; Lecommandoux, S. Self-Assembly of PEG-*b*-PTMC Copolymers: Micelles and Polymersomes Size Control. *Langmuir* **2019**, *35*, 13364−13374.

(37) de Castro Carlos, C.; Mattei, B.; Riske, C. A.; Jäger, E.; Jäger, A.; Štěpánek, P.; Giacomelli, F. C. Understanding the Structural Parameters of Biocompatible Nanoparticles Dictating Protein Fouling. *Langmuir* **2014**, *30*, 9770−9779.

(38) Zhang, Q.; Zhang, F.; Chen, Y.; Dou, Y.; Tao, H.; Zhang, D.; Wang, R.; Li, X.; Zhang, J. Structure-Property Correlations of Reactive Oxygen Species-Responsive and Hydrogen Peroxide-Eliminating Materials with Anti-Oxidant and Anti-Inflammatory Activities. *Chem. Mater.* **2017**, *29*, 8221−8238.
(39) Bur, H.; Haapasaari, K.-M.; Turpeenniemi-Hujanen, T.; Kuittinen, O.; Auvinen, O.; Marin, K.; Koivunen, P.; Sormunen, R.; Soini, Y.; Karihtala, P. Oxidative stress markers and mitochondrial antioxidant enzyme expression are increased in aggressive Hodgkin lymphomas. *Histopathology* **2014**, *65*, 319−327.
(40) Klaunig, J. E.; Xu, Y.; Isenberg, J. S.; Bachowski, S.; Kolaja, K. L.; Jiang, J.; Stevenson, D. E.; Walborg, E. F., Jr. The Role of Oxidative Stress in Chemical Carcinogenesis. *Environ. Health Perspect.* **1998**, *106*, 289−295.
(41) Liu, Y.; Fang, J.; Kim, Y.-J.; Wong, M. K.; Wang, P. Codelivery of Doxorubicin and Paclitaxel by Cross-Linked Multilamellar Liposome Enables Synergistic Antitumor Activity. *Mol. Pharmaceutics* **2014**, *11*, 1651−1661.
(42) Strozyk, M. S.; Carregal-Romero, S.; Henriksen-Lacey, M.; Brust, M.; Liz-Marzan, L. M. Biocompatible, Multiresponsive Nanogel Composites for Codelivery of Antiangiogenic and Chemotherapeutic Agents. *Chem. Mater.* **2017**, *29*, 2303−2313.
(43) Cui, C.; Xue, Y.-N.; Wu, M.; Zhang, Y.; Yu, P.; Liu, L.; Zhuo, R.-X.; Huang, W. Cellular uptake, intracellular trafficking, and antitumor efficacy of doxorubicin-loaded reduction-sensitive micelles. *Biomaterials* **2013**, *34*, 3858−3869.
(44) Hu, X.; Liu, S.; Huang, X.; Chen, X.; Jing, X. Biodegradable Block Copolymer-Doxorubicin Conjugates via Different Linkages: Preparation, Characterization, and In Vitro Evaluation. *Biomacromolecules* **2010**, *11*, 2094−2102.
(45) Büll, C.; Boltje, T. J.; Van Dinther, E. A. W.; Peter, T.; De Graaf, A. M. A.; Lausen, J. H. W.; Kreutz, M.; Figdor, C. G.; Den Brok, M. H.; Adema, G. J. Targeted Delivery of a Sialic Acid-Blocking Glycomimetic to Cancer Cells Inhibits Metastatic Spread. *ACS Nano* **2015**, *9*, 733−745.
(46) Nunes-Hasler, P.; Maschalidi, S.; Lippens, C.; Castelbou, C.; Bouvet, S.; Guido, D.; Bermont, F.; Bassoy, E. Y.; Page, N.; Merkler, D.; Hugues, S.; Martinvalet, D.; Manoury, B.; Demaurex, N. STIM1 promotes migration, phagosomal maturation and antigen cross-presentation in dendritic cells. *Nat. Commun.* **2017**, *8*, No. 1852.
(47) Halasi, M.; Wang, M.; Chavan, T. S.; Gaponenko, V.; Hay, N.; Gartel, A. L. ROS inhibitor *N*-acetyl-L-cysteine antagonizes the activity of proteasome inhibitors. *Biochem. J.* **2013**, *454*, 201−208.
(48) Yang, K.; Zhang, S.; Zhang, G.; Sun, X.; Lee, S. T.; Liu, Z. Graphene in Mice: Ultrahigh In Vivo Tumor Uptake and Efficient Photothermal Therapy. *Nano Lett.* **2010**, *10*, 3318−3323.
(49) Photos, P. J.; Bacakova, L.; Discher, B.; Bates, F. S.; Discher, D. E. Polymer vesicles in vivo: correlations with PEG molecular weight. *J. Controlled Release* **2003**, *90*, 323−334.
(50) Chiang, Y.-T.; Cheng, Y.-T.; Lu, C.-Y.; Yen, Y.-W.; Yu, L.-Y.; Yu, K.-S.; Lyu, S.-Y.; Yang, C.-Y.; Lo, C.-L. Polymer-Liposome Complexes with a Functional Hydrogen-Bond Cross-Linker for Preventing Protein Adsorption and Improving Tumor Accumulation. *Chem. Mater.* **2013**, *25*, 4364−4372.
(51) Jeannot, V.; Gauche, C.; Mazzaferro, S.; Couvet, M.; Vanwonterghen, L.; Henry, M.; Dider, C.; Vollaire, J.; Josserand, V.; Col, J.-L.; Schatz, C.; Leccommandoux, S.; Hurbin, A. Anti-tumor efficacy of hyaluronan-based nanoparticles for the co-delivery of drugs in lung cancer. *J. Controlled Release* **2018**, *275*, 117−128.
(52) Qiu, M.; Zhang, Z.; Wei, Y.; Sun, H.; Meng, F.; Deng, C.; Zhong, Z. Small-Sized and Robust Chimaeric Lipopepsomes: A Simple and Functional Platform with High Protein Loading for Targeted Intracellular Delivery of Protein Toxin in Vivo. *Chem. Mater.* **2018**, *30*, 6831−6838.
(53) Kwon, G. S.; Kataoka, K. Block copolymer micelles as long-circulating drug vehicles. *Adv. Drug Delivery Rev.* **1995**, *16*, 295−309.
(54) Lee, J. S.; Ankone, M.; Peiters, E.; Schiffelers, R. M.; Hennink, W. W.; Feijen, J. Circulation kinetics and biodistribution of dual-labeled polymersomes with modulated surface charge in tumor-bearing mice: Comparison with stealth liposomes. *J. Controlled Release* **2011**, *155*, 282−288.

https://dx.doi.org/10.1021/acs.biomac.9b01748
Biomacromolecules 2020, 21, 1437−1449

Please do not adjust margins

ARTICLE

pH-dependent disruption of giant polymer vesicles: A step towards biomimetic membranes

Received 00th January 20xx,
Accepted 00th January 20xx

DOI: 10.1039/x0xx00000x

Vladimir Sincari[a], Eliézer Jäger[a], Kahynna Loureiro Cavalcante[a], Martina Vragovic[a], Eddie Hofmann[b], Mathias Shlenk[b], Petr Štěpánek[a], Martin Hrubý[a], Stephan Förster[b,c,d] and Alessandro Jäger*[a]

Polymer giant unilamellar vesicles (PGUVs) capable of selectively delivering protected payloads into intracellular environments and releasing them in stimuli-triggered, precise spatially and temporally controlled manners are attractive bioactive cargo delivery tools. Herein, we present highly size-defined and monodisperse (42.1 ± 1.2, 60.5 ± 1.0, 80.4 ± 1.4 and 97.9 ± 1.2 µm in diameter, respectively) pH-responsive giant PGUVs prepared via microfluidic droplet generation using a flow-focusing poly(dimethylsiloxane) (PDMS)-based microfluidic device. Poly(ethylene oxide)-*block*-poly[2-(diisopropylamino)ethyl methacrylate] (PEO-*b*-PDPA) is a pH-responsive polymer that was synthesized via reversible addition−fragmentation chain-transfer (RAFT) polymerization and used in combination with poly(ethylene oxide)-*block*-poly(1,2-butadiene) (PEO-*b*-PBD) to produce homogeneous pH-responsive giant PGUVs. To demonstrate the spatiotemporal control provided by this approach, we studied in detail the pH-responsiveness of PGUVs according to the disruption and release of dye cargo under distinct acidic conditions using fluorescence confocal microscopy. This approach can be utilized to fabricate pH-responsive delivery systems for various active compounds, microreactors, and artificial organelles, thereby paving the way towards cell mimicry.

Introduction

Polymer vesicles are self-assemblies of amphiphilic diblock copolymers that correspond to hollow structures surrounded by polymer bilayer membranes.[1] Their bilayer membrane can encapsulate and release hydrophobic molecules, while their aqueous core is used for hydrophilic cargo.[2] In contrast to lipid vesicles, which are also known as liposomes, polymeric vesicles are more versatile and possess enhanced microstructural stability, as well as compromised bilayer permeability.[3] In terms of size, vesicles can be classified as either small, with diameters in the hundreds of nm range, or giant, with diameters >1 µm.[4] One application of giant polymer vesicles is as synthetic compartments in artificial cells and organelles.[5–8] Specifically, polymer giant unilamellar vesicles (PGUVs) have become increasingly popular model systems in bottom-up synthetic biology because they can be manufactured from lipids and/or amphiphilic block copolymers to match the dimensions and basic functions of eukaryotic cells.[9] PGUVs can be observed under optical microscopes using various enhancement techniques, such as phase contrast, differential interference contrast, and confocal and standard fluorescence microscopy. The versatility and enhanced properties of PGUVs include control over block lengths,[10] molecular weights,[11] and functionalization with specific groups[12] to create stimuli-responsive systems. However, it is very challenging to develop pH-sensitive PGUVs that can quickly release drugs under the acidic conditions encountered in some pathological microenvironments, such as cancer[13], inflammation[14], and ischemia[15], or upon vesicle endocytosis in early endosomes[16]. Recently, Gibson et al. designed pH-responsive giant hybrid polymer/lipid unilamellar vesicles (GHUVs) formulated with poly(ethylene oxide)-*block*-poly(dimethylsiloxane) and a cationic switchable lipid prepared by an electroformation method.[17] The latter component undergoes a pH-triggered conformational change that induces membrane destabilization and GHUV morphological changes, such as protrusions and fission upon acidification. Additionally, by monitoring the fluorescence leakage of the encapsulated calcein, the authors noted that GHUV membrane permeability to calcein increases under acidic conditions. Although these results are promising, the authors could not control the amount of cationic lipids in different GHUVs and therefore the release of calcein from the GHUVs because of a lack of control in their preparation method.

[a.] *Institute of Macromolecular Chemistry, Heyrovsky Sq. 2, 162 06 Prague 6, Czech Republic.*
[b.] *Department of Chemistry, University of Bayreuth, 95447 Bayreuth, Germany.*
[c.] *JCNS-1/ICS-1, Forschungszentrum Jülich, 52425 Jülich, Germany.*
[d.] *Physical Chemistry, RWTH University, 52074 Aachen, Germany.*

† Electronic Supplementary Information (ESI) available: [details of any supplementary information available should be included here]. See DOI: 10.1039/x0xx00000x

Please do not adjust margins

Please do not adjust margins

Currently, GHUVs and PGUVs can both be manufactured through various methods, such as film rehydration,[18] electroformation[19], emulsion centrifugation and polymerization-induced self-assembly.[20] Although the vesicles can be produced through simple methods, the assemblies produced by these methods are naturally polydisperse and have low drug-loading efficiency[21]. In contrast, microfluidic techniques use microdroplet technology to create double emulsions of water-in-oil-in-water (w/o/w), thereby allowing precise control over vesicle formation, with a narrow monodisperse size distribution and improved encapsulation of several compounds.[22,23] Microfluidic devices for the production of giant vesicles include glass capillary devices, 3D-printed devices, and PDMS systems based on soft lithography processes.[24] Glass capillary systems encounter difficulties in terms of channel design and customization, while 3D-printed devices face material property limitations and imprecise channel lengths.[25] In contrast, PDMS devices fabricated by soft lithography can be prepared with various sophisticated channel designs with high accuracy.[26] However, PDMS can be used directly with only a few solvents, such as alcohols and oils. Since PDMS has poor chemical resistance and swells when contacting many organic solvents, additional coatings, such as glass-like sol-gel, are generally applied.[27] Sol-gel coatings, such as tetraethoxysilane (TEOS) modification, produce durable glass-like layers that significantly increase the resistance of PDMS channel walls.

Although the field has progressed substantially, the production of PGUVs that respond to relevant physiological conditions has not yet been reported. Herein, we report a novel microfluidic technology for developing extremely monodisperse pH-responsive PGUVs through a water/oil/water (W/O/W) double emulsion method prepared via a microfluidic PDMS device. The PDMS devices were fabricated by soft lithography, and the microchannels were coated with a sol-gel tetraethyl orthosilicate (TEOS) technique that produced durable glass-like layers, thereby significantly increasing the resistance of the PDMS to organic solvents. The selected inner junction channels were rendered by hydrophilic coatings with PEO via plasma activation to generate double emulsion microdroplets. As a pH-responsive polymer, poly(ethylene oxide)-*block*-poly[2-(diisopropylamino)ethyl methacrylate] (PEO_{45}-*b*-$PDPA_{20}$) was synthesized by controlled reversible addition–fragmentation chain-transfer (RAFT) polymerization and used in combination with commercial poly(ethylene oxide)-*block*-poly(1,2-butadiene) (PEO_{34}-*b*-PBD_{46}) to produce homogeneous pH-responsive PGUVs. The pH response was studied in detail by confocal microscopy, and the results demonstrate prompt spatial and temporal pH-controlled PGUV disruption under the relevant simulated physiological conditions. This approach can be utilized to fabricate pH-responsive delivery systems for several active compounds, microreactors, and artificial organelles, paving the way towards cell mimicry with an unprecedently defined, controlled, robust and simple approach.

Results and Discussion

Synthesis and characterization of the block copolymer

Poly(ethylene oxide)-*b*-poly[2-(diisopropylamino)ethyl methacrylate (PEO-*b*-PDPA) diblock copolymer was successfully synthesized by RAFT polymerization, from which the commercial PEO macro chain-transfer agent (PEO macroCTA) (M_n = 2000 g mol^{-1}) 2-(diisopropylamino)ethyl methacrylate (DPA) monomer was grown. This monomer was carefully chosen because it is an ultra-pH-sensitive monomer that undergoes a hydrophobic/hydrophilic switch in the small pH window of 6.30 < pH < 6.95, which is remarkably close to the pH of the microenvironment in tumour cells; thus, this block copolymer is particularly useful for various biological applications (discussed hereafter).[28,29]

The weight-average molecular weight (M_w = 6 945 g·mol^{-1}), number-average molecular weight (M_n = 6 257 g·mol^{-1}) and dispersity (M_w/M_n = $Đ$ = 1.11) of the block copolymer were determined by SEC (Fig. S1a), and the composition was characterized by ^{1}H NMR spectroscopy, showing the characteristic signals of protons belonging to PEO and DPA repeated units (Fig. S1b). The weight fraction of the hydrophilic block (PEO) was 28%, which is within the well-known range for obtaining polymer vesicles. [30]

Microfluidic setup

We designed a microfluidic device for producing monodisperse W/O/W double emulsions that includes a six-way PDMS junction (Fig. 1) with one inner aqueous phase (IA) channel, two polymer-carrying organic phase (PO) channels, two outer aqueous phase (OA) channels and a downstream channel. The PDMS structures were fabricated using soft lithography of a silicon template (see Methods). A critical design step is controlling the hydrophobicity/hydrophilicity of the channels. To prevent the adsorption of droplets on the surface of the channel, the post-junction and main channel areas were coated with poly(ethylene oxide) (PEO; Supplementary Fig. S2; Methods). It is worth mentioning that stable W/O/W double-emulsion droplets are produced only after successful hydrophilic coverage of the regions of interest by PEO. Using independent syringe pumps, the IA stream and surrounding PO streams were hydrodynamically focused and subsequently compressed/squeezed by the two OA streams (Fig. 1). This approach produced stable and monodisperse double-emulsion droplets stabilized by PEO_{34}-*b*-PBD_{46} and/or PEO_{34}-*b*-PBD_{46} and PEO_{45}-*b*-$PDPA_{20}$ in a single step in the proposed microfluidic device (Fig. 1b). In the 6-channel microfluidic device, double-emulsion droplets are formed in the dripping regime at the junction where the 5 inlet streams meet after being focused in the main downstream channel in the direction of the outlet. The IA stream generates an inner aqueous emulsion droplet that is stabilized by the two PO streams and simultaneously broken down by the OA streams (Fig. 1a, Video S1). Because the IA phase is in contact with only the immiscible PO phase, hydrophilic compounds in the inner aqueous droplet of

This journal is © The Royal Society of Chemistry 20xx

Please do not adjust margins

Please do not adjust margins

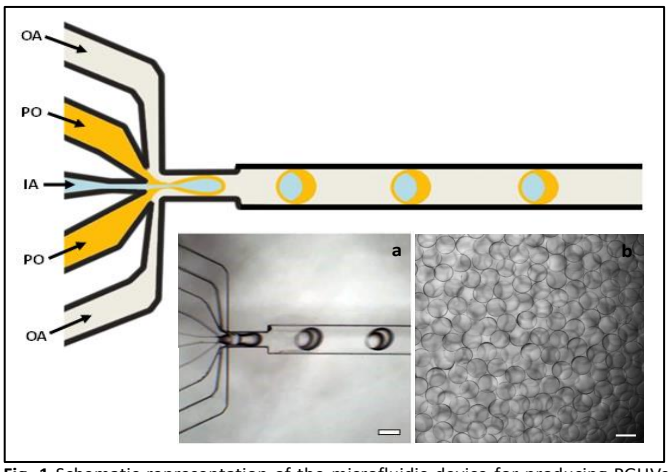

Fig. 1 Schematic representation of the microfluidic device for producing PGUVs using W/O/W double-emulsion droplets. (a) Bright field microscopy images of the microfluidic device producing W/O/W double-emulsion droplets and (b) PGUVs after solvent evaporation (overnight at room temperature under nitrogen flow). The scale bar represents 100 µm.

the double emulsion are retained without leakage to the outer continuous phase during emulsion fabrication. This concept is demonstrated by the addition of calcein to the IA stream and Nile red to the PO streams during the production of the double-emulsion droplets (Fig. 2). After toluene evaporation, the calcein was trapped in the aqueous phase, while the Nile red was found in the polymeric bilayer, allowing simultaneous observation of the PGUV aqueous core and bilayer shell using fluorescence microscopy.

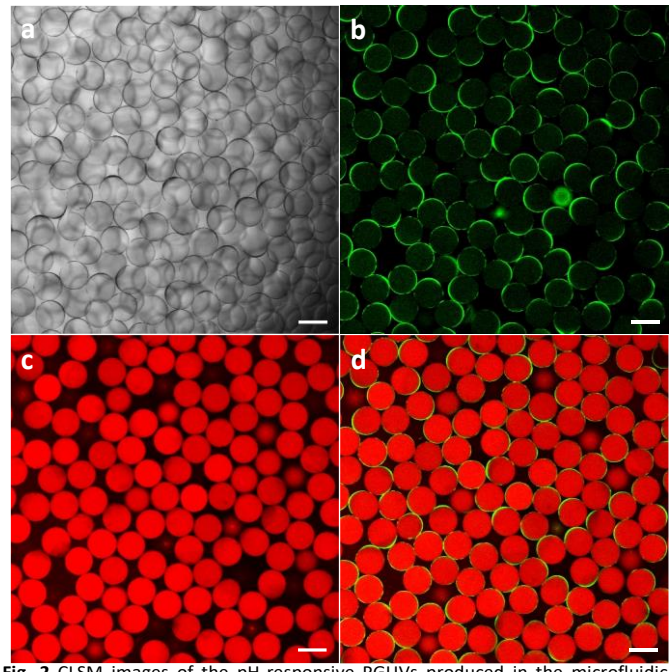

Fig. 2 CLSM images of the pH-responsive PGUVs produced in the microfluidic devices using Nile red and calcein. (a) Using only the bright field, (b) using only the fluorescent excitation/emission range of Nile red (λ_{ex} = 635 nm; λ_{em} = 645-665 nm), (c) using only the excitation/emission range of calcein (λ_{ex} = 488 nm; λ_{em} = 510-545 nm) and (d) using the excitation/emission ranges of both Nile red and calcein. The scale bar denotes 100 µm.

Transition from double emulsions to large vesicles

According to Weitz et al.[31], the transition from monodisperse W/O/W double-emulsion droplets to giant vesicles can be described by various dewetting stages. The entire process occurs in approximately 5 minutes and was followed by bright field microscopy observations (Fig. S2). During the first stage, the layer containing the organic solvent wets almost the entire drop. This step is very fast, occurring in only a few seconds; therefore, this stage could not be observed under the microscope. In the next stage, the organic layer dewets from the inner drop, and the polymer migrates to the interface, resulting in a water droplet surrounded by a thin polymeric layer (Fig. S2, 15 to 300 s). Thereafter, no changes were observed in the droplets over 24 hours, and we assume that toluene was completely evaporated. The final morphology is a vesicular system composed of a uniform bilayer of PEO_{34}-*b*-PBD_{46} with PEO_{45}-*b*-$PDPA_{20}$ copolymers sitting at the interface between the aqueous core and external water phase, thereby forming stable PGUVs (Fig. S3, 24 h).

Tuning the size of monodisperse PGUVs

A very important parameter of PGUV production is controlling and fine tuning the size and dispersity of the PGUVs. In this respect, existing microfluidic methods can easily produce monodisperse PGUVs in the range of 5 to 500 µm.[32] Fig. 3a shows the frequency histogram distributions of four batches of PGUVs produced in the size range of 40 to 100 µm. The red lines are Gaussian fits to each individual histogram distribution, and the arrows indicate the mean diameters and standard deviations (from left to right: 42.1 ± 1.2, 60.5 ± 1.0, 80.4 ± 1.4 and 97.9 ± 1.2 µm, see Methods). In each batch, a very narrow and monodisperse size distribution was obtained, with the coefficient of variation ranging between 1 and 4%. A clear example of the monodispersity of the PGUV systems is shown in the confocal laser scanning microscopy (CLSM) images of two distinct batches with sizes of 42.1 (Fig. 3c) and 97.9 µm (Fig. 3d). Concerning the manipulation of the particle size, it is well established that the flow rate of the OA and IA streams dictates the final PGUV diameter. The flow rate of the IA stream governs the amount of fluid that is encapsulated, while the flow rate of the OA stream determines how frequently pinch-off occurs. Thus, the lower the flow rate of the IA stream and the higher the flow rate of OA stream, the smaller the size of the primary W/O/W emulsion droplets and thus the final size of the PGUVs. Additionally, the dimensions of the IA channel determine the minimum fluid volume that is encapsulated, setting a lower limit on the PGUVs. For example, by manipulating the flow rates, we obtained linear relationships between the size of the PGUVs in the range of 40 to 80 µm (Fig. 3b) using a chip with an IA channel dimension of 35 µm (Fig. S4a) and 89.3 to 104.5 µm (Fig. S5) using a chip with an IA channel dimension of 65 µm (Fig. S4b). Reducing the channel dimensions further results in even smaller PGUVs. The sizes of the PGUVs produced in this work are within the typical range for eukaryotic cells [33] (10–100 µm); thus, these

Please do not adjust margins

Please do not adjust margins

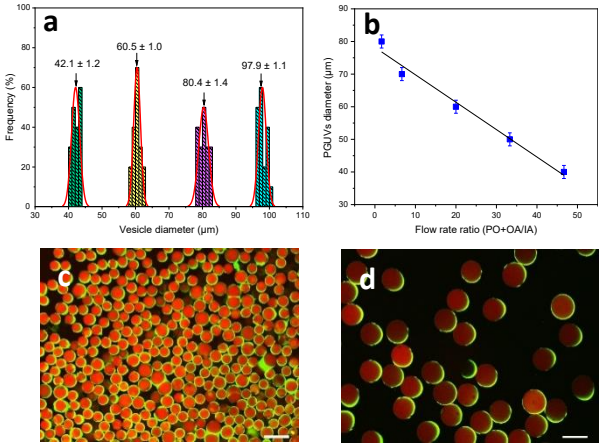

Fig. 3 (a) Frequency histograms of PGUVs in the size range of interest (40-100 µm) with highly monodisperse (1.1 to 2.8%) populations (n ≥ 200 particles). The red lines represent Gaussian fits for the individual histograms, while the arrows indicate the mean diameter and corresponding standard deviations (42.1 ± 1.2, 60.5 ± 1.0, 80.4 ± 1.4 and 97.9 ± 1.2 µm). (b) PGUV diameter as a function of the flow rate ratio of the OA/IA channels produced using a chip with an IA channel dimension of 35 µm. The line indicates a linear fit. (c) CLSM images of PGUVs using the fluorescent excitation/emission ranges of calcein (λ_{ex} = 488 nm; λ_{em} = 510-545 nm) and Nile red (λ_{ex} = 635 nm; λ_{em} = 645-665 nm). The scale bar denotes 100 µm.

PGUVs are promising candidates as a mimetic model for studying artificial cells and membranes.

Controlling the collapse of pH-responsive PGUVs

To produce relevant pH-responsive PGUV systems for biomedical applications, it is very important to ensure their stability in neutral media as well as their fast response to small external changes in pH under biological conditions. The PDPA polymer is a very promising biomaterial candidate for building pH-triggered controlled delivery systems for biomedical applications. PDPA is sensitive to small changes in external pH and completely dissociates in less than a second when the pH decrease to a value less than its pKa of 6.8 [34–36]. Moreover, PDPA is stable under physiological conditions, allowing nanocarrier systems built from this polymer to retain their original structure *in vitro* and *in vivo* at a pH of 7.4 [37]. Notably, pH-responsive PDPA nanoplatforms can target the extracellular or intracellular pH condition of tumoral tissues to realize pH-triggered drug release, thereby reducing undesirable side effects while improving drug delivery efficiency. To date, there are no records of using PDPA polymers to produce pH-responsive PGUVs. Therefore, we synthetized the pH-responsive block copolymer PEO_{45}-*b*-$PDPA_{20}$ and mixed this copolymer with the commercially available PEO_{34}-*b*-PBD_{46} at a weight ratio of 1:25 (1:3.75 molar ratio) to produce stable pH-responsive PGUVs. Several ratios were tested (12.5:25; 6.25:25; 3.12:25; 1:25), and the ratio 1:25 was selected because it provides PGUVs with the greatest long-term stability (2 weeks). The stability of the pH-responsive PGUVs was evaluated as a function of time under simulated neutral and acidic conditions using CLSM (Fig. 4).

Images of the pH-responsive PGUV samples were acquired at an interval of 60 seconds for a period of 60 minutes under neutral (pH = 7.4) conditions and a period of 20 minutes under mildly acidic (pH = 6.0) conditions (see methods). Fig. 4a-d show images of the pH-responsive PGUVs during selected time intervals within the 60 minute observation period under simulated neutral conditions at pH = 7.4. The CLSM images show that no significant differences were observed in the number or fluorescence intensity of the PGUVs during this period (Fig. 4a-d). However, after exposure to pH = 6.0, the pH-responsive PGUV samples showed clear decreases in the number of particles and fluorescence intensity of calcein as a function of time (Fig. 4e-h). After 15 minutes of exposure, the number of pH-responsive PGUVs decreased to ~90% (Fig. 4h). The reduction in the number of pH-responsive PGUVs upon acidification (pH= 6.0) indicates the presence of the pH-responsive block copolymer PEO_{45}-*b*-$PDPA_{20}$ in the bilayer membrane of the PGUVs. Because the pH-responsive PGUVs were prepared under neutral conditions (pH = 7.4, see Methods), the PDPA block is hydrophobic and sticks to the PBD block, forming polymeric bilayer membranes in the PGUVs. When the pH is less than the pKa of PDPA, the polymer block protonates and becomes hydrophilic, inducing water swelling in the polymeric bilayer. This swelling reduces the hydrophobicity of the bilayer membrane to the point where the membrane can no longer can maintain its integrity, and the PGUVs are disrupted. The disruption of the PGUVs releases the loaded calcein, causing the fluorescence intensity to fluctuate. The disruption of the pH-responsive PGUVs inducing calcein release was observed in real time (Video S2), and images of the disruption of a selected PGUV over time are shown in Fig. 5. The entire process involving the protonation of the PDPA block in the polymer bilayer membrane and the subsequent PGUV disruption is described in Scheme 1.

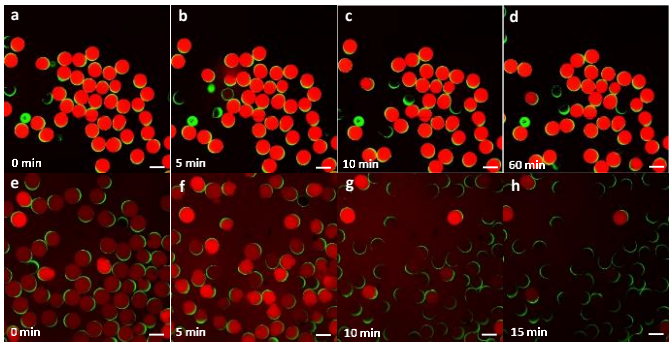

Fig. 4 A series of confocal images of the responsive PGUVs as a function of time during exposure to pH 7.4 (a-d) and pH 6.0 (e-h) at room temperature. The images depict the fluorescence excitation/emission of calcein (λ_{ex} = 488 nm; λ_{em} = 510-545 nm) and Nile red (λ_{ex} = 635 nm; λ_{em} = 645-665 nm). The scale bar denotes 100 µm.

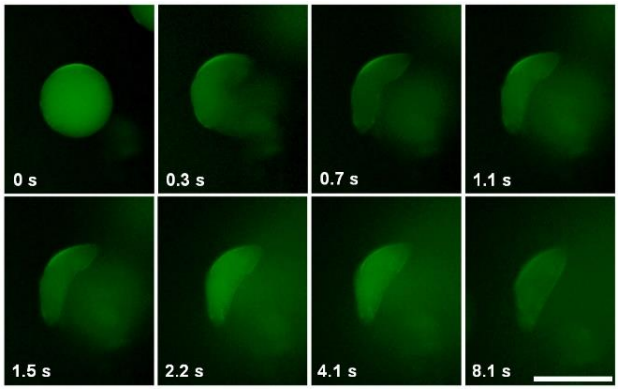

Fig. 5 Time frames in seconds showing the disruption of a pH-responsive PGUV and calcein release at pH 5.0. The images were obtained using the fluorescence excitation/emission of calcein (λ_{ex} = 488 nm; λ_{em} = 510-545 nm). The scale bar denotes 100 µm.

This journal is © The Royal Society of Chemistry 20xx

Please do not adjust margins

Please do not adjust margins

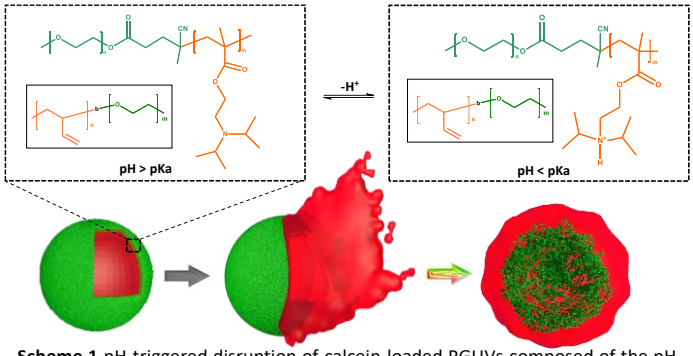

Scheme 1 pH-triggered disruption of calcein-loaded PGUVs composed of the pH-responsive block copolymer PEO_{45}-*b*-$PDPA_{20}$ and the amphiphilic block copolymer PEO_{34}-*b*-PBD_{46}. The PDPA and PBD hydrophobic blocks are represented in orange, the PEO hydrophilic block in green and calcein in red.

The pH dependence of the PGUV disruption under different acidic conditions as a function of time is shown in Fig. 6. The sensitivity of the PGUVs to small differences in the external pH was observed by following the changes in the number and fluorescent intensity of the PGUVs over time. Initially, the time for the PGUVs to be disrupted decreased significantly with decreasing pH. At pH 6.5, the time for approximately ~50% and ~80% of the PGUVs to be disrupted was ~8.5 and 12 minutes, respectively (Fig. 6a). Moreover, at pH 6.0 and 5.0, the time to disrupt the same percentage of PGUVs was found to be approximately 4.6 and 3.8 minutes, respectively. The disruption of the PGUVs as a function of pH clearly presents distinct profiles when pH values of 6.0, 5.0 and 6.5 are compared. At pH 6.5, the disruption of the PGUVs as a function of time follows a stepwise and nearly linear profile (from 5 to 12 minutes), whereas at pH 6.0 and pH 5.0, a sharp decrease is observed, and most PGUVs (> 80%) are disrupted within 3 minutes. The differences in the disruption profile of the PGUVs as a function of pH illustrate the strong dependence of the external proton concentration on the protonation process of the PDPA block. Assuming a similar polymer concentration, the results clearly indicate that the lower the external pH is in comparison to the pKa of PDPA, the faster the protonation of PDPA and the disruption of the PGUVs. Furthermore, the sharp decrease in the number of PGUVs observed at the highest proton concentrations (pH = 6.0 and 5.0) suggests that a similar amount of PDPA polymer is incorporated into each PGUV. The pH dependence of PGUV disruption as a function of time was also observed by qualitatively measuring the profile of the fluorescence intensity during the release of calcein (Fig. 6b). Initially, the fluorescence intensity increased due to the fast release and accumulation of calcein from the disrupted PGUVs in the external media. Considering a time interval of 60 seconds, the maximum fluorescence intensity from the calcein released at pH = 6.5, 6.0 and 5.0 was observed at 7, 5 and 4 minutes and corresponds to the disruption of 50, 73 and 61% of the PGUVs (Fig. 6a), respectively. Thus, the fluorescence intensity clearly shows the pH dependence of the calcein release, matching the number of PGUVs that were disrupted as a function of time. The time-related differences among the PGUV responses at distinct

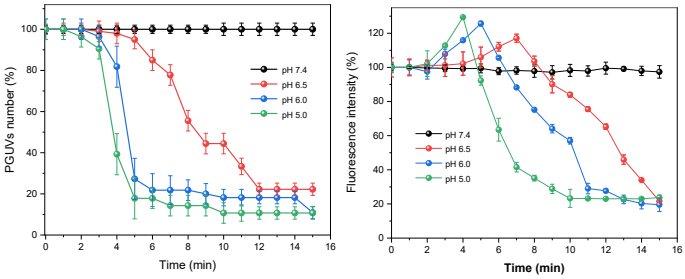

Fig. 6 Number percentage (a) and normalized fluorescence intensity of calcein (b) for pH-responsive PGUVs as a function of time after exposure to different pH values.

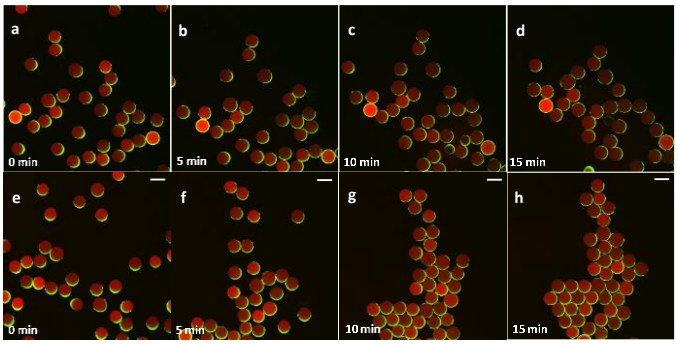

Fig. 7 A series of confocal images of nonresponsive PGUVs as a function of time during exposure to pH 7.4 (a-d) and pH 5.0 (e-h) at room temperature. The images were obtained using the fluorescence excitation/emission of calcein (λ_{ex} = 488 nm; λ_{em} = 510-545 nm) and Nile red (λ_{ex} = 635 nm; λ_{em} = 645-665 nm). The scale bar denotes 100 µm.

pH values demonstrate the sensitivity of the PDPA block to external stimuli and its potential application as a biomaterial for the development of controlled drug delivery systems.

For comparison, nonresponsive PGUVs with only PEO_{34}-*b*-PBD_{46} were prepared in the same manner and evaluated during exposure to pH = 7.4 and 5.0 (Fig. 7). No differences in the number or fluorescence intensity of the PGUVs were observed after 30 minutes of exposure to pH = 7.4 or 5.0 (Fig. S5), confirming that the pH response of the PGUVs is due to the presence of the PDPA polymer in the polymer membrane bilayer.

Cytotoxicity studies of the PGUVs

Ultimately, the *in vitro* cytotoxicity of the PGUVs was evaluated by placing them in contact with rat mesenchymal stem cells (rMSCs) for 24 or 72 hours. The rMSC cell viability data as a function of PGUV concentration and incubation time are given in Fig. 8a (24 h) and 8b (72 h). The results demonstrate the excellent biocompatibility of giant polymersomes with the rMSC cell line for both incubation times, suggesting that the PGUVs are biocompatible and nontoxic at least up to 100 $\mu g \cdot mL^{-1}$. The viability of the rMSCs in contact with the PGUVS is comparable to the viability of cells incubated with a variety of self-assemblies based on the PDPA [36,38] block and PBD [39,40] block (no statistically significant differences found by ANOVA at α=0.05), demonstrating their potential as safe building blocks in biomedical-related applications.

Please do not adjust margins

Please do not adjust margins

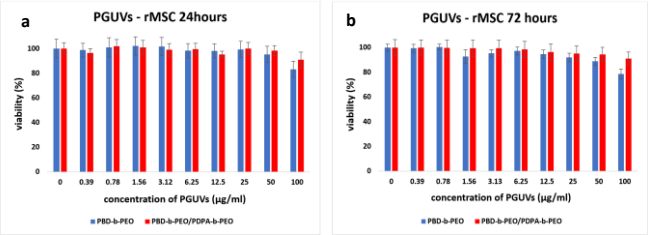

Fig. 8 Cell viability of rMSCs upon contact with PGUVs for 24 h (a) and 72 h (b).

Methods

Materials

Poly(butadiene)-*b*-poly(ethylene oxide) (PBD-*b*-PEO) Mw ~ 2,500:1,500 (PBD_{46}-*b*- PEO_{34}) was purchased from Polymer Source (Dorval, Quebec, Canada). The 2-(diisopropylamino)ethyl methacrylate monomer (DPA, 97%), initiator 4,4-azobis(4-cyanopentanoic acid) (V501) and macro chain transfer agent poly(ethylene oxide) 4-cyano-4-(phenylcarbonothioylthio)pentanoate (PEO macro CTA) with an average M_n of 2,000 g mol^{-1} were purchased from Sigma–Aldrich. Tetraethyl orthosilicate (TEOS), poly(ethylene glycol) with an average M_n of 4,600 g mol^{-1} (PEG 4,600), poloxamer 188, Nile red and calcein were purchased from Sigma–Aldrich and used as received. All solvents were of analytical grade (Sigma–Aldrich). The water used was pre-treated with the Milli-Q® Plus System (Millipore Corporation).

Synthesis of the poly(ethylene-oxide)-b-(2-(diisopropylamino)ethyl methacrylate) (PEG-b-PDPA) block copolymer

In a Schlenk flask equipped with a magnetic stirrer, poly(ethylene oxide) 4-cyano-4-(phenylcarbonothioylthio)pentanoate 2000 g·mol^{-1} (PEO 2000 macroCTA) azide (200 mg, 0.1 mmol) was dissolved in dioxane (2 mL), and 2-(diisopropylamino)ethyl methacrylate (DPA) monomer (160 mg, 0.75 mmol) was dissolved in dioxane (2 mL). The initiator AIBN (8.2 mg, 0.05 mmol) was dissolved in DMSO. The solutions were mixed, and the mixture was purged with argon for 15 minutes. Three freeze-pump-thaw cycles were performed, and the solution was purged again with argon for 15 minutes before being placing in an oil bath at 70 °C to start the polymerization process, which occurred over 48 h. Afterwards, the polymerization was quenched by exposing the reaction mixture to air and liquid nitrogen. The final product was purified through a Sephadex LH-20 column in methanol and precipitated in cold diethyl ether. The PEO-*b*-PDPA block copolymer was analysed by size exclusion chromatography (SEC) and ^{1}H NMR.

Fabrication of microfluidic devices

The microfluidic device was designed and fabricated using a previously described standard lithography process [41]. The microchannel structures were designed using AutoCAD software (Autodesk) and printed on a mask foil with a UV-absorbent ink (JD Photo Data). A negative photoresist (SU-8, Microchem Co.) was spin-coated onto a silicon wafer, and a mask aligner (Süss Mikro Tec) was used to transfer the printed microchannel structure from the mask foil to the photoresist, generating the silicon wafer master. Next, the master was used to produce poly(dimethyl siloxane) (PDMS) replicas for a 3D-focusing chip design via soft lithography, which is described in detail in the Supporting Information. Finally, inlet ports were punched into the PDMS microchannels and interfaced with polyethylene (PE) tubes to ensure that fluids could be pumped into the devices by using high-precision syringe pumps (Nemesis system; Cetoni GmbH).

TEOS modification of the microfluidic device

TEOS modification was performed as described in [42]. TEOS was mixed with ethanol at a ratio of 1:1, and the device channels were filled with the solution for 15 minutes. The remaining solution was blown with air, and 33% w/v aqueous acetic acid was loaded to catalyse the hydrolysis of TEOS for 3 minutes. Afterwards, the device was blown with air and dried at room temperature for 1 day.

PEG treatment of the microfluidic device

Hydrophilic rendering of the downstream channels was performed by adsorption of PEG 4,600 on the PDMS surface. First, the microfluidic device was treated in an oxygen plasma oven with 80 W of power for 1 minutes. Immediately after, positive air pressure was applied to the selected inlet channels by using Flow-EZ 2000 mbar pumps (Fluigent), and a 460 mg ml^{-1} PEG solution was applied to the outlet. The procedure continued for 30 minutes. Then, the outlet tube was removed, air was flushed through the inlets, and the device was placed in an oven at 115 °C for 20 minutes to immobilize the PEG 4,500 on the PDMS surface.

Solution compositions

The inner aqueous (IA) and outer aqueous (OA) phases consisted of 50 mg/ml surfactant poloxamer 188 in a glycerol/Milli-Q water solution (100 mOsm L-1) with an adjusted pH of 7.4. Diblock copolymers poly(butadiene-block-ethylene oxide) and poly[2-(diisopropylamino) ethyl methacrylate]-block-poly(ethylene oxide) at a ratio of 25:1 (w/w) were dissolved in toluene and used as polymer-carrying organic (PO) phases.

Preparation of the PGUVs

The double-emulsion droplets were prepared using the five-way microfluidic droplet generator using different flow rates pumped by 5 independent computer-controlled syringe pumps (Nemesys, Cetoni GmbH). The flow rates of the IA, PO and OA phases are shown in **Table 1**. The double-emulsion droplets were collected in vials with 100 mM glucose solution at pH 7.4, and toluene was allowed to evaporate overnight at room temperature.

This journal is © The Royal Society of Chemistry 20xx

Please do not adjust margins

Please do not adjust margins

Table 1. The flow rates of the IA, PO and OA phases.

	PGUV size (μm)			
Phase flow rate (μL h^{-1})	40	50	60	70
IA	300	300	300	300
PO	300/300	300/300	300/300	300/300
OA	7000/7000	5000/5000	3000/3000	1000/1000

In vitro cytotoxicity of the pH-responsive PGUVs

The cytotoxicity of the PGUVs was evaluated with rat mesenchymal stem cells (rMSCs). rMSCs were seeded onto 96-well tissue culture plates and cultured for 24 h prior to the addition of different concentrations of giant polymeric vesicles. The cytotoxicity of the PGUVs at 24 h and 72 h was quantified with an MTT assay. Each experimental procedure was performed in triplicate. The absorbance of the MTT product was read using a Synergy Neo plate reader (Bio-Tek, Prague, Czech Republic) at 570 nm/600 nm (excitation/emission).

Characterization of the PGUVs

Confocal laser scanning microscopy (CLSM)

The images were obtained by an IX83 confocal laser scanning microscope (Olympus, Tokyo, Japan) with a green (488 nm) and red (635 nm) laser systems. An Olympus objective (lens magnification 10x, lens NA 0.4) delivered excitation light to a diffraction-limited spot and collected the emitted fluorescence with a dichroic mirror DM405/488/543/635. All measurements were performed at 23 ± 1 °C. FluoView 1000 software version 4.2.3.6 (Olympus) was used for data acquisition and image reconstruction in XZ scanning mode.

Evaluation of the pH responsiveness of the PGUVs by CLSM

Briefly, a 25 μL aliquot of pH-sensitive PGUVs was transferred to an eight-well μ-Slide (Ibidi, Martinsried, Germany). Furthermore, 25 μL of isomolar acetate buffer glucose solution (100 mOsm L^{-1}) with pH 6.5, 6 and 5 was added to the wells to reduce the pH to approximately the experimentally desired pH values of 6.5, 6 and 5. As a control, 25 μL of an isomolar phosphate buffer glucose solution (pH = 7.4) was added to the same amount of PGUVs (25 μL). All samples were imaged at room temperature in 1-minute intervals using CLSM. The images were acquired in the same region of interest, and the number of PGUVs as a function of time was calculated by ImageJ software. The overall fluorescence intensity of the PGUVs loaded with calcein as a function of time before and after exposure to different pH values was calculated using the FluoView 1000 software package (Olympus).

In vitro cytotoxicity of the pH-responsive PGUVs

The cytotoxicity of the PGUVs was evaluated with rat mesenchymal stem cells (rMSCs). rMSCs were seeded onto 96-well tissue culture plates and cultured for 24 h prior to the addition of different concentrations of giant polymeric vesicles. The cytotoxicity of the PGUVs at 24 h and 72 h was quantified with an MTT assay. Each experimental procedure was performed in triplicate. The absorbance of the MTT product was read using a Synergy Neo plate reader (Bio-Tek, Prague, Czech Republic) at 570 nm/600 nm (excitation/emission).

Conclusions

We report the development of a PDMS-based microfluidic device capable of generating stable water-in-oil-in-water (W/O/W) microdroplets for the production of pH-responsive PGUVs based on a combination of poly(ethylene oxide)-*b*-poly(1,2-butadiene) (PEO_{34}-*b*-PBD_{46}) and synthesized poly(ethylene-oxide)-*b*-poly[2-(diisopropylamino) ethyl methacrylate (PEO_{45}-*b*-$PDPA_{20}$). By manipulating the flow rate ratios in the microfluidic device, highly monodisperse and stable pH-responsive PGUVs of different sizes were produced in a controlled manner. The sensitivity of the pH-responsive PGUVs was investigated using CLSM imaging after evaluating the percentage of disrupted vesicles and fluctuations in the fluorescence intensity as functions of time during exposure to different pH values. The CLSM images demonstrate the clear dependence of PGUV disruption and calcein release on pH. The lower the pH value, the faster the PGUVs were disrupted and calcein was released. Moreover, the temporal synchronization of PGUV disruption as a function of pH is strong evidence that each PGUV contains a similar amount of PDPA, thereby allowing fast and homogenous calcein release that can be controlled by a pH-triggered mechanism. To the best of our knowledge, the spatiotemporal pH-triggered controlled release of a hydrophilic probe in a PH-responsive PGUV system was demonstrated here for the first time. Finally, the cytotoxicity of the PGUVs in rMSCs showed good biocompatibility, demonstrating the capabilities of pH-responsive PGUVs as biomimetic systems for drug delivery, microreactors and artificial cell mimics.
The conclusions section should come in this section at the end of the article, before the acknowledgements.

Author Contributions

A. J. designed the project. E. J. and V. S. performed all synthetic experiments. J. P. with V. S. characterized and analysed the data. K. L. C., and M. V. assisted with cytotoxicity.
P. S., M. H., E. J., E. H., M. S., and S. F. discussed the results and commented on the manuscript. The manuscript was written by A. J. and V.S.

Conflicts of interest

There are no conflicts to declare.

Acknowledgements

Please do not adjust margins

Please do not adjust margins

The investigations have been sponsored by the Czech Science Foundation (grant # 20-13946Y). E. J. would like to acknowledge the financial support from Czech Academy of Sciences (Grant # 20-15077Y). P.S. acknowledges financial support from Czech Science Foundation (grant # 21-04166S).

Notes and references

The authors declare no competing financial interest.

1 Y. Zhu, B. Yang, S. Chen and J. Du, *Prog. Polym. Sci.*, 2017, **64**, 1–22.

2 J.-F. Le Meins, O. Sandre and S. Lecommandoux, *Eur. Phys. J. E*, 2011, **34**, 14.

3 E. Rideau, R. Dimova, P. Schwille, F. R. Wurm and K. Landfester, *Chem. Soc. Rev.*, 2018, **47**, 8572–8610.

4 M. Houbrechts, L. Caire da Silva, A. Ethirajan and K. Landfester, *Soft Matter*, 2021, **17**, 4942–4948.

5 E. C. dos Santos, A. Angelini, D. Hürlimann, W. Meier and C. G. Palivan, *Chemistry (Easton).*, 2020, **2**, 470–489.

6 B. C. Buddingh' and J. C. M. van Hest, *Acc. Chem. Res.*, 2017, **50**, 769–777.

7 C. Guindani, L. C. Silva, S. Cao, T. Ivanov and K. Landfester, *Angew. Chemie Int. Ed.*, , DOI:10.1002/anie.202110855.

8 Y. Elani, T. Trantidou, D. Wylie, L. Dekker, K. Polizzi, R. V. Law and O. Ces, *Sci. Rep.*, 2018, **8**, 4564.

9 L. Otrin, A. Witkowska, N. Marušič, Z. Zhao, R. B. Lira, F. L. Kyrilis, F. Hamdi, I. Ivanov, R. Lipowsky, P. L. Kastritis, R. Dimova, K. Sundmacher, R. Jahn and T. Vidaković-Koch, *Nat. Commun.*, 2021, **12**, 4972.

10 Y. Zhou and D. Yan, *Angew. Chemie Int. Ed.*, 2004, **43**, 4896–4899.

11 Z. Lu and J. Guo, *Front. Bioeng. Biotechnol.*, , DOI:10.3389/fbioe.2020.01018.

12 J. W. Hindley, R. V. Law and O. Ces, *SN Appl. Sci.*, 2020, **2**, 593.

13 E. Boedtkjer and S. F. Pedersen, *Annu. Rev. Physiol.*, 2020, **82**, 103–126.

14 K. Rajamäki, T. Nordström, K. Nurmi, K. E. O. Åkerman, P. T. Kovanen, K. Öörni and K. K. Eklund, *J. Biol. Chem.*, 2013, **288**, 13410–13419.

15 N. Song, Z. Lu, J. Zhang, Y. Shi, Y. Ning, J. Chen, S. Jin, B. Shen, Y. Fang, J. Zou, J. Teng, X.-P. Chu, L. Shen and X. Ding, *J. Cell. Mol. Med.*, 2019, **23**, 3429–3440.

16 C. H. Heo, M. K. Cho, S. Shin, T. H. Yoo and H. M. Kim, *Chem. Commun.*, 2016, **52**, 14007–14010.

17 V. Passos Gibson, M. Fauquignon, E. Ibarboure, J. Leblond Chain and J.-F. Le Meins, *Polymers (Basel).*, 2020, **12**, 637.

18 E. Rideau, F. R. Wurm and K. Landfester, *Polym. Chem.*, 2018, **9**, 5385–5394.

19 T. P. T. Dao, M. Fauquignon, F. Fernandes, E. Ibarboure, A. Vax, M. Prieto and J. F. Le Meins, *Colloids Surfaces A Physicochem. Eng. Asp.*, 2017, **533**, 347–353.

20 A. N. Albertsen, J. K. Szymański and J. Pérez-Mercader, *Sci. Rep.*, 2017, **7**, 41534.

21 C. Kunzler, S. Handschuh-Wang, M. Roesener and H. Schönherr, *Macromol. Biosci.*, 2020, **20**, 2000014.

22 W. Wang, M.-J. Zhang and L.-Y. Chu, *Curr. Opin. Pharmacol.*, 2014, **18**, 35–41.

23 S.-H. Kim, J. W. Kim, J.-C. Cho and D. A. Weitz, *Lab Chip*, 2011, **11**, 3162–3166.

24 S. Battat, D. A. Weitz and G. M. Whitesides, *Lab Chip*, 2022, **22**, 530–536.

25 C. Chen, B. T. Mehl, A. S. Munshi, A. D. Townsend, D. M. Spence and R. S. Martin, *Anal. Methods*, 2016, **8**, 6005–6012.

26 K. Y. Kim, P., Kwon, K.W., Park, M.C., Lee, S.H., Kim, S.M., & Suh, *Biochip J.*, 2008, **2**, 1–11.

27 A. R. Abate, D. Lee, T. Do, C. Holtze and D. A. Weitz, *Lab Chip*, 2008, **8**, 516.

28 Y. Li, T. Zhao, C. Wang, Z. Lin, G. Huang, B. D. Sumer and J. Gao, *Nat. Commun.*, 2016, **7**, 13214.

29 A. Joseph, C. Contini, D. Cecchin, S. Nyberg, L. Ruiz-Perez, J. Gaitzsch, G. Fullstone, X. Tian, J. Azizi, J. Preston, G. Volpe and G. Battaglia, *Sci. Adv.*, , DOI:10.1126/sciadv.1700362.

30 S. Jain and F. S. Bates, *Science*, 2003, **300**, 460–464.

31 H. C. Shum, J.-W. Kim and D. A. Weitz, *J. Am. Chem. Soc.*, 2008, **130**, 9543–9549.

32 S. Deshpande, Y. Caspi, A. E. C. Meijering and C. Dekker, *Nat. Commun.*, 2016, **7**, 10447.

33 S. F. Fenz and K. Sengupta, *Integr. Biol.*, 2012, **4**, 982.

34 A. Jäger, E. Jäger, F. Surman, A. Höcherl, B. Angelov, K. Ulbrich, M. Drechsler, V. M. Garamus, C. Rodriguez-Emmenegger, F. Nallet and P. Štěpánek, *Polym. Chem.*, 2015, **6**, 4946–4954.

35 M. Massignani, I. Canton, T. Sun, V. Hearnden, S. MacNeil, A. Blanazs, S. P. Armes, A. Lewis and G. Battaglia, *PLoS One*, 2010, **5**, e10459.

36 F. C. Giacomelli, P. Stepánek, C. Giacomelli, V. Schmidt, E. Jäger, A. Jäger and K. Ulbrich, *Soft Matter*, 2011, **7**, 9316.

37 L. J. C. Albuquerque, V. Sincari, A. Jäger, J. Kucka, J. Humajova, J. Pankrac, P. Paral, T. Heizer, O. Janouškova, I. Davidovich, Y. Talmon, P. Pouckova, P. Štěpánek, L. Sefc, M. Hruby, F. C. Giacomelli and E. Jäger, *J. Control. Release*, 2021, **332**, 529–538.

38 M. Luo, H. Wang, Z. Wang, H. Cai, Z. Lu, Y. Li, M. Du, G. Huang, C. Wang, X. Chen, M. R. Porembka, J. Lea, A. E. Frankel, Y.-X. Fu, Z. J. Chen and J. Gao, *Nat. Nanotechnol.*, 2017, **12**, 648–654.

39 Z. Cheng, D. R. Elias, N. P. Kamat, E. D. Johnston, A. Poloukhtine, V. Popik, D. A. Hammer and A. Tsourkas, *Bioconjug. Chem.*, 2011, **22**, 2021–2029.

40 R. C. Amos, A. Nazemi, C. V. Bonduelle and E. R. Gillies, *Soft Matter*, 2012, **8**, 5947.

41 M. Schlenk, M. Drechsler, M. Karg, W. Zimmermann, M. Trebbin and S. Förster, *Lab Chip*, 2018, **18**, 3163–3171.

42 J. H. L. Beal, A. Bubendorfer, T. Kemmitt, I. Hoek and W. Mike Arnold, *Biomicrofluidics*, 2012, **6**, 036503.

This journal is © The Royal Society of Chemistry 20xx

Please do not adjust margins